

Atomistic Understanding of Calcium Silicates:
Experimental and Theoretical Research

Zur Erlangung des akademischen Grades eines
DOKTORS DER NATURWISSENSCHAFTEN

(Dr. rer. nat.)

von der KIT-Fakultät für Chemie und Biowissenschaften
des Karlsruher Instituts für Technologie (KIT)

genehmigte

DISSERTATION

von

Dipl.-Ing. Nicolas Giraudo

aus

Villa María, Córdoba, Argentinien

KIT-Dekan: Prof. Dr. Willem Klopper

Referent: Prof. Dr. Christof Wöll

Korreferent: Priv. Doz. Dr. Artur Böttcher

Tag der mündlichen Prüfung: 24.04.2017

To my father.

I hereby declare, that this thesis is based on my own work and was written by me. I referenced the corresponding parts of the text that were extracted from other works.

Nicolas Giraudo
15.03.2017

Contents

1	Introduction	5
1.1	Suitable Model Systems for Cement and Concrete Research	5
1.2	Motivation	8
1.3	Description of Approaches and Objectives	9
2	Metal-Proton Exchange Reaction (MPER)	14
2.1	Wollastonite as a Model of Calcium Silicates	14
2.2	Methodology	14
2.3	Kinetic Aspects: MPER at Different Orientations of the Wollastonite Crystal	16
2.4	Thermodynamic Aspects: Non-stoichiometric Ground State of Wol- lastonite	18
2.5	Experimental Confirmation of Theoretical Findings	20
2.6	Summary	25
3	Corrosion Induced by Water: Detection by Shape Changes	26
3.1	Wulff Construction	26
3.2	Methodology	27
3.3	Experimental Observation of Shape Changes	28
3.4	Theoretical Evaluation of the Shape Changes	29
3.5	Summary	32
4	Calcium-Silicate-Hydrate Phases on Silicon: a New Model System	33
4.1	Lacks of Knowledge Filled by the New Model System	33
4.2	Methodology	33
4.3	Fourier Transform Infrared Spectroscopy (FTIR)	34
4.4	Characterization of C-S-H Phases Synthesized on Silicon	35
4.5	Synthesis of C-S-H Phases and Transformation into C-S Phases	40
4.6	Thermodynamic Analysis of the Crystallization of C-S Phases	43
4.7	Dehydroxylation Temperature vs. Ca/Si ratio	46
4.8	Experimental Modification of the Ca/Si ratio and Confirmation of Theoretical Results	48
4.9	Summary	54
5	The Problem of Passivation of C-S-H Phases by Carbonation	56
5.1	Passivation Approaches to Avoid Corrosion: Concept of Activation . .	56
5.2	Methodology	56
5.3	Nature of Carbonates on C-S Phases: Two Different Species	58

5.4	Synthesis of C-S-H Phases on Silicon Wafers	60
5.5	Activation Techniques	63
5.6	Efficiency of the Activation	68
5.7	Summary	70
6	Implementation of High Temperature Resistant Phosphate-Probe Molecules: Phosphates	71
6.1	Interface Characterization by Probe Molecules	71
6.2	Selection of Phosphates as Probe Molecules	71
6.3	Methodology	72
6.4	C-S-H Phases Characterization and Transformation into C-S Phases .	73
6.5	Application of Probe Molecules on C-S-H Phases	76
6.6	Application of Probe Molecules on C-S Phases	78
6.7	Driving Force of the Diffusion of Phosphates and Phosphorus	80
6.8	ToF-SIMS Confirmation of the Diffusion	82
6.9	Summary	82
7	Conclusions and Perspectives	84
7.1	Conclusions	84
7.2	Perspectives	85
8	Acknowledgements	88
9	Publications	89
10	References	90

Abstract

Hydrated cement, also called concrete, is the most used construction material by mankind. In this thesis model systems are proposed to study the Calcium-Silicate (C-S) and Calcium-Silicate-Hydrate (C-S-H) phases, which are the most important components of hydrated cement. The implementation of model systems is intended to achieve an atomistic understanding of the C-S and C-S-H phases. The model systems presented here can be classified into two main categories: well-known nature minerals and synthesized phases. In the first part of this work Wollastonite is applied, which is a natural calcium silicate. Applying theoretical and experimental methods from the surface science, a very important aspect of such mineral in contact with water is brought up and further studied: the Metal-Proton Exchange Reaction (MPER). This reaction represents the basic mechanism of corrosion of concrete by water, which is also analyzed on particles to observe shape changes. The drastic effects produced on the particles are simulated by means of density functional theory (DFT) calculations, revealing the importance of kinetic considerations at the corrosion by water. In the second part of this dissertation, specific ultrathin C-S-H phases synthesized on silicon wafers are implemented as model. Samples are investigated by means of Fourier Transform Infrared (FTIR) spectroscopy and X-ray diffraction (XRD) and their results are analyzed again on the basis of first principles calculations. The synthesis of the most important components of concrete on silicon wafers allows to control their chemical composition, by modifying conditions during the synthesis. The chemical composition of these C-S-H and C-S phases can also be changed by putting them in contact with specific molecules. First, carbon dioxide is put in contact with the surfaces to analyze the effects of carbonates, finding them to be a barrier for passivation techniques. Several activation techniques are presented and their efficiency is evaluated. Afterwards, phosphates are used as probe molecules to further study the calcium silicate structure. A detailed and self-consistent picture of the chemical and structural properties of interfaces such as the one between the atmosphere and ultrathin C-S phases (gas/C-S) and the one between them and silicon wafers (C-S/Si) is achieved. The material combination of C-S/C-S-H phases synthesized on silicon wafers might in the future have great potential in selective chemistry, catalysis, and sensing technologies as well as in semiconductor manufacturing.

Zusammenfassung

Hydratisierter Zement, auch Beton genannt, ist das am meisten verwendete Baumaterial der Menschheit. In dieser Arbeit werden Modellsysteme vorgeschlagen, um die Calcium-Silikat (C-S) und Calcium-Silikat-Hydrat (C-S-H)-Phasen zu untersuchen. Diese sind die wichtigsten Bestandteile von hydratisiertem Zement. Die Umsetzung von Modellsystemen soll ein atomares Verständnis der C-S- und C-S-H-Phasen erreichen. Die hier vorgestellten Modellsysteme lassen sich in zwei Hauptkategorien einteilen: bekannte Naturminerale und synthetisierte Phasen. Im ersten Teil dieser Arbeit wird Wollastonit angewendet, ein natürliches Calciumsilikat. Bei der Anwendung theoretischer und experimenteller Methoden aus der Oberflächenwissenschaft

wird ein sehr wichtiger Aspekt eines solchen Minerals in Kontakt mit Wasser aufgeworfen und weiter untersucht: die Metal-Proton Exchange-Reaktion (MPER). Diese Reaktion stellt den Grundmechanismus der Korrosion von Beton durch Wasser dar, der auch auf Partikel analysiert wird, um Formänderungen zu beobachten. Die auf den Partikeln erzeugten drastischen Effekte werden mittels Dichtefunktionaltheorie (DFT) simuliert, was die Bedeutung kinetischer Betrachtungen bei der Korrosion durch Wasser aufdeckt. Im zweiten Teil dieser Dissertation werden spezifische ultradünne C-S-H-Phasen auf Silizium-Wafern synthetisiert, die als Modell implementiert werden. Die Proben werden mittels Fourier-Transformations-Infrarot (FTIR)-Spektroskopie und Röntgenbeugung (XRD) untersucht, und ihre Ergebnisse werden anhand von First-principles-Untersuchungen unterstützt. Die Synthese der wichtigsten Komponenten von Beton auf Silizium-Wafern ermöglicht es, ihre chemische Zusammensetzung zu kontrollieren, indem die Bedingungen bei der Synthese modifiziert werden. Ihre chemische Zusammensetzung kann auch verändert werden, indem man sie mit spezifischen Molekülen in Kontakt bringt. Zuerst wird Kohlendioxid mit den Oberflächen in Kontakt gebracht, um die Auswirkungen von Carbonaten zu analysieren. Es wurde dabei gefunden, dass sie als eine Barriere für Passivierungstechniken dienen. Es werden mehrere Aktivierungstechniken vorgestellt und deren Effizienz wird ausgewertet. Danach, werden Phosphate als Sondenmoleküle verwendet, um die Calciumsilikatstruktur weiter zu untersuchen. Ein detailliertes Bild der chemischen und strukturellen Eigenschaften von den Grenzflächen zwischen der Atmosphäre und den ultradünnen C-S-Phasen (Gas/C-S) und zwischen C-S-Phasen und Silizium-Wafern (C-S/Si) wurde erreicht. Die Materialkombination aus C-S-Phasen, die auf Silizium-Wafern synthetisiert werden, kann künftig ein großes Potenzial in der selektiven Chemie, Katalyse und Sensortechnik sowie in der Halbleiterfertigung haben.

1 Introduction

The development of construction materials has been a trending topic since prehistory. The construction chemistry plays a crucial role in such development and the design of new materials to be produced industrially remains very promising and will be applicable in the future. Even more interesting are the advances on the development of recycling technologies of concrete. Reprocessing concrete is a very attractive solution to the problem of waste management. However, the outcome of these approaches does not satisfy the demand of construction materials or are more expensive than the ones on the market. Therefore, year after year the concrete industry keeps producing on the same or even greater scale, and the consumption grows steadily. Thus, the most urgent inquietude of the construction chemistry should be the deterioration, which has to be investigated around the standing materials in form of buildings, bridges, roads among others. In order to avoid corrosion, a deeper understanding of existing materials is necessary for the industry of the 21st century to develop adequate and sustainable infrastructures. Despite the numerous published works in this field, lacks of knowledge were detected, some of which can be filled with the implementation of model systems. These models are to contribute to the understanding of the phenomena in which cementitious compounds are involved. In this thesis, two different kinds of substrates are proposed as models for Calcium-Silicate (C-S) and Calcium-Silicate-Hydrate (C-S-H) phases, the most important components of concrete. In the figure 1, a graphical overview of the contents of the following chapters is presented.

1.1 Suitable Model Systems for Cement and Concrete Research

In all developed countries Portland-cement concrete is the most widely used construction material.¹⁻³ The consumption of cement is steadily growing and expected to grow by 7.5 % in 2015 and by 7.9 % in 2016.⁴⁻⁵ Since Calcium-Silicate-Hydrate (C-S-H) and Calcium-Silicate (C-S) phases are the most important components of hydrated cement (concrete), their structure and chemical properties have been subject of numerous experimental investigations.⁶⁻⁷ The huge interest in these compounds originates from their suitability as model systems for concrete.⁸ Despite the importance of the surface chemistry of these materials in the context of corrosion, their rather complicated structure has so far largely prohibited to gain a deeper understanding. The knowledge about surface processes and information down to the atomic level is rather limited.⁹ The most frequently used model systems for cement and concrete are well-known minerals. However, several issues have been hindering the investigation of well-defined mineral substrates under ultrahigh vacuum (UHV) conditions, that are mandatory for many analytical methods. Experimental problems and the fact that, until recently, infrared spectroscopy could not be applied to the surfaces of bulk dielectrics are examples of such issues. Consequently, the further research of model reactions using spectroscopic methods has so far not been carried out. This lack of detailed experimental information prohibits a validation of theoretical predictions and makes a detailed understanding of even simple chemical

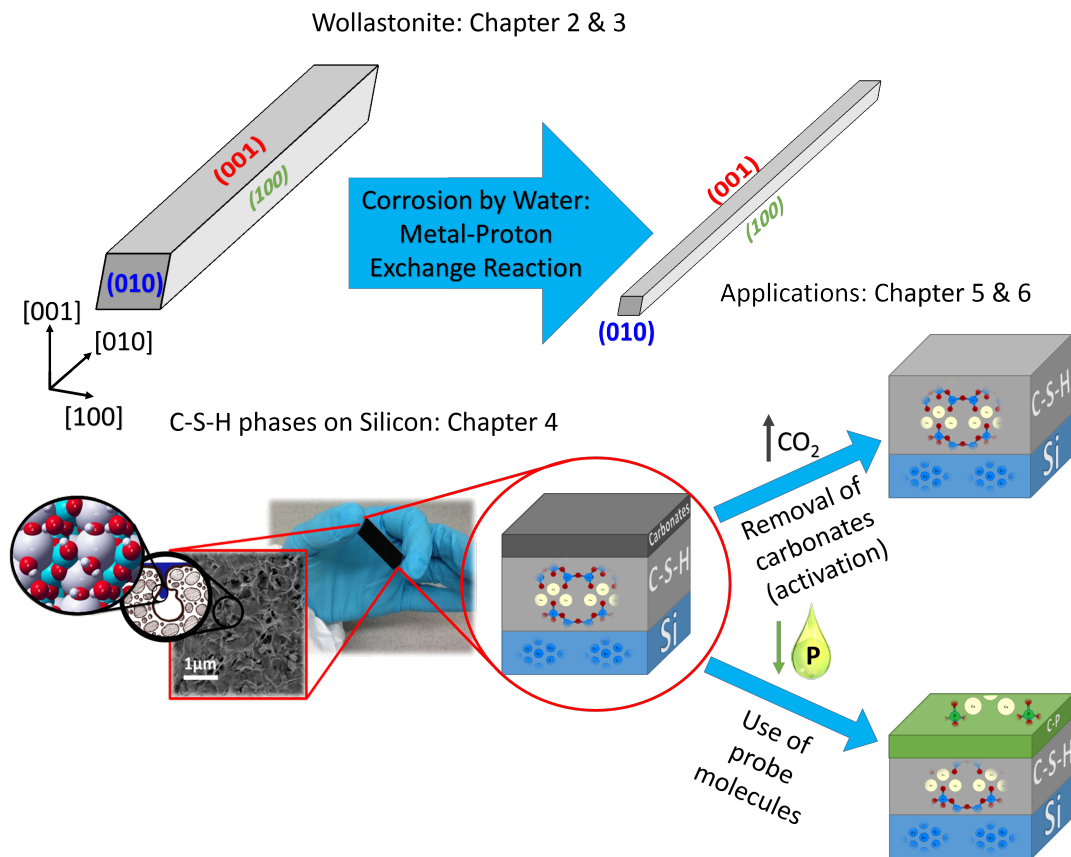


Figure 1: Graphical overview of the contents.

processes on mineral surfaces, and in particular on concrete, virtually impossible.

Two different model systems are proposed in this work. In the first part Wollastonite as model for calcium silicates is applied. Wollastonite is a chemically well characterized mineral (CaSiO_3) named in honor of the English mineralogist Sir Wollaston. Numerous applications have been found for this mineral ranging from medicine with the formation of artificial bones, due to its bioactivity, to construction chemistry, with calcium silicates as model system e.g. for the Portland cement. The bioactivity as well as the hydration of cement develops in the presence of water and both processes have to be correlated with the so called Metal-Proton Exchange Reaction (MPER, also called early stage hydration).¹⁰ The crystal structure of Wollastonite consists of silicate chains parallel to the b-axis (see figure 2), which are linked with a periodicity of three tetrahedra; usually called dreierketten.¹¹ The calcium is linked by octahedral coordination to six of the oxygens.¹² While the bulk structure is well characterized, scarce information is available about the surface chemistry of this material and, particularly, about its interaction with water. However, some authors have investigated this mineral experimentally. Schott et al. reported an experimental investigation of the dissolution reactions occurring at the surfaces of this mineral under acidic conditions and analyzed the effects by X-ray Photoelectron Spectroscopy (XPS), Diffuse Reflectance Infrared Fourier-Transformed (DRIFT) spectroscopy and Transmission Electron Microscopy (TEM).⁷ Their conclusions are supported and further explained in this thesis. A number of

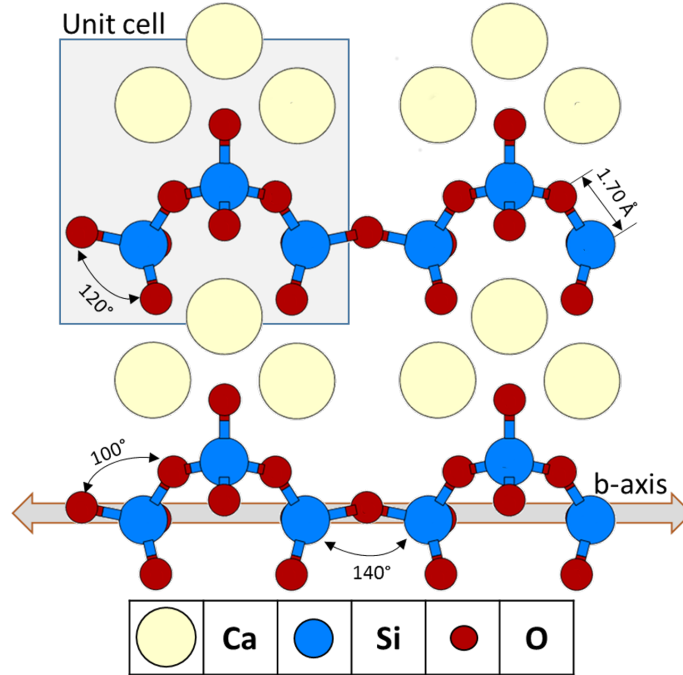


Figure 2: Side view of a $(1 \times 2 \times 2)$ unit cell of Wollastonite, relaxed by means of first principles calculations.

studies have demonstrated the importance of this mineral as a model system for concrete.^{5,10} Despite of the great suitability of this mineral as a model system for concrete investigations, its availability is limited. Furthermore, changes in the chemical composition of the C-S and C-S-H phases cannot be fully analyzed by just using this mineral, since the Ca/Si ratio is constant for Wollastonite. Thence, the development of new realistic materials combinations remains necessary.

The investigation presented in this work is focused on two main reactions, the already mentioned corrosion by water, and the carbonation. Carbonates are present in the industry and in the quotidian life with several applications. Metal carbonates like calcium carbonate are used to produce clinker, that later will be implemented for cement; sodium carbonates are used to produce glasses, soaps, detergents and paper; lithium carbonates are very popular in the pharmaceutical industry; cobalt carbonates in the catalysts industry, among many examples.¹³⁻¹⁴ However, another application of carbonates production is nowadays of rising importance: its utilization for the sequestration of CO_2 .¹⁵⁻¹⁶ Since CO_2 is the principal gas responsible for the Greenhouse Effect, one of the greatest but only partially successful efforts of the research community during the last century was to control the release of this gas, regulating thereby the global warming.¹⁷ During the production of cement, a lot of CO_2 is released, and therefore alternatives to reduce it, like for example storage of the gas through sequestration via carbonation, are in constant development.^{15,18-22} Carbonates can have negative effects inhibiting for example heavy metals to be transferred from soil to plants.²³ The presence of carbonates in many minerals as impurities is well known, and its presence in C-S-H phases has been well characterized.²⁴⁻²⁶ Some interesting works have demonstrated that the implementation of C-S-H phases for CO_2 storage is really promising, for example using supercritical CO_2 conditions.²⁷⁻²⁸

However, the discussion whether the hydrated cement can be applied for CO₂ storage remains controversial, since the impact of such process on the mechanical properties of the concrete is still unknown. Independently of the influence of carbonates on the mechanical properties of concrete, the chemical impact associated to the formation of carbonates on concrete surfaces has to be investigated.

1.2 Motivation

Concrete degradation is a major problem for industrialized countries. According to a study published in 2014, in 2002 a total of 8.3 billion dollars had to be spent only on repair and maintenance of highway bridges. The total amount of expenses required for the removal of corrosion damage to all concrete-based materials was at least an order of magnitude higher.²⁹ There are many reasons for the failure of concrete-based constructions: corrosion of supporting (metal) bars, mechanical stress caused by vehicles, or rapid heating-cooling cycles resulting from day/night temperature changes. However, one of the largest problems is the interaction of C-S and C-S-H phases with water.

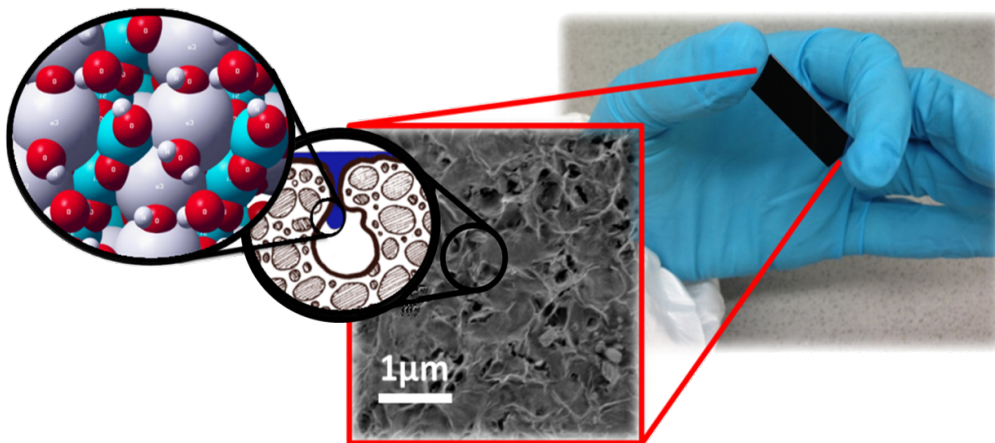


Figure 3: Representation of the model system achieved with the synthesis of Calcium-Silicate-Hydrate phases on silicon wafers.

The corrosion of C-S and C-S-H phases induced by water is controlled by MPER.³⁰ During the MPER, Ca is removed from the structure and replaced by protons from water, building calcium hydroxide as a product.³⁰ Since the deteriorating of constructions materials represents high spendings for many countries, approaches have to be developed to avoid it. The detection of the corrosion of such materials is as important as the protection. Since the C-S-H and C-S phases are responsible for the mechanical properties of hydrated cement, the understanding of corrosion mechanisms is important not only for both reasons, durability and quality of building.^{31,10}

Apart from the corrosion occasioned by water, carbonation is also very important and must be considered. MPER in presence of CO₂ was already investigated, to understand the dependence of the building of carbonates in presence of water.³² One of the most transcendental conclusions of such work is that the carbonation occurs

very quickly independently of MPER. The end products of dry and wet carbonation are predicted, and their structures are calculated and discussed in the chapter 5.^{33–34}

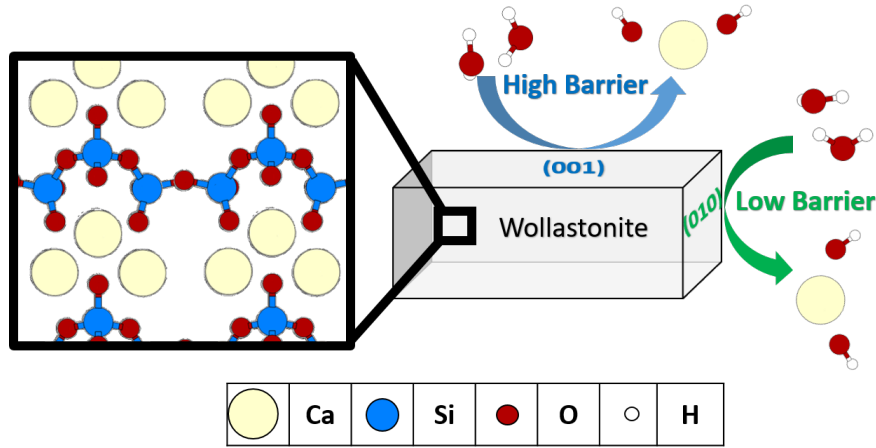


Figure 4: The Kinetic behaviour of the Metal-Proton Exchange Reaction on Wollastonite depends on the crystal orientation.

Carbonation is as important as corrosion, not only due to the effects that this reaction can have in the mechanical properties of the materials. As was mentioned in the last section, the carbonates formed on the C-S and C-S-H surfaces passivate them, and impede further reaction of the surfaces with many molecules, as will be discussed in the Chapter 5. The investigation of the above mentioned reactions, causing corrosion and passivation requires simulations at the atomic level, i.e. a deeper understanding of the C-S-H phases.⁶ The approaches employed in this thesis are destined to achieve such understanding by implementing two substrates as models: the mentioned Wollastonite and C-S-H and C-S phases synthesized on silicon wafers presented in the figure 3. These approaches will highlight new aspects of the corrosion reactions, carbonation, Ca/Si ratio influences, among others.³⁵

1.3 Description of Approaches and Objectives

Corrosion of hydrated cement has to be understood and avoided. In this dissertation:

- In order to gain a deeper understanding of the Metal-Proton Exchange Reaction (MPER), first principles calculations are applied and a qualitative model describing the kinetics of the correlation between exchanged calcium and protons at the water/Wollastonite interface is developed as shown in the figure 4 (chapter 2). Ab initio calculations are performed to further investigate the dependence of the MPER on the pH value at the interface with water. The theoretical results for basic and neutral regime ranging from pH 14 to pH 4 are in good agreement with those of in-situ Atomic Force Microscopy (AFM) experiments performed in a liquid cell. For the acidic regime between pH 4 and pH 0, the MPER alone can no longer explain all experimental results

but has to be expanded. Finally, one complete new aspect of the MPER is investigated, the strong anisotropic characteristic, detected in AFM and Low Energy Ion Scattering (LEIS) measurements.

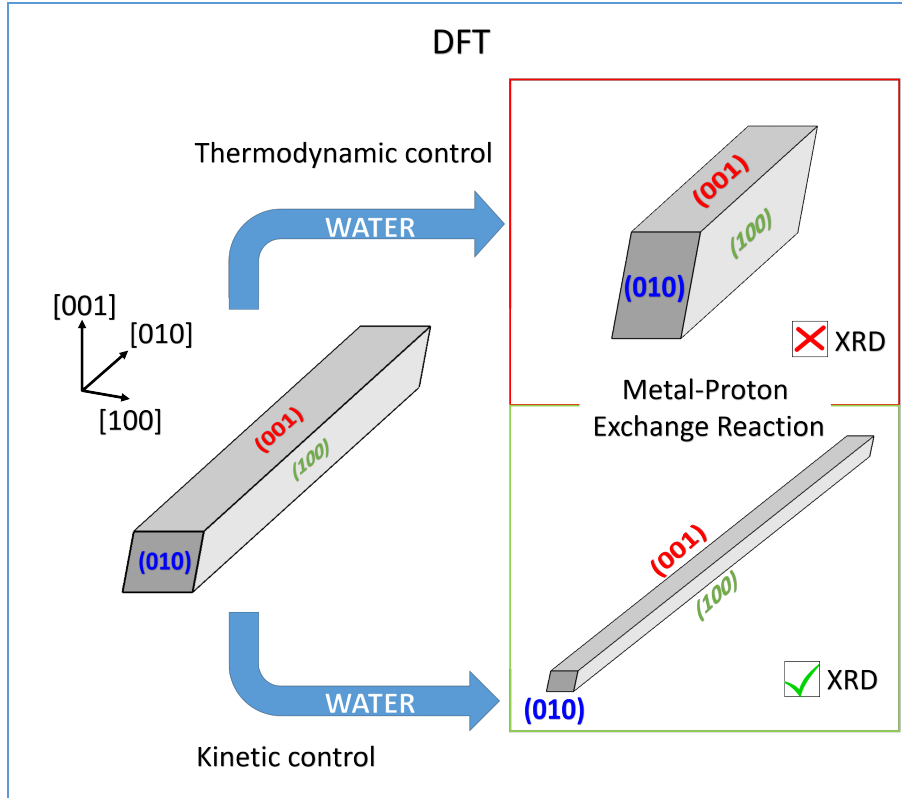


Figure 5: Shape changes caused by chemical corrosion of Wollastonite induced by water, explained with Wulff constructions.

- As was mentioned before, the detection of corrosion is also very important. Therefore the effects of corrosion by water on Wollastonite are analyzed in the chapter 3. The outcome of XRD-experiments on Wollastonite are analyzed, and compared with theoretical results presented by Wulff constructions (see Figure 5). Surprisingly, however, the predicted changes in the shape of the Wollastonite-particles are not consistent with our experimental XRD results. Expanding the Wulff constructions by explicitly considering kinetic control a consistent picture of experimental and theoretical findings can be derived.
- Due to the mentioned limitations of Wollastonite, a new material combination was developed as a promising model system for the future: C-S-H phases were synthesized on silicon wafers. In the chapter 4, the effects of all relevant parameters to control the synthesis are presented and analyzed.^{36–37} Samples are investigated by means of Fourier Transform Infrared (FTIR) spectroscopy and X-ray Diffraction (XRD) and the results are supported with first principles calculations. The important findings of chapter 4 are summarized in the figure 6. Substituting water in the solutions partially with methanol at the synthesis, the chemical composition of the C-S-H phases changes, increasing

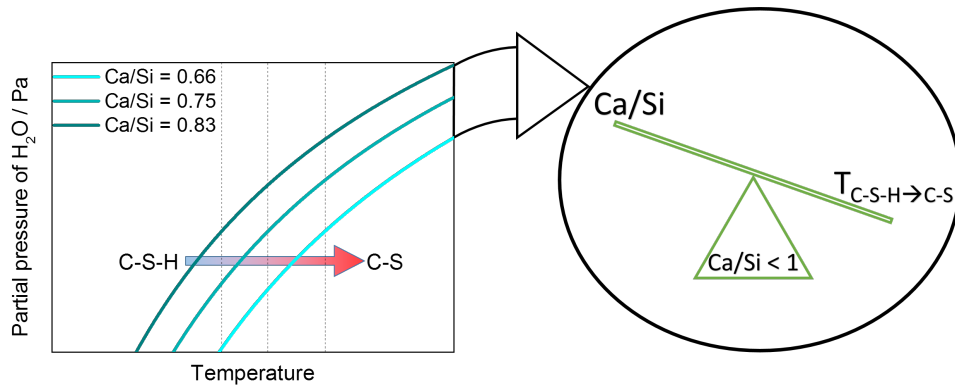


Figure 6: Temperature of dehydroxylation as a function of different Ca/Si ratios of Calcium-Silicate-Hydrate phases.

the Ca/Si ratio. The effects of different Ca/Si ratios on the temperature of dehydroxylation are analyzed. The core of this section lies on the preparation of a model surface. Its remarkable properties allows to highlight the importance of C-S and C-S-H phases, and makes it possible to model reactivity, stability and mechanical properties using first principles calculations.



Figure 7: Schema of the results obtained by the activation of Calcium-Silicate-Hydrate phases with four different techniques: heating, UV-light exposure, plasma and wet chemical treatment.

- Towards the protection of construction materials against corrosion, the activation is suggested in chapter 5. Activation means, in this case, the removal of carbonates which inhibit the covalent bonding of many passivation molecules on the surface. Ultrathin C-S-H phases on silicon wafers are prepared, which are partially terminated by calcium carbonates. First, a Density Functional Theory (DFT) analysis is performed, to define the nature of the carbonates

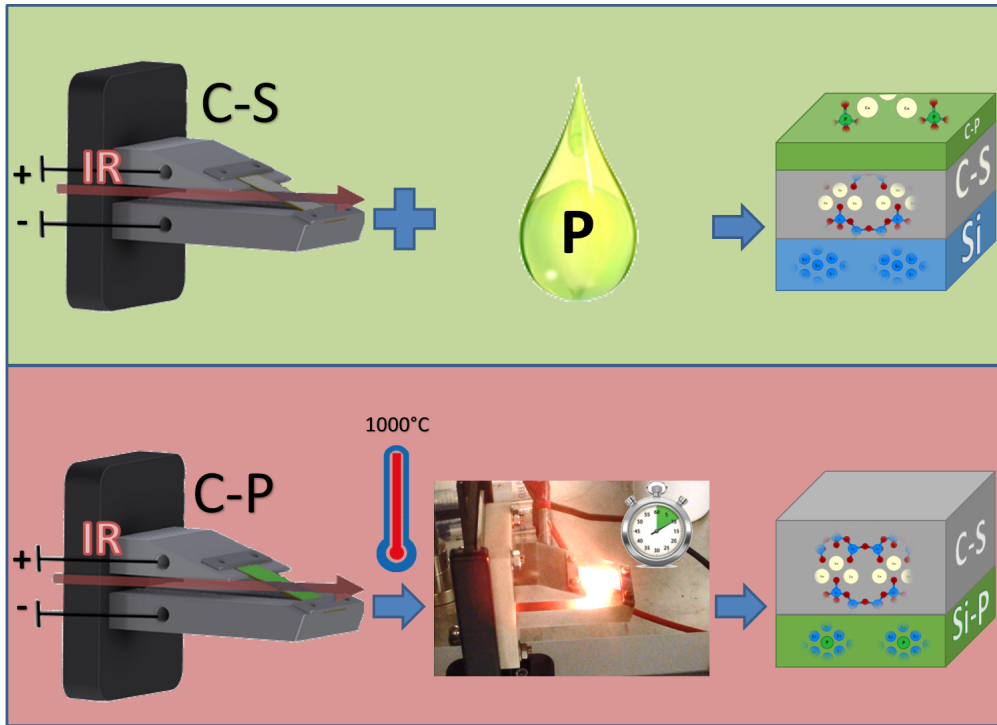


Figure 8: Representation of reactions involved in the implementation of probe molecules: the deposition of phosphate probe molecules on C-S phases and the heating process causing the diffusion of phosphorus into the silicon.

that are stable in the structure. Then, by means of four different experimental handling techniques, the C-S-H phases are activated by disposing the carbonate termination: (1) UV-light (365 nm) radiation as a function of time, (2) direct heating between room temperature (RT) and 840 °C, (3) wet chemical treatment by an aqueous solution with a defined pH value as a function of time and (4) Ar/O₂-plasma treatment as represented in the figure 7. Fourier Transform Infrared (FTIR) spectroscopy is implemented to confirm that every method is successfully reducing the carbonate termination of the ultrathin C-S-H phases. Interestingly, the effects of the diverse treatments on the C-S-H phases are very different.

- High temperature resistant phosphate molecules are also applied to describe the synthesized ultrathin (100 nm) C-S phases as presented in the chapter 6. The interaction of phosphates with the C-S phases is studied by means of in-situ transmission FTIR as summarized in the figure 8. At room temperature the chemistry of the system is dominated by the formation of Calcium-Phosphates (C-P). In case of temperatures rising up to 1000 °C, the C-S phases are regenerated. FTIR results are analyzed on the basis of first principles calculations and further supported by complementary Time-of-Flight Secondary Ion Mass Spectrometry (ToF-SIMS) experiments. This study provides a detailed and self-consistent picture of the chemical and structural properties of interfaces like the one between the atmosphere and ultrathin C-S phases (gas/C-S) and the one between them and silicon wafers (C-S/Si bulk). The

material combination of ultrathin C-S phases grown on silicon wafers might in the future have great potential in selective chemistry, catalysis and sensing technologies as well as in the semiconductors manufacture.

2 Metal-Proton Exchange Reaction (MPER)

The contents of this chapter were adapted from the published article :“Early Stage Hydration of Wollastonite: Kinetic Aspects of the Metal-Proton Exchange Reaction” with permission from The Journal of Physical Chemistry C. Copyright (2015) American Chemical Society.³⁰

2.1 Wollastonite as a Model of Calcium Silicates

In this chapter the properties of the water/Wollastonite interface are investigated, as model system for Calcium-Silicate-Hydrate (C-S-H) as well as of Calcium-Silicate (C-S) phases. C-S-H and C-S phases are the main components of hydrated cement.¹¹ At the water/Wollastonite interface, the Metal-Proton Exchange Reaction takes place, which is unique for mineral surfaces. The name of this mechanism was used for other kind of reactions as well.³⁸ Oelkers et al. investigated the MPER, finding as a conclusion that the quantity of protons to be exchanged is specifically defined by the nature of the mineral.³⁹ The consumption of protons by the MPER in Wollastonite surfaces resulted in less than 2, proposing that the amount of protons that react by the removal of Ca are less than needed to compensate for the loss of charge. Casey et al. attributed this to a repolymerisation of Si-OH sites on the Wollastonite surface during its leaching.⁴⁰ Here, this theory is expanded and the pH dependence of the MPER is proposed.

2.2 Methodology

Theoretical Considerations

The calculations presented in this chapter employ density-functional theory (DFT) as implemented in the Vienna Ab initio Simulation Package (VASP).⁴¹ The electron-ion interaction is treated within the Projector-Augmented Wave (PAW) method.⁴² The valence electron wave functions are expanded into plane waves up to the kinetic energy cutoff of 400 eV, for the kinetic analysis and 360 eV for the thermodynamic one and for the surface relaxation. This energy cutoff was found to yield converged structural parameters for both substrates. The Brillouin zone sampling was performed with $2 \times 2 \times 2$ and $2 \times 2 \times 1$ meshes of Monkhorst-Pack k-points for Wollastonite bulk and Wollastonite surfaces calculations for the kinetics, respectively, meanwhile for the crystal surfaces relaxation it was done with $1 \times 1 \times 1$.⁴³ The electron-electron exchange and correlation energy is approximated within the Generalized Gradient Approximation (GGA), using the PW91 functional.⁴⁴ It describes reliably the structure and energetics of hydrogen bonded water molecules.^{45–48} The optimization of the atomic coordinates (and unit cell size/shape for the bulk materials) was performed via a conjugate gradient technique which implements the total energy and the Hellmann Feynman forces on the atoms (and stresses on the unit cell).⁴⁹ The structures were considered to be fully relaxed when the forces on the ions were smaller than 0.01 eV/Å. To calculate the energy barrier of the reaction path of the considered cases, the Nudged Elastic Band (NEB) method was applied, for

which the images were geometrically preconfigured according to the relaxed images for the initial and final stages.⁵⁰

Supercells containing slabs of Wollastonite ($\text{Ca}_3\text{Si}_3\text{O}_9$) as well as vacuum were implemented, in order to describe the surfaces within three-dimensional periodic boundary conditions. In addition to the k-point density and plane-wave cutoff discussed above, the convergence of surface calculations also depends on the thickness of the material slab and the width of the vacuum region between the slabs.⁵¹ The convergence was tested by running a series of test calculations with different slab thicknesses and vacuum regions. Supercells containing two layers of $\text{Ca}_3\text{Si}_3\text{O}_9$ units separated by a vacuum region of approximately 20 Å between the images of the unhydrated surfaces and at least 10 Å between the images of the hydrated surfaces were found to converge. Calculations on reactants and products were performed using equivalent supercells. For calculations with charged supercells a neutralizing background charge is assumed.

Sample Preparation

A piece of Wollastonite stone was broken mechanically. The fragment was embedded into two-component resin (Araldite) and left hardening during 8 h. After curing, the sample was treated on a sapphire AMT 550 grinding and polishing machine. The granularities of the individual grinding steps using SiC grinding paper were 300, 600, 1.200, 2.500, and, finally, 4.000 (200 rpm). The sample was polished with 3 μm polycrystalline diamond suspension (150 rpm).³²

Sample Characterization

Atomic Force Microscopy (AFM)

AFM was applied for sample surface morphology characterization in air and in fluid using an MFP-3D-BIOTM (Asylum Research, Oxford Instruments). Under ambient conditions in air, a silicon NSC-35 B (MikroMasch) cantilever was used in intermittent contact mode. For fluids contact mode AFM was applied in a closed fluid cell (Asylum Research, Oxford Instruments) using cantilever 2 of the silicon-nitride PNP-TR Reflex (Cr/Au) probe (NanoWorld AG). The pH adjustment was performed using previously published methods found in Brown et al.⁵²

Inductive Coupled Plasma Optical Emission Spectroscopy (ICP-OES)

Wollastonite was mounted in a closed fluid cell with tube connections which were connected to peristaltic pump, pumping the electrolyte (100 mL) in a circle. The electrolyte was purged with argon to avoid undesirable contaminations, like the formation of carbonates. The pH value was adjusted to between 11.0 and 1.0 and aliquots of 2 mL were analyzed with the help of ICP-OES to measure the concentration of Ca and Si. This experiment was also performed with SiO_2 .

Low Energy Ion Scattering (LEIS)

LEIS measurements were done using a Qtac analyzer (ION-TOF GmbH, Münster, Germany), applying a 3.0 keV $^4\text{He}^+$ beam at a beam current of 2.3 nA and a fixed scatter angle of 145° . Each measurement lasted 120 s. The fraction of backscattered He ions was measured as a function of the kinetic energy with a double toroidal analyzer, imaging the ions according to their energy onto a position-sensitive electrostatic detector. The use of this analyzer-detector combination was important because the large scatter angle of detection combined with the parallel detection increases the sensitivity by orders of magnitude and allows a reduction of the overall ion dose needed for measurements. Consequently, the total ion dose was very low compared to the surface atomic density, and therefore, ion-induced sputtering and intermixing were negligible.

2.3 Kinetic Aspects: MPER at Different Orientations of the Wollastonite Crystal

The most important step in the MPER is the exchange of Ca by protons from water. The protons occupy such lattice sites in the crystal structure, replacing the metal in the mineral structure. The system considered here is described chemically by the equation 1.³⁹



As a first consideration of the system the kinetics of the proposed mechanism in different crystal orientations is performed. The aim of these calculations is to determine whether the reaction could be activated by lower energies at different surfaces of the crystal due to its morphology. The surface energies, of which are perpendicular to the b-axis, and therefore to the silicate tetrahedral chain, are really similar.⁵³ Thus, to perform the kinetic description of the mechanism, the considered slabs are the (010) and the (001). Since these surfaces are perpendicular to each other, these scenarios are relevant for the kinetic aspect. In (001) the Ca has to move perpendicular to the b-axis, whereas in (010) the Ca can move parallel to the b-axis.

[001] Orientation

The kinetic barrier of the minimum energy path proposed for the (001) slab is represented in figure 9 top. Each of the energy values corresponds to certain molecular scenarios, the most representatives are depicted in the figures A-C, in figure 9 bottom.

In the beginning of the reaction, the water molecules rotate to a position closer to the calcium atom, as can be observed comparing the figures 9.A and 9.B. The most remarkable result of this rotation is that in the figure 9.B the protons are 1 Å nearer to the surface than in the state represented by figure 9.A, and that the first water dissociation succeeded, having a barrier of almost 2 eV. The dissociation of the second water molecule has a lower energetic barrier, represented by the structures

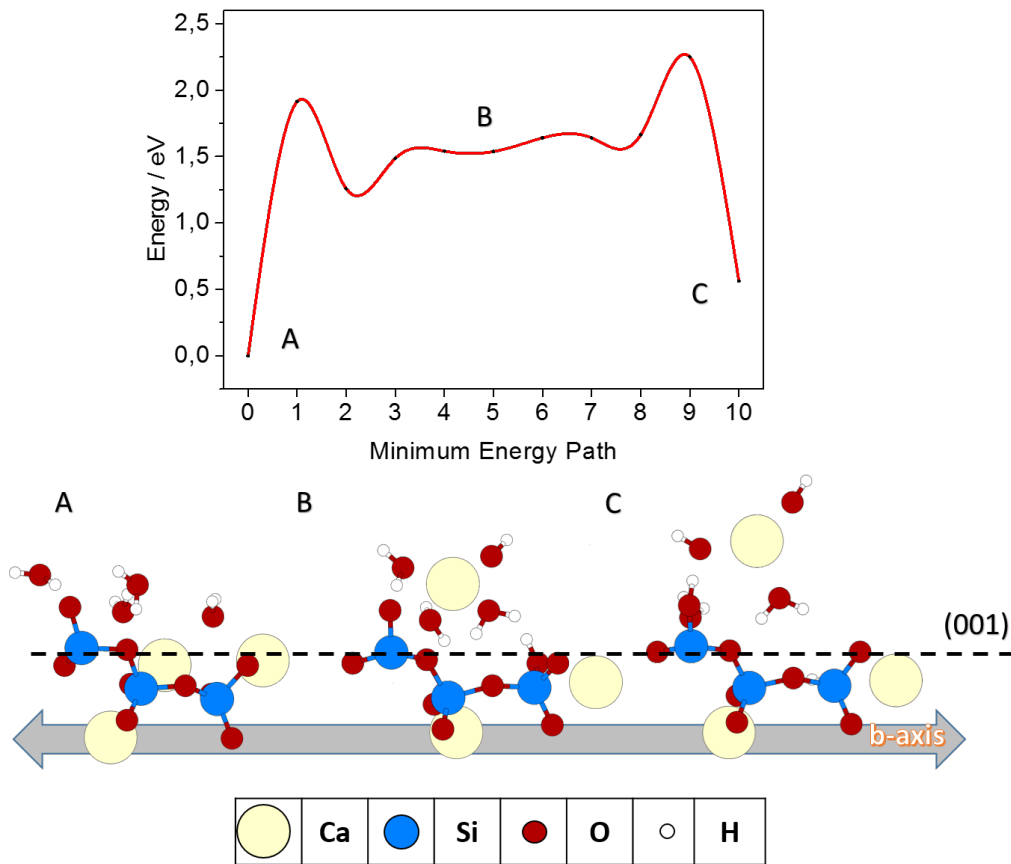


Figure 9: Kinetic barriers of the minimum energy pathway of the MPER on a (001) Wollastonite surface and their representative structures.

in the figures 9.B and 9.C, of about 0.7 eV. The final state scenario of figure 9.C shows how $\text{Ca}(\text{OH})_2$ is finally formed moving 1.5 Å away from the surface.

[010] Orientation

At the (010) surface, the Ca can move parallel to the b-axis. The kinetic barriers of the calculated minimum energy path in the case of the (010) slab is represented in the figure 10 top. Figure 10.A shows the initial state, where the four water molecules are relaxed, over the (010) Wollastonite surface. As was observed in the previous case, a water molecule rotates and dissociates between the figures 10.A and 10.B. At the same time, Ca extracted from the structure is about 1 Å higher than before. The other atoms of the structure are virtually on the same position. These changes can be interpreted as the first kinetic barrier (around 0.4 eV). The first water molecule is already dissociated and the hydrogen now bonded to the tetrahedral silicate is forming a hydrogen bridge bond with another oxygen of the tetrahedral silicate. Also in the figure 10.B, a second water molecule is close to dissociate. Figure 10.C evidences that the protons are replacing the calcium atom in the structure, which is about 2 Å higher than its original position, taking this time its OH to the way up, forming a bond with the Ca to have $\text{Ca}(\text{OH})_2$. The water molecule that was involved

in the second dissociation is now tied by a hydrogen bridge bond, attached to the surface. Figure 10.C corresponds to the final state structure, where the $\text{Ca}(\text{OH})_2$ is not grafted to the surface and the H_2O molecule found their relaxed spots on the surface. The kinetic barrier to be overcome for the second step is of 0.82 eV.

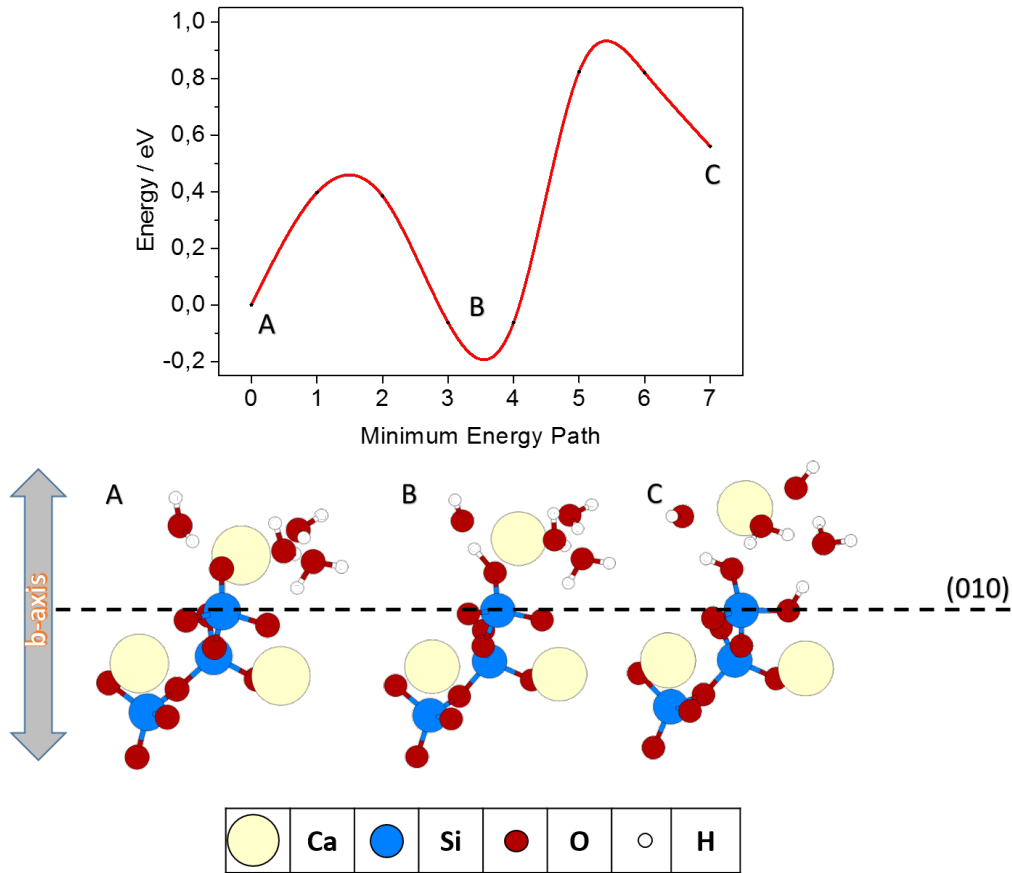


Figure 10: Kinetic barriers of the minimum energy pathway of the MPER on a (010) Wollastonite surface and their representative structures.

Regarding the results of both calculations, it can be concluded that the MPER on Wollastonite is energetically more favorably at (010) surfaces than at (001) surfaces. The energy of the dissociation of water molecules is the same in both cases, but in the (001) surface, the Wollastonite has to relax the Ca into a different position to exchange it with protons.

2.4 Thermodynamic Aspects: Non-stoichiometric Ground State of Wollastonite

Once the kinetics of the system in different orientations are considered, the thermodynamic dependencies of the whole mechanism have to be analyzed. In presence of water the MPER is initiated and results in a non-stoichiometric thermodynamic ground state of the interface. A detailed description of the thermodynamic methodology can be found in Sanna et al.¹⁰ The chemical potentials $\mu(A_i)$ of the surface

constituents A_i have to be taken into account in order to compare interfaces with different stoichiometry energetically. The ground state of the surface is determined by the minimum of the thermodynamic grandcanonical potential Ω :

$$\Omega = F - \sum_i \mu(A_i) n_i + q(E_F + E_{VBM}) \quad (2)$$

where n_i is the number of constituents, $F = E - TS$ is the surface free energy. Here, it is approximated by the total surface energy E assuming similar entropy contributions S for different adsorption configurations and T is the temperature. In fact, the differences in vibrational free energy and electronic entropy are typically several orders of magnitude smaller than adsorption energies resulting from chemical bond formation as found in the present case. The last term on the right side accounts for the energy changes due to a possible surface charge q in dependence on the chemical potential of electrons given here by the Fermi level (E_F) measured relative to the valence-band maximum (E_{VBM}) of Wollastonite. The case is considered, where the surface is in equilibrium with bulk water but vary the pH-value. For computational reasons, the calculations were thereby limited to a water thin film of monolayer thickness adsorbed on the (001) Wollastonite surface. The stability of various stoichiometries is studied as well as surfaces with varying surface charge. In the following a nomenclature is implemented where W_{xyz} refers to a structure that has x Ca atoms less and y additional hydrogen atoms adsorbed per unit cell with respect to a stoichiometric surface; z denotes the surface charge. In order to assess the stability of the numerous model structures that were probed again, the thermodynamic grandcanonical potential was investigated. However, now additional degrees of freedom are included: not only the number of water molecules, but also the numbers of surface Ca and O atoms as well as H and electrons are not the same anymore for different structures. The respective chemical potentials are not independent from each other:

(i) The sum of the chemical potentials of the surface constituents Ca and O is here assumed to equal the chemical potential of the CaO bulk

$$\mu(CaO)_{bulk} = \mu(Ca) + \mu(O) \quad (3)$$

(ii) the chemical potentials of oxygen and hydrogen are related to the chemical potential of water

$$\mu(H_2O) = 2\mu(H) + \mu(O) \quad (4)$$

(iii) the chemical potential of hydrogen is related to the chemical potentials of electrons and protons

$$\mu(H) = \mu(e^-) + \mu(H^+) \quad (5)$$

(iv) where the latter in turn is related to the pH-value by

$$\mu(H^+) = \mu_0 - pH * 0.05918eV \quad (6)$$

where μ_0 contains the proton solvation enthalpy in water. The pH-value determines the chemical potential of protons via equation 6, that directly enters the grand canonical potential given by equation 2. For the present calculations we assume the

chemical potential of electrons, i.e., the Fermi level, to be fixed at the valence-band maximum (E_{VBM}) of the ideal Wollastonite crystal. The latter is calculated from the energy difference between a slightly charged ($q=0.001$ e) and neutral unit cell

$$E_{VBM} = \frac{E_{bulk}^0 - E_{bulk}^{0.001}}{0.001} \quad (7)$$

If the water chemical potential is approximated by the respective value for bulk ice $\mu(H_2O)_{solid}$, the stability of the various structures can be directly compared for a given pH-value. A word of caution is certainly in order with respect to the phase diagram calculated based upon these approximations: apart from slight deviations of the chemical potentials due to chemical reservoirs that differ from the assumptions made here, temperature effects are neglected and the necessarily limited number of structures and charge states that can be considered will impair its predictive power. In particular the limitation to structures that have the periodicity of the Wollastonite (1×1) surface unit cell represents a severe limitation. Still, a meaningful description of the chemical trend is expected.

The resulting phase diagram is shown in figure 11. The dash lines represent the isoelectrical points of CaO and SiO₂ as published by Sanna et.al.¹⁰ The results show that the (001) Wollastonite surface, in the presence of water, changes its chemical stoichiometry in order to reach the thermodynamic ground state. It occurs already at basic pH value (W_{12-1} in figure 11). The (001) Wallastonite surface in contact with neutral and moderate acidic aqueous solution is enriched in Si-OH sites relative to the composition of the bulk mineral (W_{24-1} on figure 11) among the structures investigated, W_{12-1} was found stable from neutral to basic conditions, while W_{24-1} is favored for more acid milieu.

2.5 Experimental Confirmation of Theoretical Findings

Inductive Coupled Plasma Optical Emission Spectroscopy

At the experiments performed, different values of Ca and Si concentrations were obtained, varying the pH values. The obtained results are depicted in the figure 12.A, where the red curves correspond to the red Y axis and the blue curve responds to the blue one. Both Y axis have the same scale and can be directly compared. The blue points represent values of Ca concentrations of Wollastonite measured at varying pH values. The red diamonds depict the Si concentration of Wollastonite as reference system. With respect to the MPER, the concentration of Ca is higher than the Si concentration in the aqueous medium at every pH value. The red squares represent the concentration of Si which was measured in the aqueous medium with SiO₂ as a reference system. Beyond a shadow of doubt one can find a clear relationship between the two materials: both are most stable in the neutral regime of pH values. Considering the SiO₂, the classic hydrolyzing curve of silicates is observed, as seen by C.J. Brinker.⁵⁴ While SiO₂ is also known to be etched in the basic regime of high pH values, Wollastonite was found to be as stable as in the neutral pH regime. This can be explained by strong cohesion of the Ca placed between the silicate chains.⁶ With the same data, the relation of proton concentration and Ca exchange can be represented. The figure 12.B shows the ratio. Ca from Wollastonite is exchanged

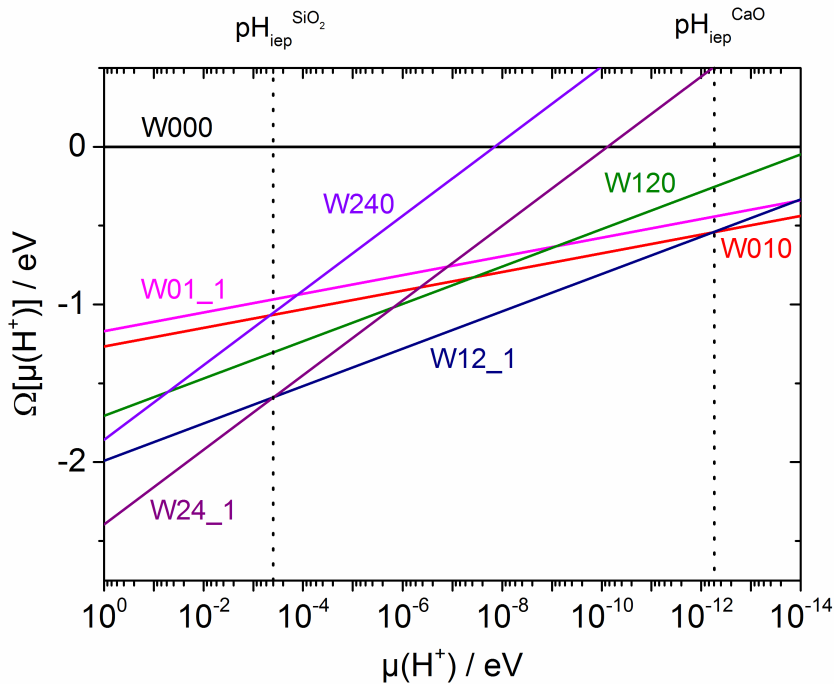


Figure 11: Calculated phase diagram of the water-(001) Wollastonite surface interface as a function of the pH value. For clarity, only the most favorable structures are shown.

differently by changing the pH values of the solution. A good agreement with the predicted values is found in the basic and neutral regime (pH values from 14-4), the increasing mismatch that appears in the acidic regime (pH value lower 4) will be explained at the following experimental analysis by a non-equilibrium etching that dominates over the MPER.

Atomic Force Microscopy

In figure 13, 90 μm x 90 μm AFM overview scans show the stability of the Wollastonite in neutral (pH = 6.7) and slightly acid (pH = 3.3) regimes. While no considerable changes in surface morphology are detectable here, in the case of pH = 1.3 a significant change in surface morphology is observed, which can be only explained by an etching process, which was not considered in the theoretical prediction so far. Within the large scan images, green squares indicate the zoom-in areas for additional 20 μm x 20 μm scans (shown below), including equidistant height cross sections spanned between unmodified positions (red line). These cross sections visualize the changes in surface morphology. However, the differentiation whether this is due to material erosion or due to deposition cannot be performed by the system. Nevertheless, an anisotropic behavior can be detected, considering that the measurements were done in a (001) Wollastonite surface, where the Ca moves perpendicular to the b-axis. The relationship of the rates of the reaction at different surfaces can be calculated using DFT kinetic barrier values E in the Eyring equation of the transition state theory (TST), represented in equation 8.⁵⁵

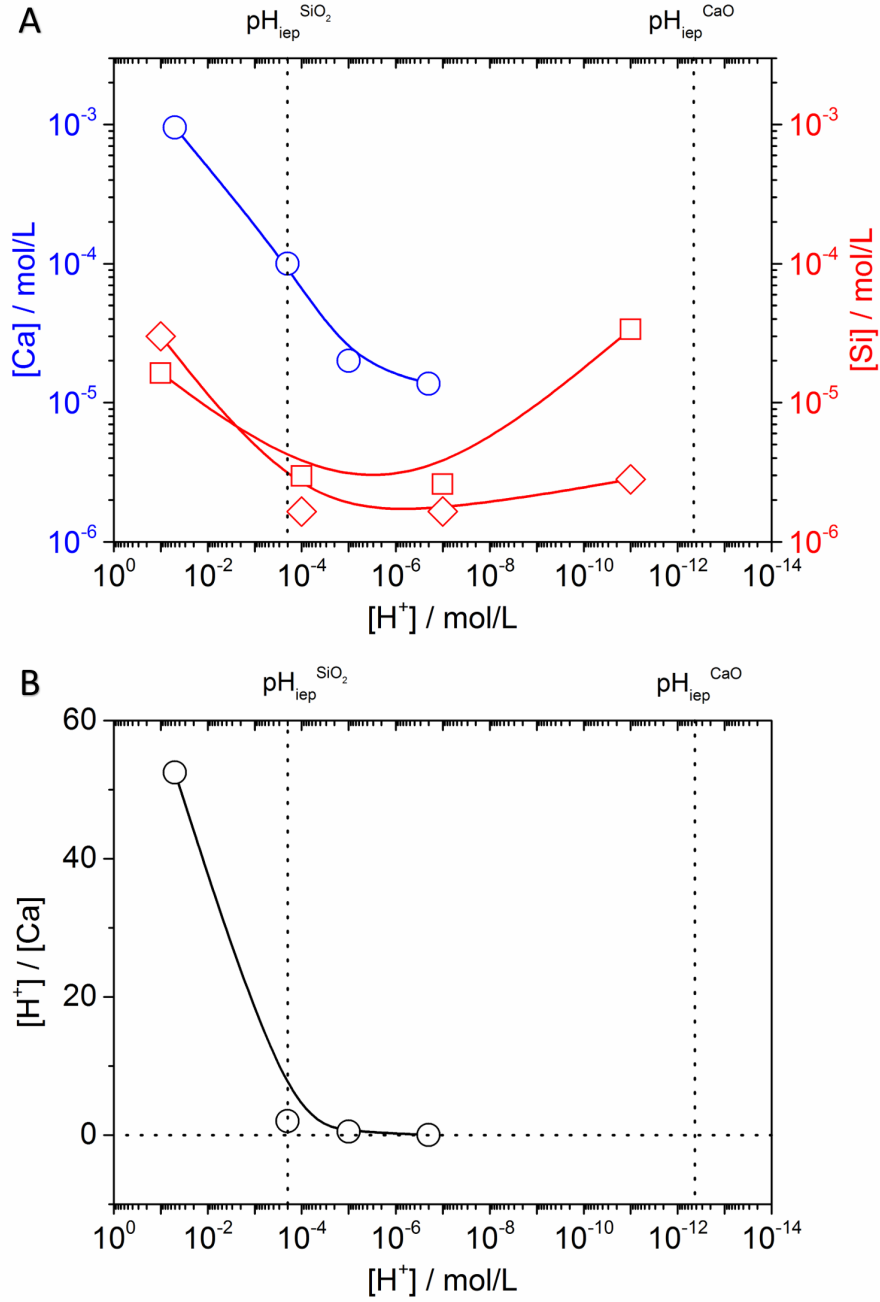


Figure 12: (A) Concentration of Si and Ca as function of concentration of protons; measured with the help of Inductive coupled plasma atomic emission spectroscopy. (B) Number of protons consumed by the preferential exchanged Ca as a function of the pH value applied at the water/Wollastonite interface.

$$k = \left(\frac{k_B * T}{h} \right) * e^{\left(\frac{-E}{RT} \right)}, \quad (8)$$

where k_B is the Boltzmann constant, T is the temperature, h is the Planck constant and R is the gas constant. As energy of activation (E), the highest kinetic

barrier value of the MPER at each surface was taken. Thence, a ratio between k_{001} and k_{010} can be obtained. The ratio k_{010}/k_{001} , is about 1×10^{24} . That means that at the same conditions and at room temperature, the reaction along the b-axis (surface (010)) is almost 10^{24} times faster than in the perpendicular direction. Of course these obtained values are not the exact rates of the MPER, since there are many more factors involved in this process (e.g., the rate is not constant), but it provides a first estimation of the rate.

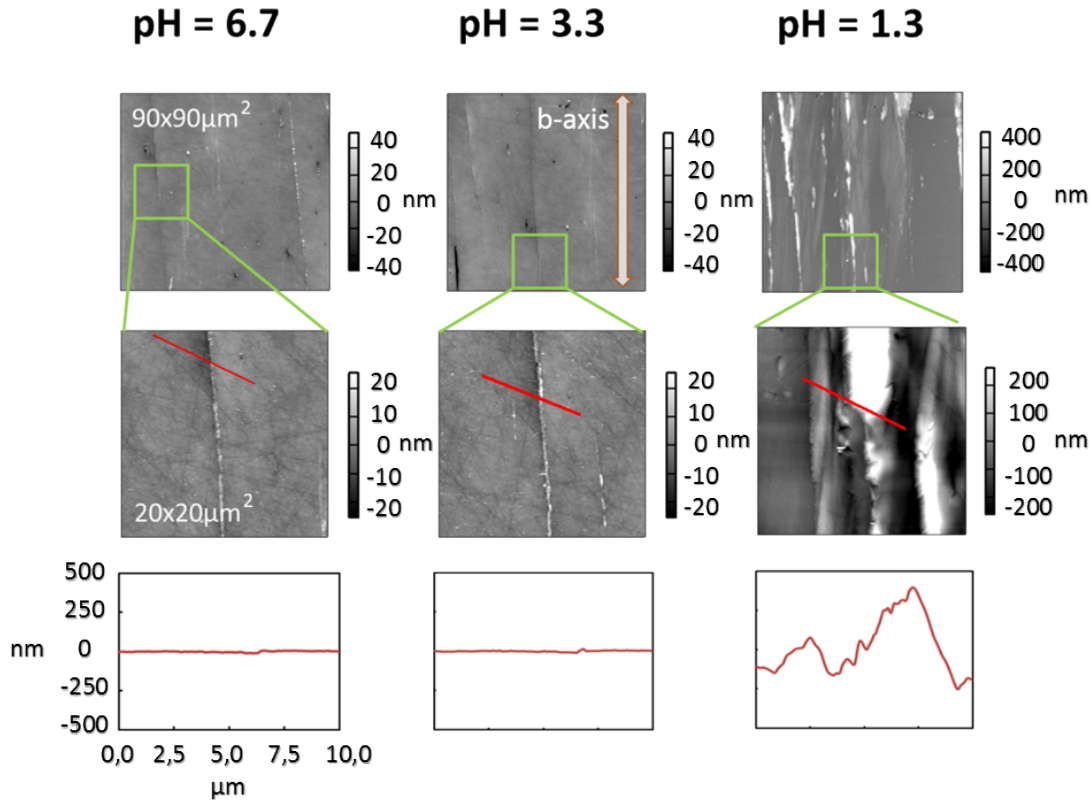


Figure 13: AFM topographies and cross sections at different pH values of the water-(001) Wollastonite surface interface. Upper line images represent scans of $90 \mu\text{m} \times 90 \mu\text{m}$. Middle line images represent scans of $20 \mu\text{m} \times 20 \mu\text{m}$ with cross sections marked by solid red lines.

Low Energy Ion Scattering

Additional measurements are performed by means of low energy ion scattering (LEIS). In figure 14.A and 14.B, the measurements on (001) Wollastonite and (010) Wollastonite surfaces directly after the transfer from the atmosphere are shown, respectively. In this way, different orientations of the MPER with respect to the b-axis can be analyzed. Afterwards, the surfaces are exposed to hydrochloric acid (HCl) and measured again.

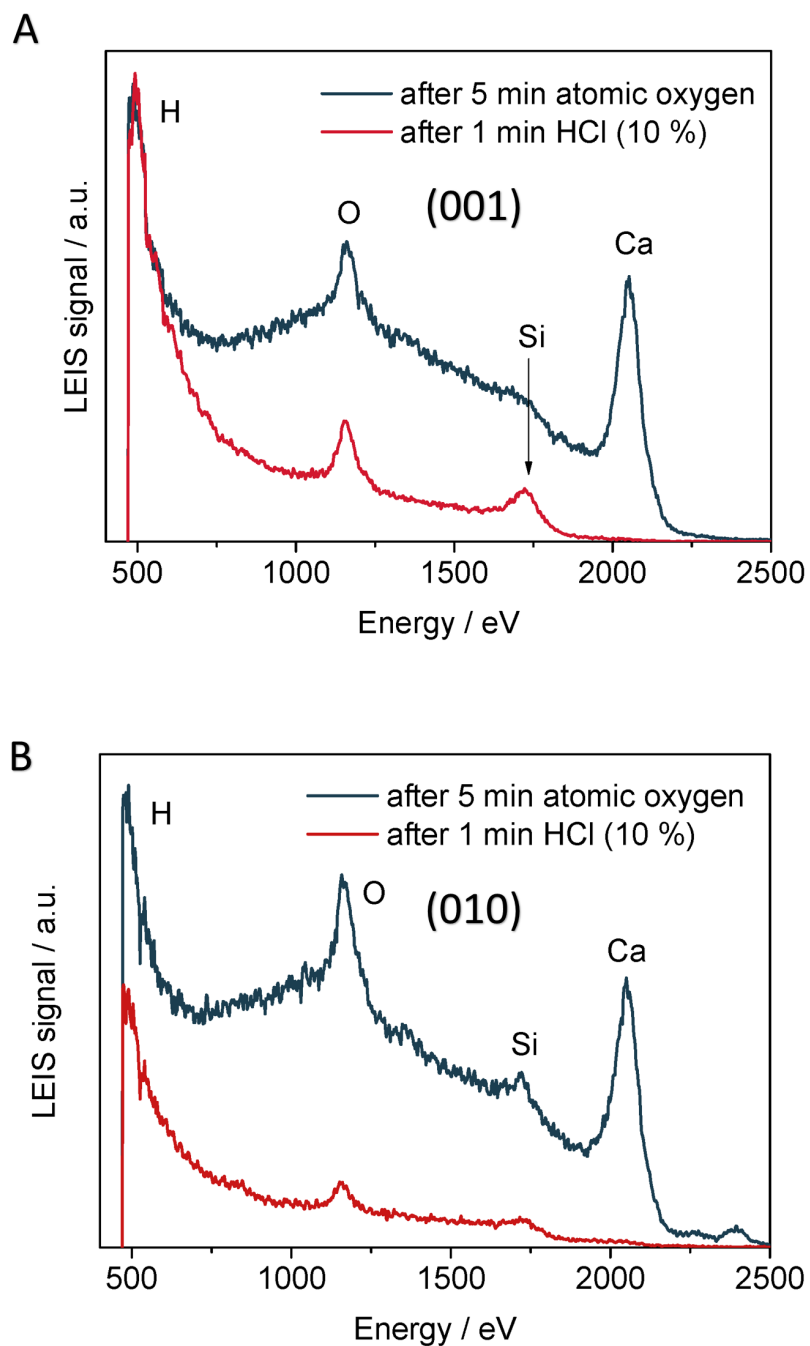


Figure 14: (A) Low energy ion scattering measurements performed on (001) Wollastonite surface before (blue curve) and after exposition to HCl (red curve). (B) Low energy ion scattering measurements performed on (010) Wollastonite surface before (blue curve) and after exposition to HCl (red curve).

Low Energy Ion Scattering

The red line depicts the measurements after the exposure to HCl. The LEIS intensity is proportional to the surface coverage. With the help of the obtained intensity values, some differences between the employed model of the (001) Wollastonite surface (figure 14.A), and the (010) Wollastonite surface (figure 14.B) can be discussed. The Ca/Si ratio after exposure to HCl appear most interesting. In case of the (001), the concentration of Ca is dependent on the transport mechanism from the bulk material ($\text{Ca/Si} = 1$) to the surface ($\text{Ca/Si} = 0.1$). Since (001) is measured, the transport of the Ca has to run perpendicular to the b-axis. In accordance with the result of the kinetic barrier calculation of the MPER (see figure 9 and 10), it slows down the whole process. The (010) has a Ca/Si ratio in the bulk phase of 1 and at the surface after exposure to HCl of 0.3 (3 times higher than at the (001), anisotropic affect). This is only possible with a different/better transport mechanism in the bulk phase (parallel to the b-axis) compared to the (001) surface. Anisotropic characteristics at the MPER are the first step to understand the nanocrystalline structure of macro amorphous cement.

2.6 Summary

In this chapter the kinetic and thermodynamic aspects of the Metal-Proton Exchange Reaction were investigated using Wollastonite surfaces in contact with water as a model system. A was observed by Longo et al. "In presence of water the Metal-Proton Exchange Reaction (MPER) is happening and leading the Wollastonite surface to a non-stoichiometric thermodynamic ground state in equilibrium with a $\text{Ca}(\text{OH})_2$ solution."³² The exchange of Ca with protons of water was characterized proposing different values to define the amount of protons consumed at the exchange of each Ca from the Wollastonite surface (protons/Ca). In the basic and neutral pH regime a number lower than 2 was found for that ratio. In the moderate acidic pH regime the number 2 was found and in the acidic pH regime a number higher than 2 was found. While a good agreement between the thermodynamic model and experimental results was found in the basic and neutral regime (pH values from 14-4), an increasing mismatch appears in the acidic regime (pH value lower 4). This is finally explained by non-equilibrium etching (seen in the in-situ AFM measurements), dominating over the MPER in the very acidic regime. On the (010) Wollastonite surfaces, the reaction occurs with a smaller kinetic barrier than on (001) surfaces, which explains the effect of anisotropy. The consideration of these anisotropic characteristics in the corrosion will be the first step to understand it and control it.

3 Corrosion Induced by Water: Detection by Shape Changes

The contents of this chapter were adapted from the published article: “Corrosion of Concrete by Water-Induced Metal-Proton Exchange” with permission from The Journal of Physical Chemistry. Copyright (2016) American Chemical Society.⁵⁶

3.1 Wulff Construction

As it was explained in the last Chapter, the Metal-Proton Exchange Reaction (MPER), schematically represented in figure 15, controls the corrosion of concrete induced by water.³⁰ A straightforward way to predict the equilibrium shape of particles from the free energies of the different surface orientations is provided by the Wulff construction.⁵⁷ Application of this method yields the thermodynamic most stable shape for a particle in equilibrium with the environment.^{58–59} While most Wulff constructions are reported for particles in equilibrium with the vapor phase, recently, also equilibria with other environments have been considered. Such calculations represent a major challenge, since in order to obtain the corresponding surface free energies, e.g. via DFT, a water layer with sufficient thickness has to be included in the calculations. As a result, DFT-based Wulff constructions for materials in aqueous environments have only been reported in a few cases, e.g for MgO.^{10,60}

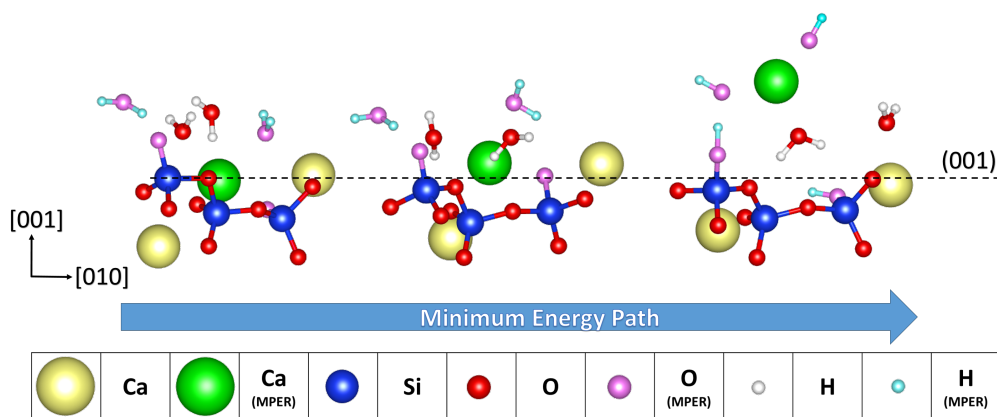


Figure 15: Metal-Proton Exchange Reaction (MPER) on a (001) Wollastonite surface.

In this chapter, the outcome of XRD experiments is analyzed, which allows to determine the shape of micrometer-sized powder particles before and after immersion into water. Subsequently, Wulff constructions for two materials, α -SiO₂ and Wollastonite, are presented. While for α -SiO₂ the water-induced changes are minuscule, as expected, substantial changes are observed for Wollastonite. Surprisingly, however, the predicted changes in the shape of the Wollastonite-particles are not consistent with the experimental XRD results. Expanding the Wulff construction by explicitly considering kinetic control a consistent picture of experimental and theoretical findings can be provided.

3.2 Methodology

Sample Preparation

Wollastonite powder particles with dimensions of less than 20 μm were produced by milling of a mm-sized natural crystal and subsequent sieving. After characterization with XRD, the powder was immersed in an aqueous HCl solution (pH 4.3). The solution was continuously purged with argon in order to avoid unwanted reactions other than MPER, e.g. carbonation.³² After 5 minutes of purging the recipient was closed. After reaction times of 24 and 48 hours the suspension was filtered. The powder remaining on the filter paper was dried to constant weight and immediately characterized again with XRD. Aliquots of the solution were analyzed by inductive coupled plasma optical emission spectroscopy (ICP-OES) to determine the amount of calcium which had been leached out from the powder.

X-ray Diffraction (XRD)

Out-of-plane XRD measurements were carried out with a Bruker D8 Advance in Bragg-Brentano geometry ($\theta - \theta$ setup) by employing a PSD Lynxeye (192 Si-strips) detector equipped with a 9-fold sample holder. Cu-radiation was implemented (κ -alpha). A scan speed of 0.2 seconds/step and a step size of 0.01° were taken as standard parameters. Diffracted intensities were recorded in an interval between 10° and 70° . For all measurements the same sample holder was used.

Environmental Scanning Electron Microscopy (ESEM)

A Philips XL30 ESEM-FEG operated at 20 kV was used for imaging the samples.

Theoretical Determination of Surface Free Energies at the Solid/Vacuum and Solid/Water Interface

All ab-initio electronic structure calculations reported here were carried out using Density Functional Theory (DFT) as implemented in the Vienna Ab initio Simulation Package (VASP).⁶¹ The electron-ion interaction was treated within the Projector-Augmented Wave (PAW) method.⁴¹ The plane waves into which the valence electron wave functions are expanded have a kinetic energy cutoff of 360 eV. This energy limit yielded converged structures for all calculations. The Brillouin zone sampling was completed with $2 \times 2 \times 1$ meshes of Monkhorst-Pack k-points.⁴³ The electron-electron exchange and correlation energy was approached making use of the PW91 functional contained in the Generalized Gradient Approximation (GGA), which in previous work has been found to reliably describe the structure and energetics of hydrogen bonded water molecules.^{44–48}

Every slab used for the calculation of free surface energies was extended and relaxed from a single crystal, which was optimized with the third order Birch-Murnaghan equation of state. In order to assess the stability of the numerous model structures and different surface orientations, the thermodynamic grandcanonical potential was investigated, using previously published methods found in Sanna et al. and explained in the chapter 2.¹⁰ For the corresponding calculations, it is important

to note that not only the number of water molecules but also the number of surface Ca and O atoms as well as H and electrons are different for the different structures.⁶²

Additional anions like chloride have not been considered in these calculations.

3.3 Experimental Observation of Shape Changes

The Lorentzian fitting of the XRD peaks recorded for the Wollastonite particles before and after immersion to the aqueous solution are shown in figure 16.⁶³ While the positions remain unchanged, the width of the peaks showed a significant variation. These changes in width result from a change of the size of the coherent scattering domains (CSD) along the corresponding crystallographic directions also provided in figure 16. A broadening of a particular XRD-peak reveals a decrease of the CSD-size along the corresponding direction.⁶⁴ Scherrer's equation can be used to quantitatively determine the average CSD-size from the FWHM (full width half maximum) value:

$$\beta(2\theta) = \frac{K\lambda}{L\cos\theta} \quad (9)$$

where, β is the FWHM, after subtracting the instrumental line broadening. K is the constant of the proportionality (Scherrer constant). λ is the wave length. L is a volume average on the CSD thickness in the direction normal to the reflecting planes. The changes on the FWHM observed in the figure 16, resulting from a fitting with a Lorentzian function are: from 0.052 ± 0.001 to 0.073 ± 0.003 for (200), from 0.061 ± 0.001 to 0.090 ± 0.003 for the (002) and from 0.100 ± 0.003 to 0.089 ± 0.003 for (120) before and after 24 hours MPER, respectively.

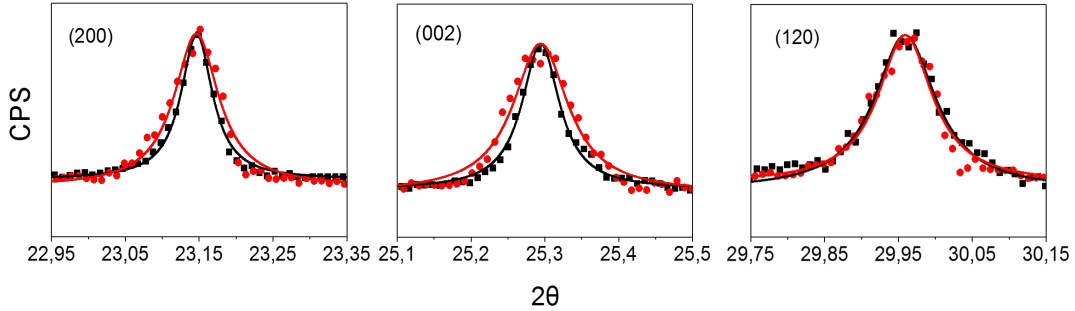


Figure 16: XRD pattern of Wollastonite (black) before MPER and (red) after 24 hours MPER.

In the microstructure of Wollastonite, both, the [100] and the [001] orientations run perpendicular to the so-called b-axis. Strong changes of the CSD sizes appear as a result of the immersion of Wollastonite in water for 24h. Interestingly, both (200) and (002) domains change in a similar way, becoming smaller (broader peaks) upon immersion in water. In contrast to that, changes on the (120) domain are negligible. Measurements recorded after 48h of immersion showed that Wollastonite particles

became amorphous, in good agreement with recent literature.⁷ Corresponding experiments for α -SiO₂ particles immersed in the same aqueous solutions revealed no changes in XRD peak shapes.

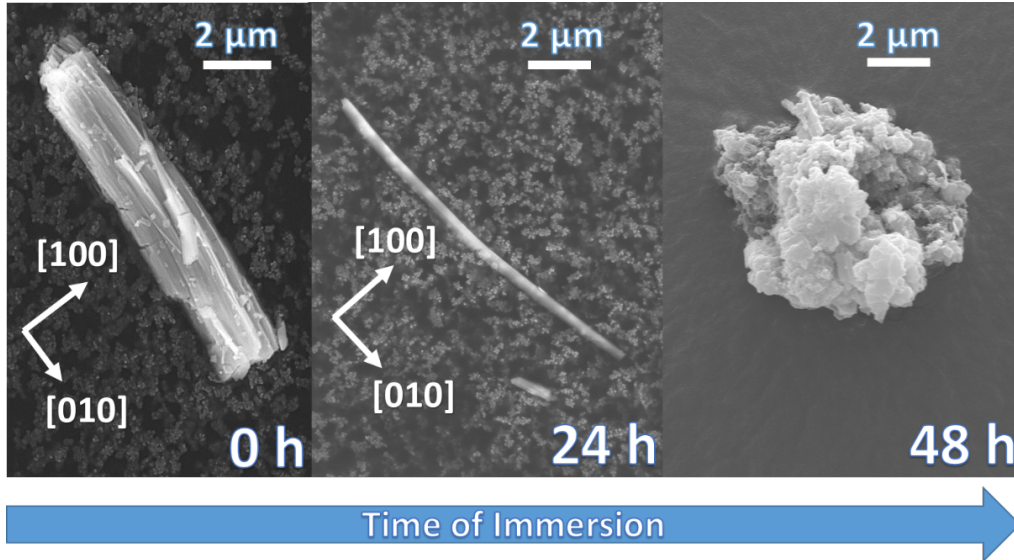


Figure 17: ESEM captions of selected representative particles of the Wolastonite powder at different times of immersion into water.

Figure 17 shows selected ESEM pictures recorded for particles after different periods of exposure to water corrosion. The initial structure of the particles after the grinding process is rather elongated. Similar nail-shapes have been reported in earlier studies.^{7,65} After 24 hours of immersion in the solution, MPER has clearly changed the shape of the particles, that now reveal a needle-like form. The CSD-data reveal that the extension along the 010-directions has decreased substantially. After 48 hours of immersion most particles are amorphous, in full agreement with the XRD results.

3.4 Theoretical Evaluation of the Shape Changes

In this section the theoretical description of particle shapes in thermodynamic equilibrium with the environment will be developed. The first step in building a Wulff construction is to determine the total free surface energy γ of the most important surface orientations.¹⁰ γ is defined as

$$\gamma = \frac{E_{sl} - n * E_b}{2A} \quad (10)$$

where E_{sl} is the free energy of the slab; n is the number of unit cells used to build the slab, E_b is the free energy of the unit cell of the bulk, and A is the area of the slab. In case of α -SiO₂, the calculated surface energies are 2.5 J/m² for (001) and to 1.6 J/m² for (100) and (010). These values are in good agreements with previously published results.^{66–68} After adsorption of water, the values of the surfaces energies of α -SiO₂ change to 8.8 J/m² for (001) and to 4.0 J/m² for (100) and (010).

In figure 18 the Wulff constructions of clean α -SiO₂ (A) and α -SiO₂ after adsorption of water (B) are depicted. In case of α -SiO₂ the water molecules are just adsorbed on the surfaces and no strong chemical interactions are present. Consequently, the water-induced changes in shape are negligible.

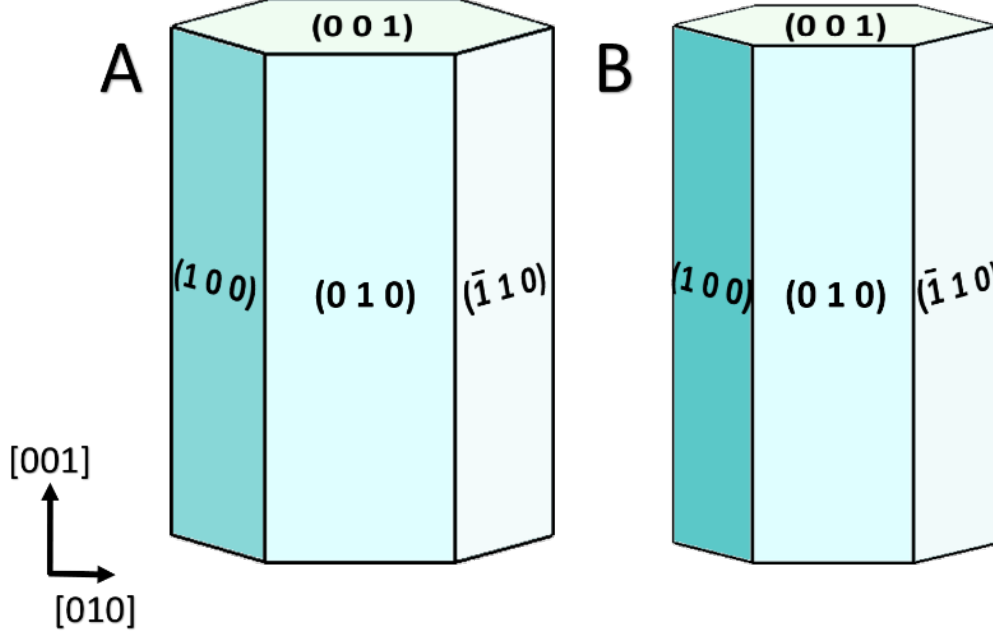
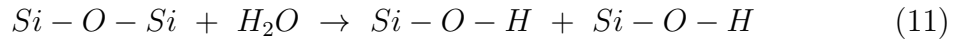


Figure 18: (A) Wulff construction of clean α -SiO₂. (B) Wulff construction of α -SiO₂ after water adsorption.

For the calculations of Wollastonite slabs it is crucial that both sides of the slabs (top and bottom) exhibit the same surface termination. Among the different orientations studied in case of Wollastonite, special care has to be taken for the (010) orientation. All orientations that are not running parallel to the b-axis will create unit cells where the chains of Si-O have to be interrupted. In order to saturate the resulting dangling bonds, a H₂O molecule was added to the unit cell,



and the total free energy of the slab was adjusted accordingly:

$$E_{(010)}^{water} = E_{(010)} - n_{H_2O} * \mu(H_2O) \quad (12)$$

where $E_{(010)}$ is the free energy obtained from the calculations for the (010) surface, n_{H_2O} is the number of water molecules integrated into the model, $\mu(H_2O)$ is the chemical potential of the water.

In case of Wollastonite, the calculated surface energies are 0.04 J/m² for the (001) surface, 0.08 J/m² for the (100) surface, and 0.29 J/m² for the (010) surface. As a result of the MPER, the thermodynamically most stable state of Wollastonite surfaces changes when brought in contact with water, the new values are 3.85 J/m² for the (001) surface, 3.12 J/m² for the (100) surface, and 7.80 J/m² for the (010) surface orientation. More important than the absolute changes are the relative

changes: ratio of the surface energies before MPER (001/100/010) is (1/1.8/6.8) and after MPER it is (1.2/1/2.5).

In the figure 19 the Wulff constructions of Wollastonite (A) before and (B) after the reaction with water are depicted. Dramatic changes in particle shape are the result of the so-called MPER. The ratios between the orientations are 7:1 for the (010) relative to the (001) before MPER and 3:1 for the (010) relative to the (100) after MPER. These ratio clearly demonstrate that the particles are getting less elongated in the b-axis direction.

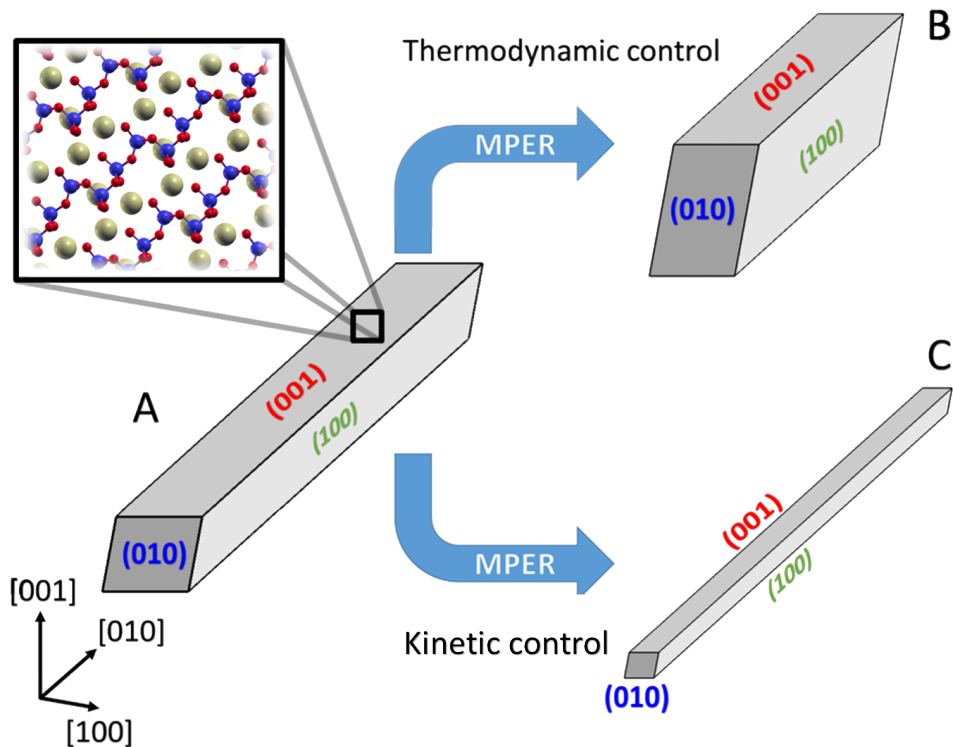


Figure 19: (A) Wulff construction of clean Wollastonite. (B) Wulff construction of Wollastonite after MPER. (C) Wulff construction of Wollastonite after MPER with detailed kinetic analysis.

Surprisingly, these changes in the aspect ratios do not agree with the XRD results, since along the [010] direction, the calculations predict a decrease in CSD diameters, whereas the corresponding XRD-data show no change at all. This unexpected discrepancy serves as an indicator that the changes in the shape of the micrometer-sized Wollastonite particles in aqueous environments cannot be understood on the basis of thermodynamic arguments alone. The equilibrium shapes are not reached and the possibility of kinetic limitations has to be considered.

As has been demonstrated in the chapter 2, the kinetic constants k_{001} , k_{010} and k_{100} of the MPER occurring along the [001], [010] and [100]-orientations, respectively, can be computed using Transition State Theory (TST) by the Eyring model. One of the most important conclusions of the last chapter was that k_{010}/k_{001} is so large, that the MPER on (001) and (100) surfaces did not take place on the time-scale (12 h) of

the experiments. Furthermore, k_{100} and k_{001} can be assumed to be equal.³⁰ Note the substantial difference in chemical behavior between surfaces oriented perpendicular to the silicate chains and surfaces not cutting through chains.

The ratio of the surface energies before MPER (001/100/010) is (1/1.8/6.8) and after kinetic MPER is (1/1.8/16.2). In the same figure 19 the Wulff construction of clean and the kinetic controlled model of Wollastonite after MPER (C) is depicted. Now, a consistent picture of experimental and theoretical results is found.

The Metal-Proton Exchange Reaction on Wollastonite is responsible for Calcium removal from the structure, being replaced by protons coming from the water, it modifies the shape of the crystals leading to their amorphization. This reaction runs faster in orientations that are perpendicular to the silicate tetrahedral chain (b-axis), and therefore affects more strongly compounds in which these orientations appear more often, namely with shorter chains.

3.5 Summary

Using XRD, substantial changes in the shape of Wollastonite particles upon immersion into water were detected. A thorough theoretical analysis revealed that these shape changes, caused by a corrosion process controlled by the Metal-Proton Exchange Reaction (MPER), cannot be explained by thermodynamic arguments alone and kinetic considerations are to be included, instead.

The observed phenomena can be rationalized using an observation reported in the last chapter, where the MPER was found to be substantially accelerated on surfaces oriented perpendicular to the b-axis of Wollastonite ([010] orientation), whereas for surfaces that are parallel to the silicate tetrahedral chains the reaction is slower.³⁰ These kinetic differences are responsible for the characteristic changes on the shape of the mineral particles when exposed to water.

Corrosion of concrete induced by MPER leads to a phase transformation of crystalline to glassy C-S-H phases, due to the before-mentioned changes in the structure. The length of the silicate tetrahedral chain plays a very important role in the mechanical properties such as stiffness and hardness of this kind of compounds, and also determines how the MPER affects their structure.

4 Calcium-Silicate-Hydrate Phases on Silicon: a New Model System

4.1 Lacks of Knowledge Filled by the New Model System

As mentioned in the first chapter of this dissertation, despite high consumption, the understanding of Calcium-Silicate-Hydrate (C-S-H) and Calcium-Silicate (C-S) phases still presents some deficiencies. Several relevant properties of construction materials have been taken into account in the last decades. Among them, the mechanical properties of different C-S-H and C-S phases are the focus of many researchers.^{31,69–70} Hydration properties were also intensive analyzed, pointing out the importance of interfaces phenomena.⁷¹ Furthermore, in chapters 2 and 3 the corrosion of concrete by water was explained, remarking the importance of the interface and the length of silicate chains.⁵⁶

The investigation of the above mentioned properties required atomic-level simulations to unveil a deeper understanding of the C-S-H phases, and their comparison.⁶ Likewise, the potential of the changes in the chemical composition, by changing the Ca/Si ratio, to modify the mechanical properties of determined C-S-H phases can be characterized.³⁵ The synthesis of thin layers of C-S-H and C-S phases on silicon wafers fills this lack of knowledge. This material combination is suitable for many fields of investigation such as the protection of construction materials applying molecules reacting with the surface, preventing or predicting the corrosion of building materials, among others.^{37,73}

The last chapter reported about the corrosion of C-S phases by water, and the following ones will describe the influence of external compounds on these phases by applying determined molecules and even about the influence of the presence of carbonates.^{30,32,56} However, the synthesis of the C-S-H and C-S phases has to be well characterized before new applications can be developed. Therefore, in this chapter, such synthesis is performed under different conditions and successfully controlled.^{36–37}

4.2 Methodology

Theoretical Methods

The model relaxation was done as explained in the last chapter for the case of Wollastonite bulk and by Longo et al.³²

Sample Preparation

A 3 cm × 1 cm Si(111) crystal was chemically cleaned with a 30 min exposure at 80 °C to a 1:3 solution of aqueous H₂O₂:H₂SO₄ (piranha solution). Afterwards, the crystal was rinsed thoroughly with deionized water with a resistivity of 0.055 μS/cm. Then, the wafer was immersed in a solution of 10 mM Ca(OH)₂ at 60 °C. Aqueous solutions of Ca(OH)₂ (1 mM, 5 mM and 10 mM) were prepared in a N₂(g) atmosphere to avoid any effects due to CO₂ contamination. Piranha-cleaned silicon wafers were immersed in the solutions of different temperatures, namely RT, 60 °C

and 80 °C. After determined periods, the samples were extracted from the solution in the protected atmosphere to avoid the formation of carbonates. Afterwards, samples were measured by means of FTIR. Methanol solutions were prepared using a concentration of 10 mM $\text{Ca}(\text{OH})_2$, the concentrations of methanol are expressed in % v/v of anhydride methanol, as bought from Merck. A schematic representation of the synthesis is shown in the figure 20.

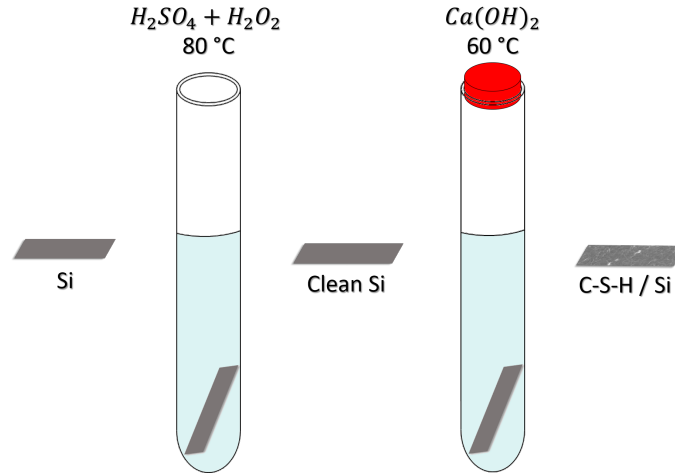


Figure 20: Schematic representation of the synthesis of Calcium-Silicate-Hydrate phases on silicon wafers.

Environmental Scanning Electron Microscopy (ESEM)

A Philips XL30 ESEM-FEG operated at 20 kV was used for imaging the samples.

Transformation of C-S-H Phases into C-S Phases

Samples containing C-S-H phases were heated up stepwise to 900 °C and measured after every increment of 100 °C. The temperature was hold 1 second at each temperature, and then cooled down and measured at 60 °C.

X-Ray Diffraction (XRD)

A Bruker D8 Advance in Bragg-Brentano geometry ($\theta - \theta$ setup) for out-of-plane measurements (coplanar geometry) with PSD Lynkeye (192 Si-strip detector), 9-fold sample holder, Cu-radiation was implemented. The scan speed was of 1 s/step with a step size of 0.02° . Diffracted intensities were recorded in an interval between 10° and 70° .

4.3 Fourier Transform Infrared Spectroscopy (FTIR)

From this point forward, FTIR spectroscopy is implemented in this dissertation as the most important technique to evaluate the changes produced in the C-S and C-S-H phases synthesized on silicon wafers. All FTIR measurements were done in

a $\text{N}_2(g)$ purged glovebox with a Bruker Vertex 70, and recorded with a nominal 4 cm^{-1} resolution. Spectra were collected from 400 to 4000 cm^{-1} in transmission mode with an angle of incidence of 64° with respect to the silicon surface normal. A room temperature pyroelectric detector (DTGS) was employed for data collection. In all experiments, 1024 scans were taken. Several considerations are to be mentioned before moving forward to the results of the application of the new model system. Single channels obtained from the FTIR measurements can be converted into spectra only if the corresponding background was measured. Therefore, the following nomenclature is applied to better interpret what the figures show:

Absolute spectrum: since measurements are performed in transmission mode, the piranha-cleaned wafer is taken as starting point for all samples. Thence, the absolute spectra are the ones, which result from taking the single channel of the piranha-cleaned wafer as background. This way, the bands from the reference material are removed. One good example of this procedure is observed in the figure 21.

Difference spectrum: on the other hand, some measurements are intended to show the changes produced by an alteration of the already synthesized C-S or C-S-H phases on the wafer. These changes can be produced by, for example, the application of temperature, UV light, chemical treatment, plasma, etc. during a period of time. Therefore, difference spectra are the ones which result from the single channels of the sample before and after those treatments. It has to be considered that the description of the background is unavoidable here to understand the meaning of the spectra. For example, the background of difference spectra shown in the figure 27 is always the previous temperature, e.g. the spectrum after $200\text{ }^\circ\text{C}$ takes the single channel after $100\text{ }^\circ\text{C}$ as background. Different is the case presented later in this chapter in the figure 40, for example, where every spectrum takes the single channel at $t=0$ as background.

4.4 Characterization of C-S-H Phases Synthesized on Silicon

Several considerations were taken into account to perform the characterization of Calcium-Silicate-Hydrate phases. The figure 21.A and 21.B show the spectrum obtained from the synthesis of C-S-H phases with the piranha-cleaned silicon wafer as background. This spectrum is separated in two figures to better distinguish the vibration modes. These phases are investigated experimentally by different methods and changing different parameters.

Concentration Dependence

In the figure 22.A a comparison of the FTIR spectra of three different concentrations of $\text{Ca}(\text{OH})_2$ solutions, namely 1 mM , 5 mM and 10 mM is presented. The concentration and the presence of the $\text{Ca}(\text{OH})_2$ on the sample does not vary linearly with the concentration. An explanation of the changes in the layer thickness respect to the concentration of the solution is discussed in this chapter.

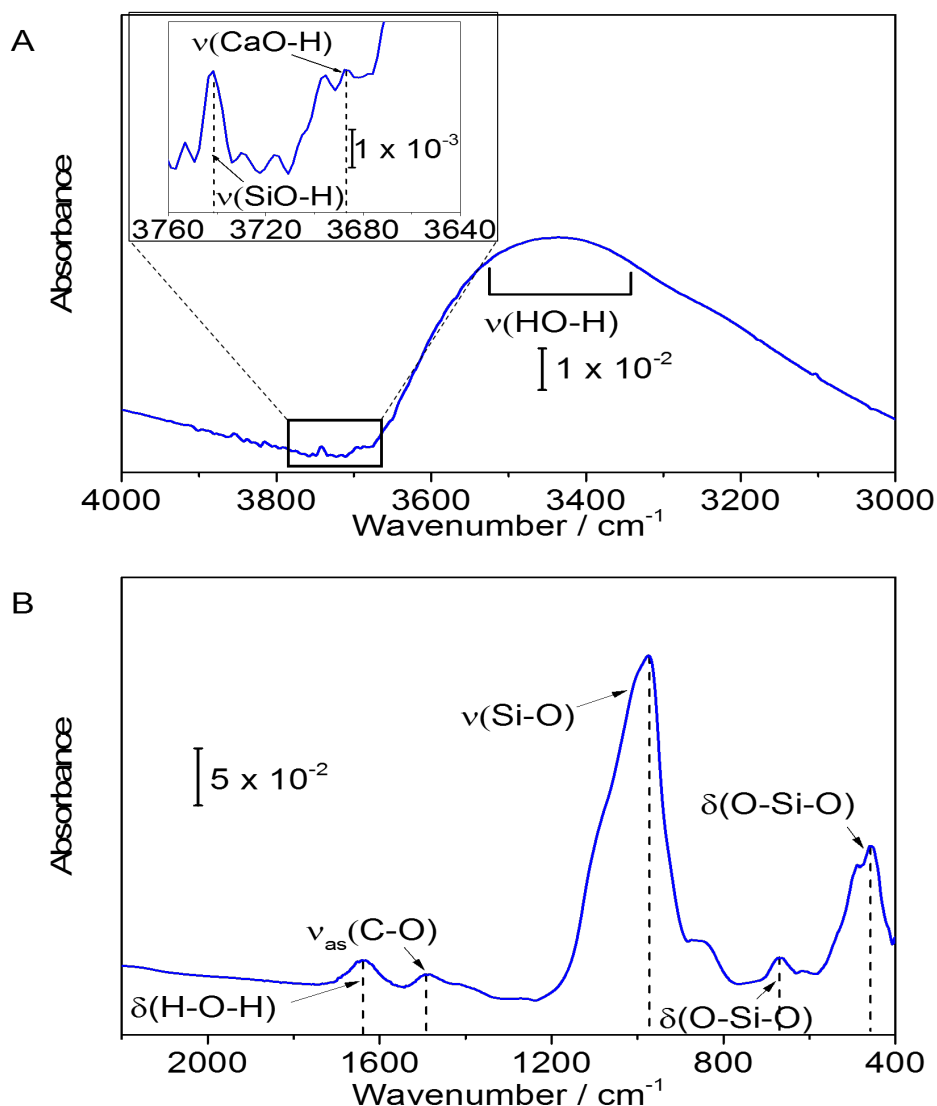


Figure 21: Absolute IR Spectrum of C-S-H phases synthesized on a silicon wafer with a 10 mM $\text{Ca}(\text{OH})_2$ solution at RT during 12 h.

Mechanism of Reaction

In the figure 22.B the spectrum of the synthesis of C-S-H after 4 hours is shown. The sample was produced implementing a 10 mM solution of $\text{Ca}(\text{OH})_2$ at RT. As can be seen the reaction starts with the etching of the SiO_2 layer, before building the calcium silicates on the surfaces. Such etching is observed by the Si-O associated vibration modes ($\nu(\text{Si-O})$ centered at 1108 cm^{-1} and $\delta(\text{O-Si-O})$ at 612 cm^{-1}). The etching of bulk Si was also detected by changes on the intensity of the transmission.

Uniqueness of the Calcium

The success of the synthesis of C-S-H phases on silicon wafers is related to the unique effect produced by the $\text{Ca}(\text{OH})_2$ solutions. After etching the SiO_2 and some of the Si bulk, the reaction reaches an equilibrium, and the SiO-H and Si-H terminations of the silicon wafers react with the $\text{Ca}(\text{OH})_2$ to build the C-S-H phases. The reaction responsible for the formation of C-S-H phases on the surface competes with another well-known reaction: the Metal-Proton Exchange Reaction (MPER).³⁰

In the figure 22.C the spectrum of a wafer in contact with a KOH solution is shown. A piranha-cleaned sample was immersed in a solution of KOH with the same pH value as a 5 mM solution of $\text{Ca}(\text{OH})_2$ (~ 10 mM KOH). After 12 h at 60 °C in the solution, no KO-H nor SiO-H is observed in the spectrum (see figure 22.C). In the absence of Ca, the surface is not Si-OH terminated, but Si-H terminated ($\nu(\text{Si-O})$ at 2080 cm^{-1}).⁷⁴ The exchange of K by the protons of water succeeds with a lower energy barrier and therefore no potassium silicates are observed. The same behavior will be observed at the synthesis of ultra-thin layers with low concentrated solutions, the concentration of protons is high, and therefore calcium will be exchanged by the MPER.

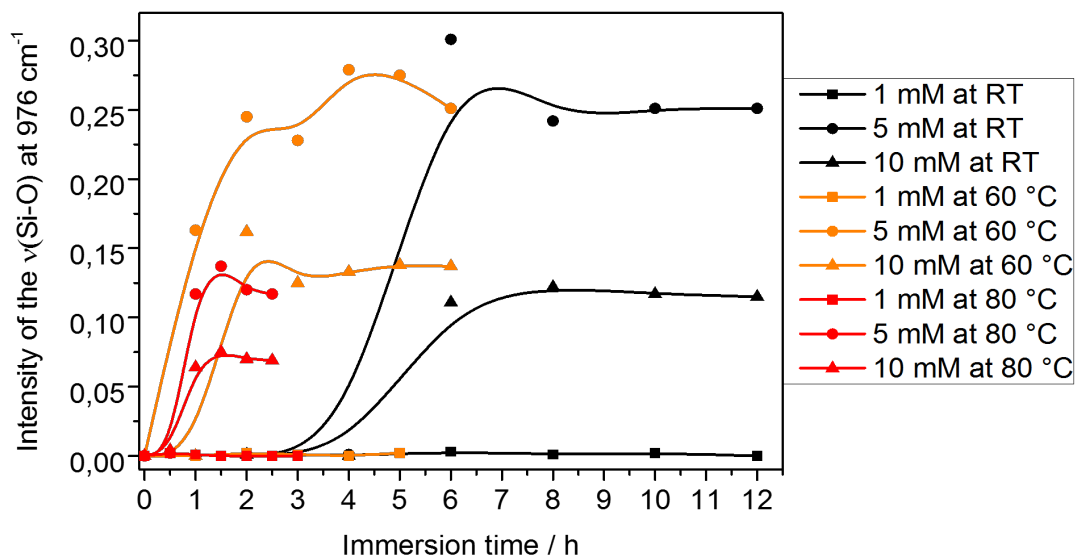


Figure 23: Intensity of the peak at 976 cm^{-1} from the absolute spectra of the synthesis of C-S-H phases on piranha-cleaned wafers during different times of synthesis.

Rate of Synthesis

Different parameters were tested at the formation of the C-S-H phases on silicon wafers, to describe their influence on the characteristics of the samples. The most important parameters controlling the success of the synthesis are: concentration of the implemented solution, temperature and the time of immersion. The formation

of the C-S-H phases can be evidenced by the presence of the O-H vibration modes of dissociated water, however it is in this case more representative to evaluate the Si-O vibration modes, because of their high intensity (see figure 21). In the figure 23 a representation of the intensities of the highest peak as a function of the time of immersion is shown. Three different solutions of Ca(OH)_2 (1 mM; 5 mM and 10 mM) were implemented at three different temperatures (RT, 60 °C and 80 °C). Higher concentrations produced immeasurable thick layers, most of them due to the presence of solid Ca(OH)_2 and CaO , and lower concentrations do not produced any layers. Higher temperatures produce an excessive sedimentation of Ca(OH)_2 , and lower temperatures make the process too slow. The figure 24 shows one interesting fact: for every temperature, independently of the kinetics of the reaction, the solutions of 5 mM produce thicker layers on the wafers. The explanation for this behavior is that the etching of silicon by alkaline solutions successes differently at different pH values.

As was shown by Venkatesh et al. the etching rate has a maximum at certain pH value, which can be in this case near to the pH value of the 5 mM solution.⁷⁵ Other interesting point of the representation is that independently of the concentration of the solution, the synthesis is equally fast, which gives the kinetic idea of a first order reaction.⁷⁶ 1 mM concentrated Ca(OH)_2 solutions were not able to produce C-S-H phases on the silicon wafer. The explanation for this behavior is that the synthesis was always performed in 100 ml reactors. Smaller reactors, or higher pressures may change the observed behavior.

Layer Thickness

The analysis based on the intensity of the most intensive Si-O vibration mode is now supported by another two techniques. ESEM measurements were performed of every sample to determine the layer thickness and uniformity of the layers. As can be seen in the figure 24, the intensities shown in the figure 23 are in agreement with the outcomes of this technique. Even if the layers produced with 5 mM solutions are thicker than the ones produced with 10 mM solutions, they are more irregular. A second technique was used to confirm the results of the layer thickness: in the figure 25 a sample produced with a solution of 5 mM (layer thickness in ESEM of 400 nm) was measured by means of AFM. The sample was measured in order to obtain two parts of the wafer on screen: one part that did not react (isolated by the Teflon sample holder) and a part with the C-S-H layer. Taking the cross section between both sides, the layer thickness can be defined, obtaining approximately the same value as observed in ESEM.

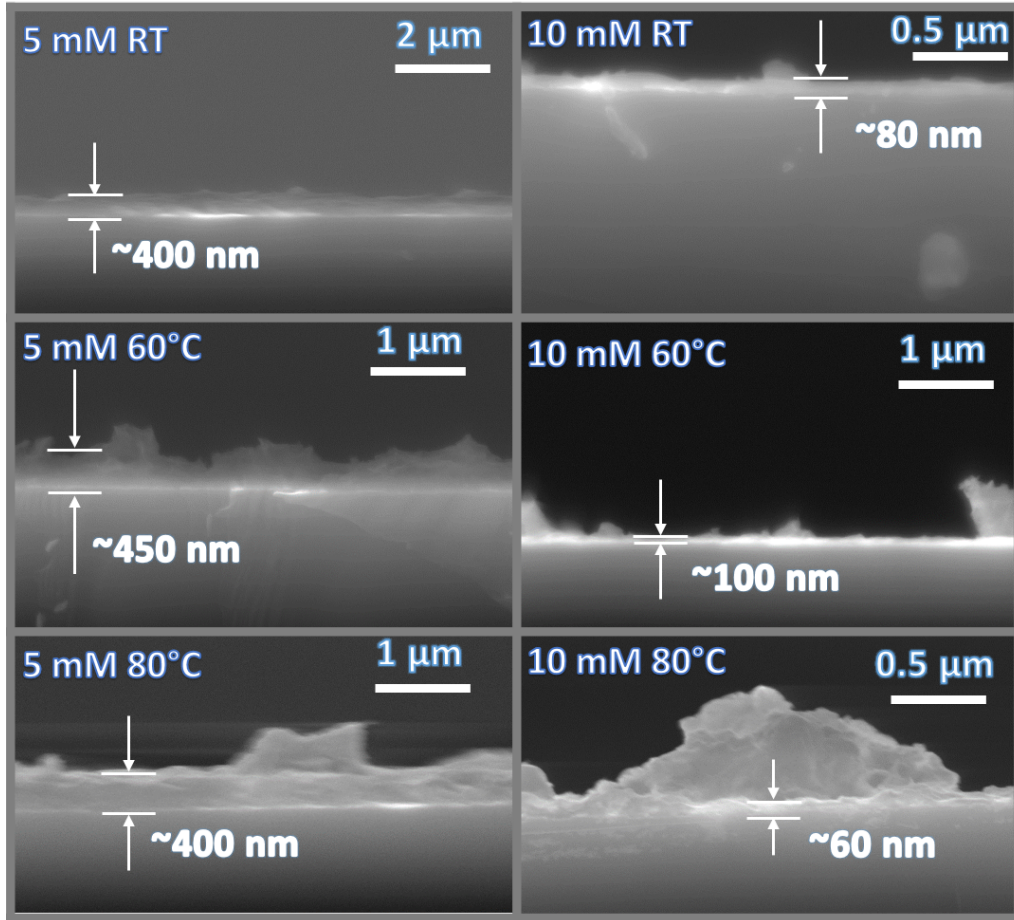
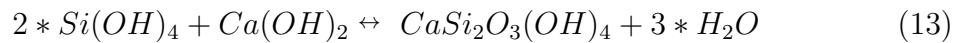


Figure 24: ESEM captions of the C-S-H phases synthesized at different concentrations and temperatures.

4.5 Synthesis of C-S-H Phases and Transformation into C-S Phases



Equation (13) is a representation of the possible stoichiometric configuration of hydrated products, considering the results of the dehydrated ones. The Ca/Si ratio of the crystallized C-S phases is 0.5. The explanation for this value will be later supported by the results of XRD. This value depends on the equilibrium reached between the formation of the C-S-H phases and the MPER in the proposed system. Since this reaction is kinetically controlled, the Ca/Si ratio obtained in all samples is unique for the synthesis in aqueous solutions, independently of the concentration, temperature and time of synthesis, but possible affected by other parameters mentioned such as pressure and size of the reactor.

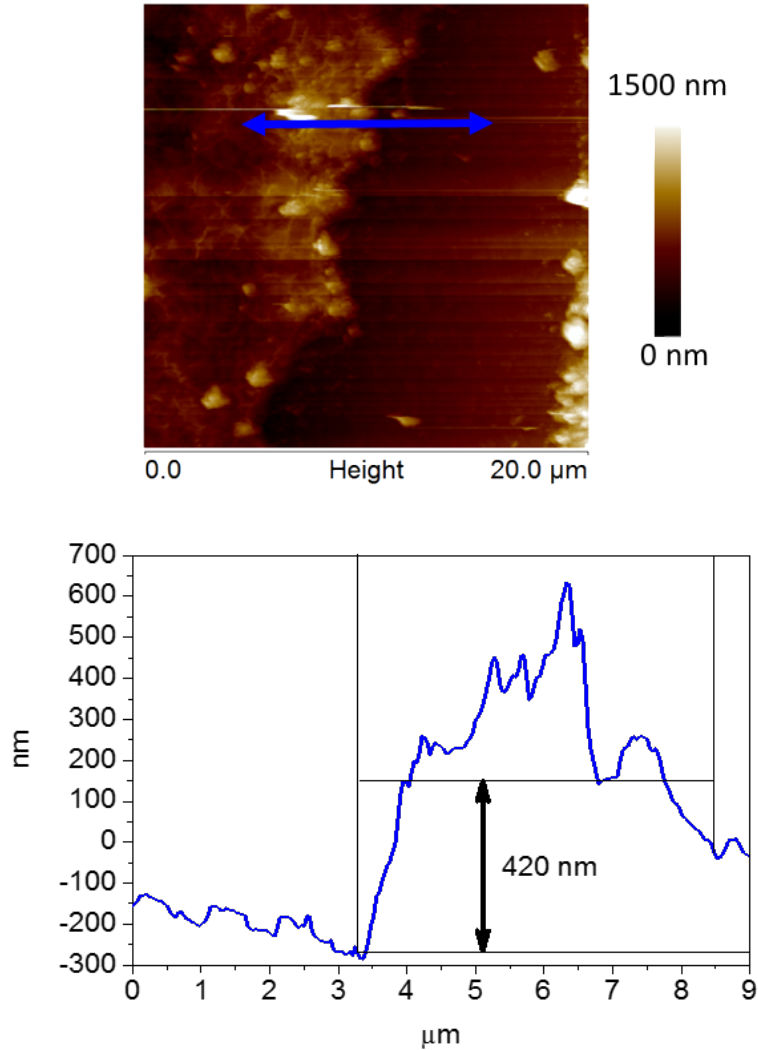


Figure 25: Cross-sectional AFM imaging of C-S-H phases synthesized on a silicon wafer with 10 mM $\text{Ca}(\text{OH})_2$ solutions at RT during 12h.

The synthesis of C-S-H phases on silicon wafers, is followed by the transformation to C-S phases. In figure 27 the difference IR spectra of several steps of heating of a representative sample are shown, which ESEM captions (top and side view) are presented in the figure 26. In figure 27.A the low temperatures are depicted (from 100 °C to 600 °C). The OH-stretching area corresponding to these spectra is shown later in the figure 32.A. From 100 °C to 300 °C, molecular water is desorbed, which produces a shift of the Si-O vibrations to higher wavenumbers ($\nu(\text{Si-O})$ at 1010 cm^{-1} and 971 cm^{-1} shift to 1144 cm^{-1} and 1085 cm^{-1} , respectively). The new ($\nu(\text{O-H})$) vibration modes that are observed are assigned to a different dissociation of water forming the SiO-H ($\nu(\text{O-H})$ at 3740 cm^{-1} in the figure 32.A).⁷⁷ After 300 °C, the dehydroxylation has begun ($\nu(\text{O-H})$ at 3690 cm^{-1} and 3740 cm^{-1} , in the figure 32.A). This removal produces shifts in the vibration modes of Si-O as mentioned above. After 600°C, carbonates were almost completely removed ($\nu_{as}(\text{C-O})$ at 1465 cm^{-1} and $\delta(\text{O-C-O})$ at 875 cm^{-1}), nevertheless the dehydroxylation continues.³⁷ After 700°C the dehydroxylation has already stopped at this point and

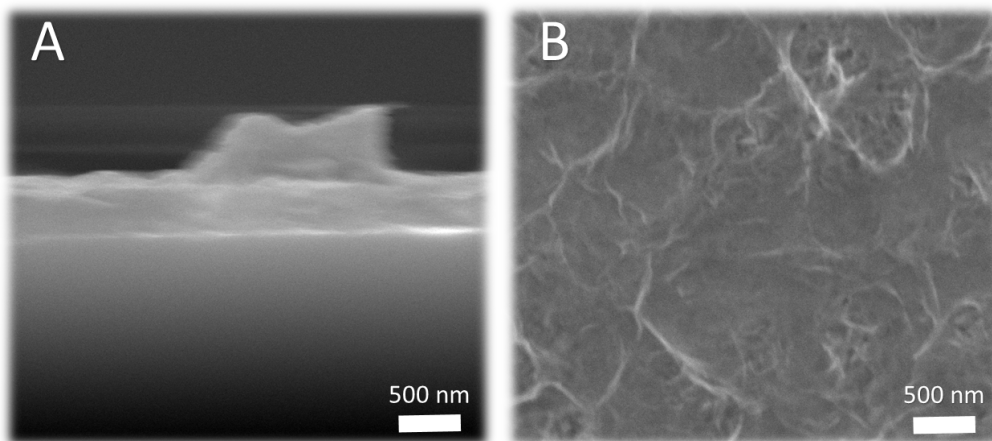


Figure 26: ESEM captions of a representative sample of Calcium-Silicate-Hydrate phases synthesized on a silicon wafer. A. Side view. B. Top view

no foreign compounds remain. From this point forward, the changes in the samples are exclusively on the C-S structure.

In the Figure 27.B the sharp and intensive $\nu(\text{Si-O})$ peak presented at 1160 cm^{-1} represents the formation of the Si-O-Si bonds, which are lower coordinated by calcium, the so-called frustrated chains. This concept is analyzed in detail in a following chapter.⁷² The rest of the Si-O stretching modes are associated to the modifications of the Si-O tetrahedra. Temperatures up to $900\text{ }^\circ\text{C}$ produce the same effect, and the $900\text{ }^\circ\text{C}$ cycle was repeated several times. In the figure 27.B, it is observable that the changes produced are the same but they get weaker every time. The disposition of the $\nu_1(\text{Si-O})$ is combined with the rise of $\nu_2(\text{Si-O})$ and $\nu_4(\text{Si-O})$, which corresponds to the incorporation of calcium into the structure, coordinating the Si-O-Si compounds, building longer chains and increasing the Ca/Si ratio. The vibration modes are supported by first principles calculations (Table 1).

To further understand the difference spectra shown in the figure 27, figure 28 provides absolute information about the remaining structures on the silicon wafer, after several heating steps up to the same temperature ($900\text{ }^\circ\text{C}$). The IR spectrum of a tethering by aggregation and growth (T-BAG) of Wollastonite sample is also shown as a reference in the figure 28.⁷⁸ The three bottom spectra of the figure 28 represent different times of heating of the samples up to $900\text{ }^\circ\text{C}$, that were produced under the same conditions. The disposition of the $\nu_1(\text{Si-O})$ at 1160 cm^{-1} is contrasted with new positive vibration modes, the $\nu_2(\text{Si-O})$ and $\nu_4(\text{Si-O})$ ($\nu_2(\text{Si-O})$ at 1095 cm^{-1} and $\nu_4(\text{Si-O})$ at 1043 cm^{-1}). These vibration modes correspond to the formation of phases with a higher Ca/Si ratio, and $\nu_q(\text{Si-O})$ corresponding to the formation of $\text{SiO}_2(\text{Ca/Si} = 0, \nu_q(\text{Si-O}) \text{ at } 1250\text{ cm}^{-1})$. Bending vibrations support the statement of the Si-O-Si formation, and a higher coordination by calcium, see $\delta_1(\text{Si-O-Si})$. It was also demonstrated by means of first principles calculations that the first Si-O vibrations modes correspond to the stretching of the bridging bonds of the tetrahedral chain. Furthermore, the spectrum of Wollastonite is in agreement with the literature.^{79–80}

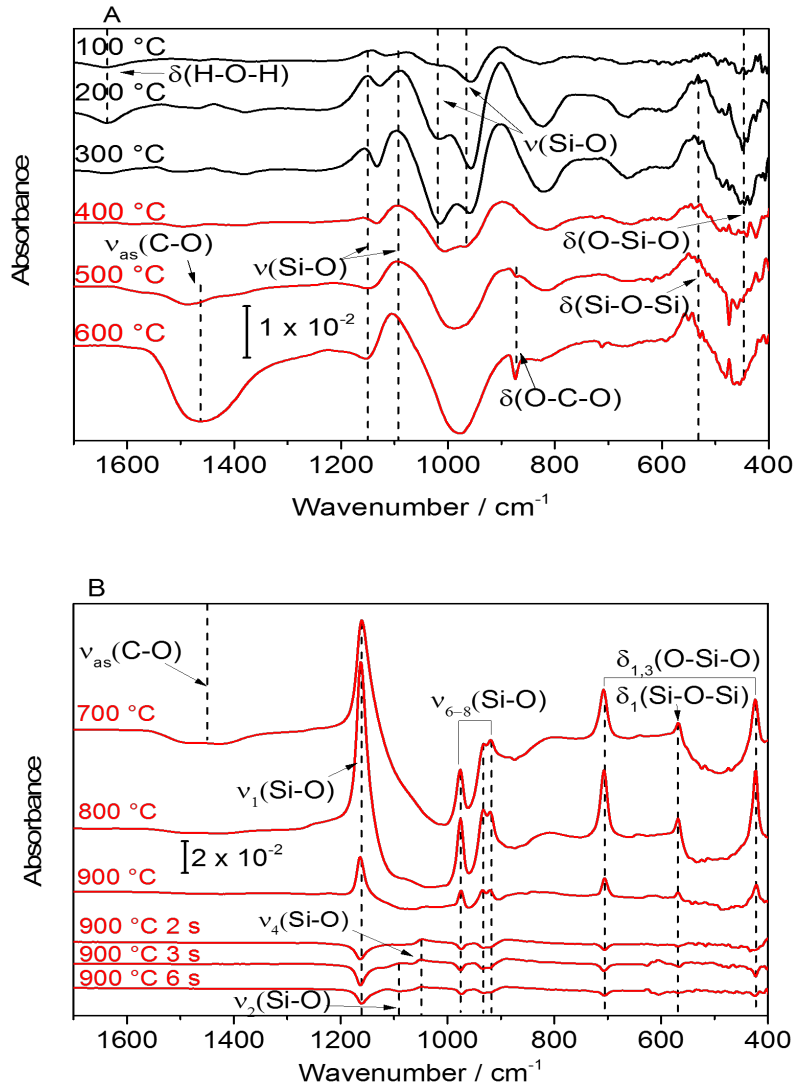


Figure 27: Difference IR spectra of the transformation of C-S-H phases into C-S phases by heating. A. From 100 °C up to 600 °C. B. From 700 °C up to 900 °C. All spectra take the previous temperature as background.

4.6 Thermodynamic Analysis of the Crystallization of C-S Phases

The crystallization of the C-S phases after heating up to 840 °C was already mentioned in a published work.³⁷ A detailed analysis of the XRD measurements of such phases yields in a defined Ca/Si ratio, which confirms the statements made after FTIR results, bringing further information like chain length, and in consequence, associated mechanical properties.³¹ In figure 29, the diffractograms after several periods of heating C-S-H phases synthesized on a silicon wafer are shown. Before heating (black curve) no reflexes are observed. After heating 1 s up to 900 °C (light red curve), 3 reflexes are observed. The coherent scattering domains decrease with the increment of the temperature and time of exposure, as can be observed in the

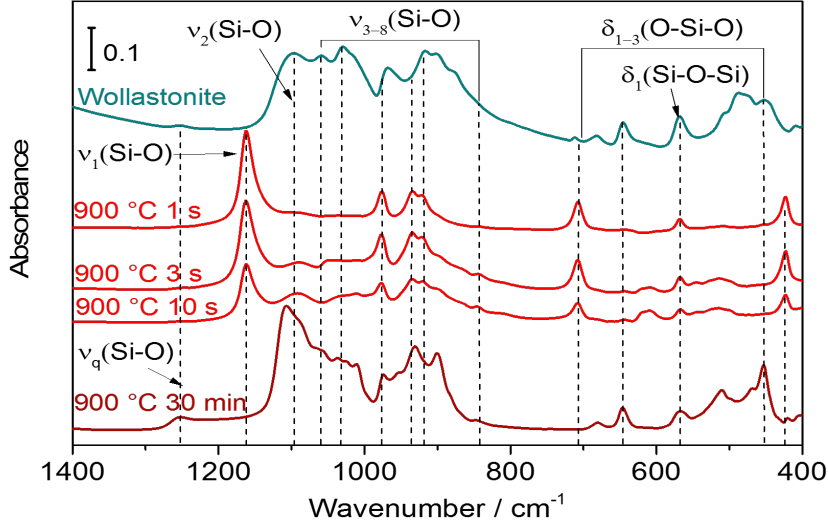
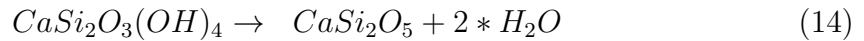
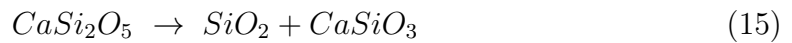


Figure 28: (green line) Absolute IR spectrum of the T-BAG of Wollastonite. (red lines) Absolute IR spectra of several periods of heating of C-S phases synthesized on silicon wafers.

diffraction pattern after 10 s of heating (red curve). Even when the reflexes are few, and their assignment to a singular C-S phase results difficult, it is proposed here that they belong to a unique phase due to the symmetry of occurrence of the peaks. Considering the statement that at the beginning of the heating steps the Ca/Si ratio has to increase from 0 (for the C-S phases before heating), and tend to 1 after heating to the corresponding temperature, the phase with a Ca/Si = 0.5 is proposed, namely titanite-like calcium silicate (CaSi_2O_5).^{73,81} The reflexes are observed at 18.5° , 37° and 56.5° , which correspond to the first, second and third plane of the same orientation of this particular C-S phase, (0 1 1), (0 2 2), and (0 3 3). Since the growth of the crystals is probably oriented in one particular domain due to the oriented wafers, the assignment of the crystalline phase to a specific mineral with high accuracy remains difficult without performing complementary measurements. Nevertheless, the formation of the crystal of titanite is described by the equation (14).



To perform a longer heating process, the samples were put into an oven up to 900°C during 30 minutes in an Argon-protected atmosphere to emulate the conditions under which the short heated samples had in the glovebox. After such prolonged times, no crystals are detected by means of XRD (dark red curve). The reason and mechanism of such change is explained by the equation (15).



The presence of SiO_2 is responsible for the missing crystallization of the CaSiO_3 , since the chains are interrupted by the presence of SiO_2 networks. Every vibra-

tion was analyzed in the basis of first principles calculations and the corresponding vibration modes are depicted in the Table 1.

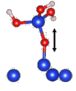
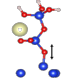


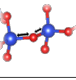
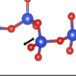
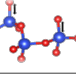
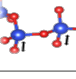
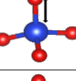
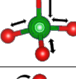
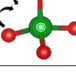
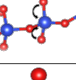
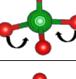
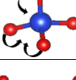
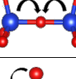
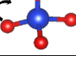
Vibration modes	Experimental Wavenumber (cm ⁻¹)	Associated to DFT Wavenumber (cm ⁻¹)				Vibration Sketch
		C2S	Jaffeite	Wollastonite	Hydroxylapatite	
$\nu_1(\text{Si-O})$, frustrated chain	1160					
$\nu_2(\text{Si-O})$	1095					
$\nu_1(\text{P-O})$	1074				906	
$\nu_3(\text{Si-O})$	1056	821				
$\nu_4(\text{Si-O})$	1043			982		
$\nu_5(\text{Si-O})$	1009			919		
$\nu_6(\text{Si-O})$	979			894		
$\nu_7(\text{Si-O})$	940			842		
$\nu_8(\text{Si-O})$	840	821				
$\nu_2(\text{P-O})$					757	
$\delta_1(\text{O-P-O})$	714				413	
$\delta_1(\text{O-Si-O})$	704	698				
$\delta_2(\text{O-P-O})$	625				371	
$\delta_2(\text{O-Si-O})$	591	535				
$\delta_1(\text{Si-O-Si})$	525		450			
$\delta_3(\text{O-Si-O})$	464	440				

Table 1: Correlation of experimental vibration modes with wavenumbers calculated by means of DFT.

The enthalpies of formation of the phases involved in the equilibrium represented by the equation 15 have been calculated and experimentally determined in the past.^{73,82} Since the mixture of quartz (SiO_2) and Wollastonite (CaSiO_3) is more thermodynamically stable than titanite (CaSi_2O_5), after heating to high temperatures, the reaction depicted in the equation 15 takes place. The equilibrium observed in that equation describes a change of the Ca/Si ratio from 0.5, to 0 and 1. Other authors have observed the same behavior for titanite (0.5), and even for other minerals with different Ca/Si ratios like tobermorite (0.83).⁸²⁻⁸³ This transformation is thermodynamically controlled, since the products are energetically more stable than the reactants, in this case titanite-like calcium silicate.

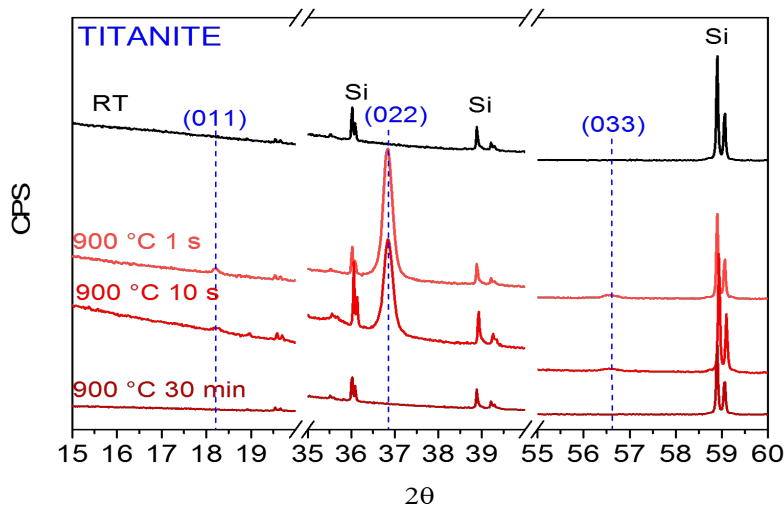


Figure 29: XRD diffractograms after several periods of heating C-S-H phases synthesized on a silicon wafer.

4.7 Dehydroxylation Temperature vs. Ca/Si ratio

At a first glance, it can be concluded from the IR spectrum of the C-S-H phases synthesized on silicon wafers (see figure 21) that no long chains of silicate tetrahedra are formed. Mono and bi tetrahedral compounds are predominant. The reason for this statement is the presence of an only broad peak before heating. This peak splits into two different peaks at higher wavenumbers during the removal of water, as explained and observed in the figure 27. This is also related to the Ca/Si ratio. Hou et al. have shown the dependence of the length of the silicate chain with this ratio. Wollastonite has infinite long chains, and in this mineral the ratio $\text{Ca/Si} = 1$.³¹ Since C-S-H phases synthesized in water solutions do not form long chains before heating, the hypothesis is that, if $\text{Ca/Si} < 1$ the chain length increases with this value.

The hypothesis that the increment of the Ca/Si ratio lengthens the chain leads also to the idea that the temperature of dehydroxylation has to decrease by increasing Ca/Si ratios. To confirm this statement, three different phase diagrams

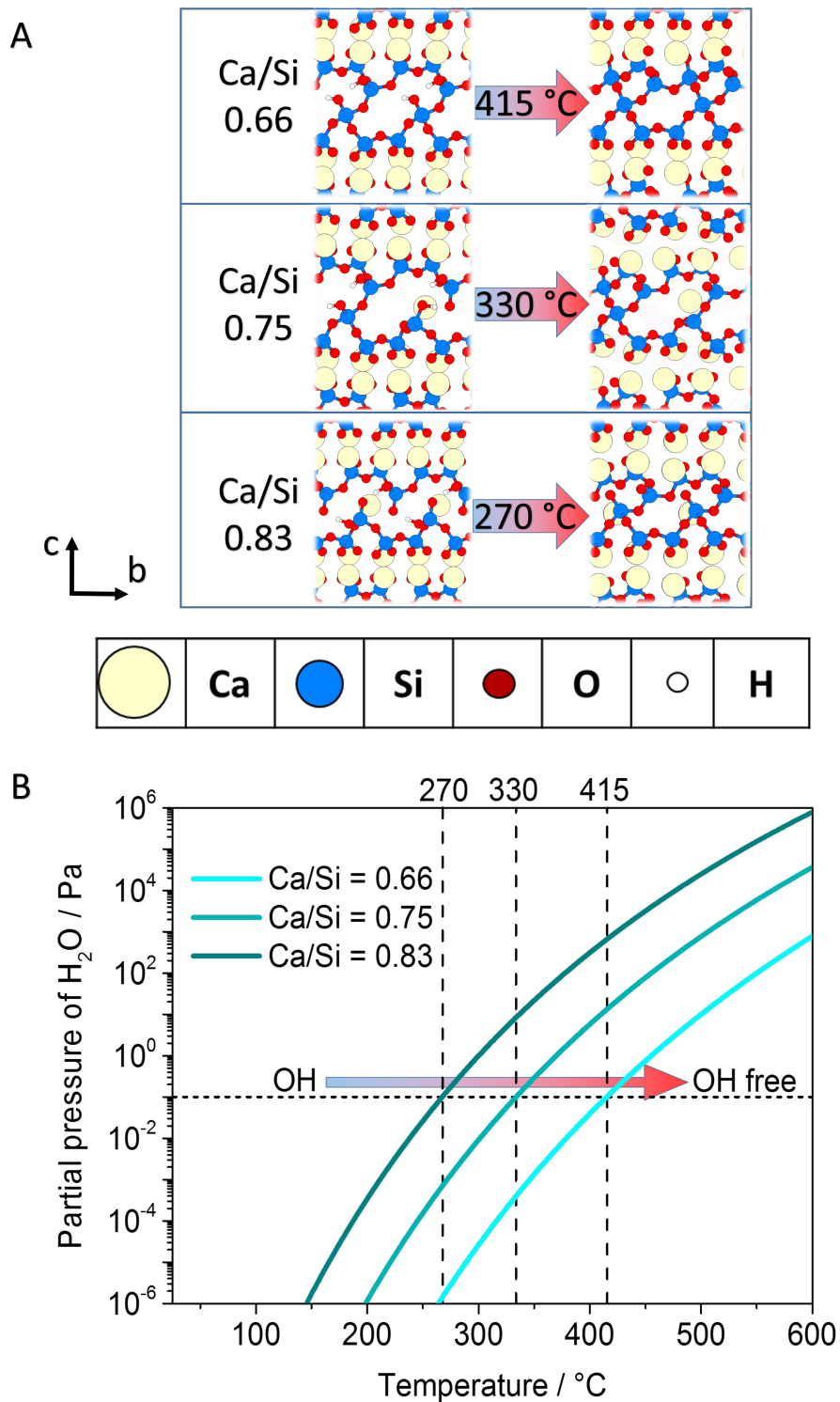


Figure 30: A. Structures of hydroxylated (left) and dehydroxylated (right) tobermorite phases. B. Calculated diagram of phases of the dehydroxylation of three different Ca/Si-ratio phases as a function of pressure and temperature.

are calculated as done by Emmerich et al. and Sanna et al., shown in the figure 30.B.^{10,84}

In contrast to the calculations done in the mentioned works, where water was added and the thermodynamic transitions were studied, in this case the hydroxylated structures found in the literature were relaxed and the volumetric minimum was found by means of the Birch-Murnaghan equation of states. The calculated phases are two different and well-known tobermorites: $\text{Ca/Si} = 0.66$ ($\text{Ca}_4\text{Si}_6\text{O}_{15}(\text{OH})_2$) and $\text{Ca/Si} = 0.83$ ($\text{Ca}_5\text{Si}_6\text{O}_{16}(\text{OH})_2$).^{85–86} To have a trend of the behavior of the temperature of dehydroxylation with the increment of Ca/Si ratio, a supercell with a combination of both phases is also calculated, with a $\text{Ca/Si} = 0.75$ ($\text{Ca}_9\text{Si}_{12}\text{O}_{31}(\text{OH})_4$, figure 30.A). Afterwards, the dehydroxylated structures were calculated. The differences on the grandcanonical potential of these structures before and after the dehydroxylation can be analyzed taking into account their dependence on the chemical potential of the water. Hence, the chemical potentials of water where the transition takes place can be expressed as a curve of pressure and temperature as shown in the figure 30.B. In every phase diagram, the line corresponds to the transition of hydroxylated states to dehydroxylated ones, as shown in the top. It can be observed that, if $\text{Ca/Si} < 1$, the temperature of dehydroxylation decreases with the increment of the Ca/Si ratio. In the figure 30.B, the dash lines represent the temperatures of dehydroxylation in the conditions under which the experiments are performed (in the glovebox about 1 ppm H_2O). For all cases, where $\text{Ca/Si} < 1$, the dehydroxylation involves a tridimensional networking between the tetrahedral chains, which needs much more energy to succeed.

The fact that the temperature of dehydroxylation decreases with the increment of Ca/Si ratio is not only very important for the understanding of the structure of C-S-H phases and their transformation into C-S phases, but also is an excellent experimental parameter to elucidate the Ca/Si ratio of the ultrathin C-S-H phases. This parameter, combined with the correct assignment of vibration modes in the IR spectra, constitutes an unequivocal indicator of such ratio.

4.8 Experimental Modification of the Ca/Si ratio and Confirmation of Theoretical Results

The synthesis of C-S-H phases on silicon wafers was explained above as multiple reactions taking place between the substrates presented here. The equilibrium of the reactions, represented in the equation (13), outstands the unique Ca/Si ratio obtained in water solutions. The MPER controls this equilibrium.³⁰ It was mentioned before that the equilibrium can be also modified implementing different pressures and/or reactor sizes. This strongly influences the layer thickness, which is undesired since the samples are measured in transmission infrared spectroscopy. Therefore, to increase the Ca/Si ratio, methanol in water solutions are implemented at the synthesis. In these solutions, the concentration of H is lower, which induces higher Ca/Si ratios.

In the figure 31.A and 31.B, the absolute spectra of the C-S-H phases are shown, synthesized in different solutions of methanol in water. The concentrations are expressed in % of methanol in v/v. The scale of the spectra is adjusted, since the

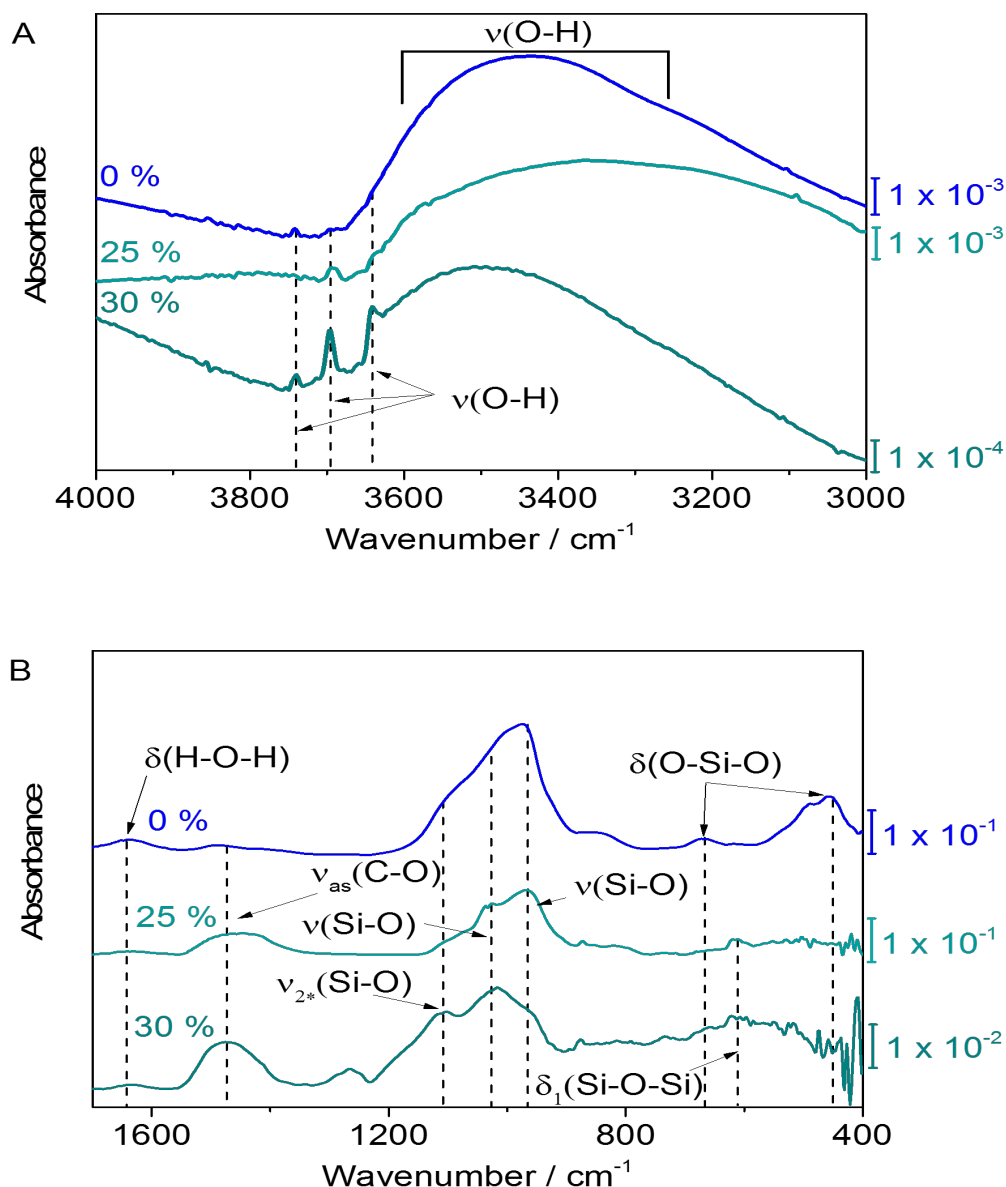


Figure 31: Absolute IR spectrum of C-S-H phases synthesized on silicon wafers with solutions of methanol in water in concentrations of 0, 25 and 30% v/v.

thickness of the C-S-H phases on the wafer strongly decreases with the increment of the concentrations of methanol in the solution. With concentrations higher than 40 % no C-S-H phases could be synthesized, implementing the standard concentrations, times and temperatures. The increment of concentration of methanol in the solution produces an increment of the Ca/Si ratio on the surface. This increment can be noticed in the IR spectra as follows:

- The band corresponding to the Si-O-Si bending vibration modes ($\delta_1(\text{Si-O-Si})$)

at 615 cm^{-1}) indicates the bridging of silicon tetrahedra due to the higher coordination by calcium.

- The first Si-O stretching vibration modes shift to higher wavenumbers ($\nu(\text{Si-O})$ from 970 cm^{-1} to 1013 cm^{-1}).
- The vibration modes corresponding to CaO-H shift to lower wavenumbers ($\nu(\text{O-H})$ from 3690 cm^{-1} to 3640 cm^{-1}).⁸⁷

Samples synthesized with concentrations of 30% methanol show two clearly different vibration modes in the Si-O-stretching area ($\nu_{2*}(\text{Si-O})$ at 1099 cm^{-1} and $\nu(\text{Si-O})$ at 1013 cm^{-1}). $\nu_{2*}(\text{Si-O})$ was already analyzed in the past, and evidences the formation of silicate tetrahedral chains with a higher coordination by Calcium.⁷² In the last section, it was concluded from the theoretical results that the increment of the Ca/Si ratio decreases the temperature of dehydroxylation of the C-S-H phases. If $\text{Ca/Si} < 1$, this dehydroxylation does not involve the formation of longer chains, but a tridimensional networking between them. In the figure 31 it was shown that the synthesis in mixtures of water with methanol produces higher Ca/Si ratios. Therefore, all samples are heated up to produce the dehydroxylation and confirm such behavior. In the figure 32.A, the difference spectra of the heating of the sample produced with in a pure-water solution are observed (which is the OH-stretching area of the figure 27). The dehydroxylation in this case begins at $300\text{ }^\circ\text{C}$, whereat both kinds of OH stretching vibrations modes are being disposed. However, it can be observed that the OH stretching vibration modes associated to the SiO-H keep being disposed at temperatures over $600\text{ }^\circ\text{C}$. In the case of the solutions containing 25 % of methanol, represented in figure 32.B, the dehydroxylation begins at $300\text{ }^\circ\text{C}$ too, but after $400\text{ }^\circ\text{C}$ the dehydroxylation ceases. At last, in the figure 32.C, the dehydroxylation begins and ceases at $300\text{ }^\circ\text{C}$ which confirms the statement that C-S-H phases with higher Ca/Si ratios ($\text{Ca/Si} < 1$) can be dehydroxylated at lower temperatures, since the higher coordination by Calcium impedes the formation of tridimensional networks. A complementary evaluation of figure 32 is shown in the figures 33 and 34.

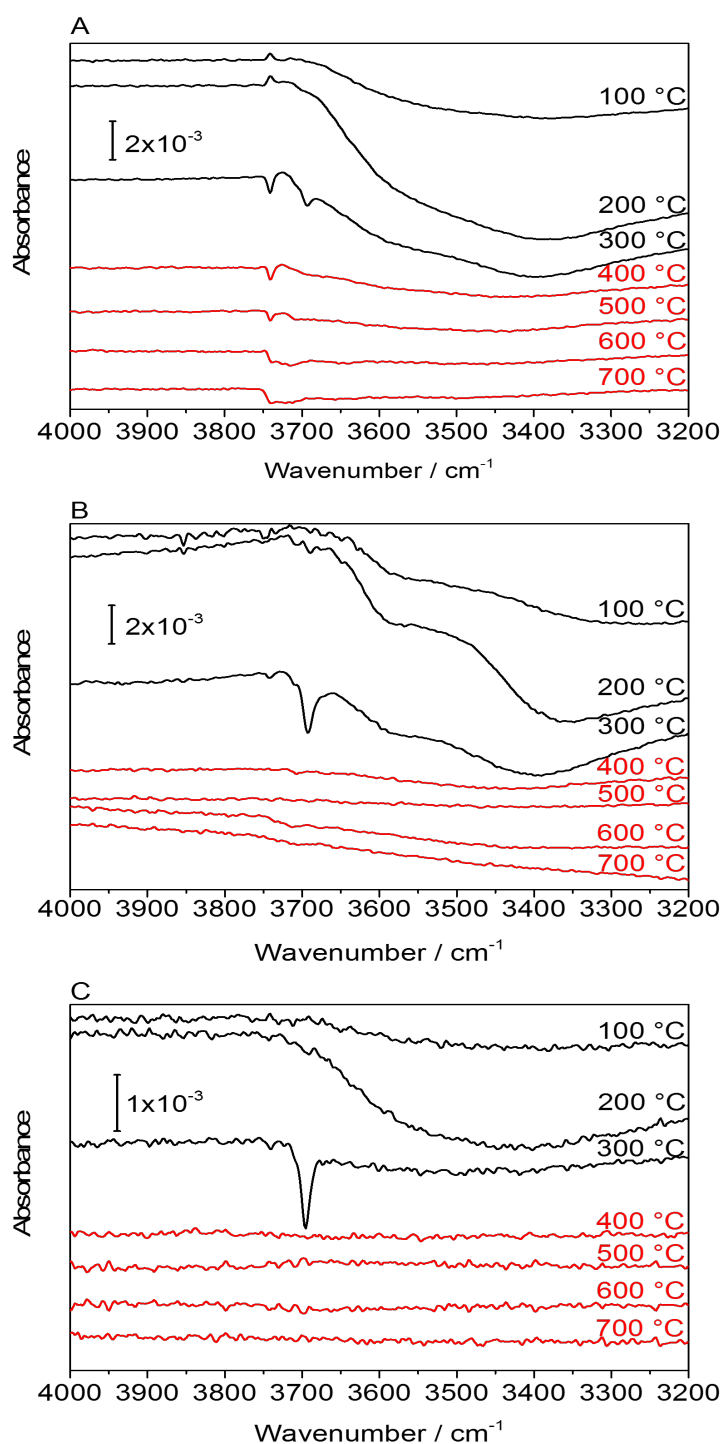


Figure 32: OH-stretching area of the difference IR spectra of several heating steps of A. C-S-H phases produced in a pure-water solution; B. C-S-H phases produced in a 25% methanol in water solution and C. C-S-H phases produced in a 30% methanol in water solution. All spectra take the previous temperature as background.

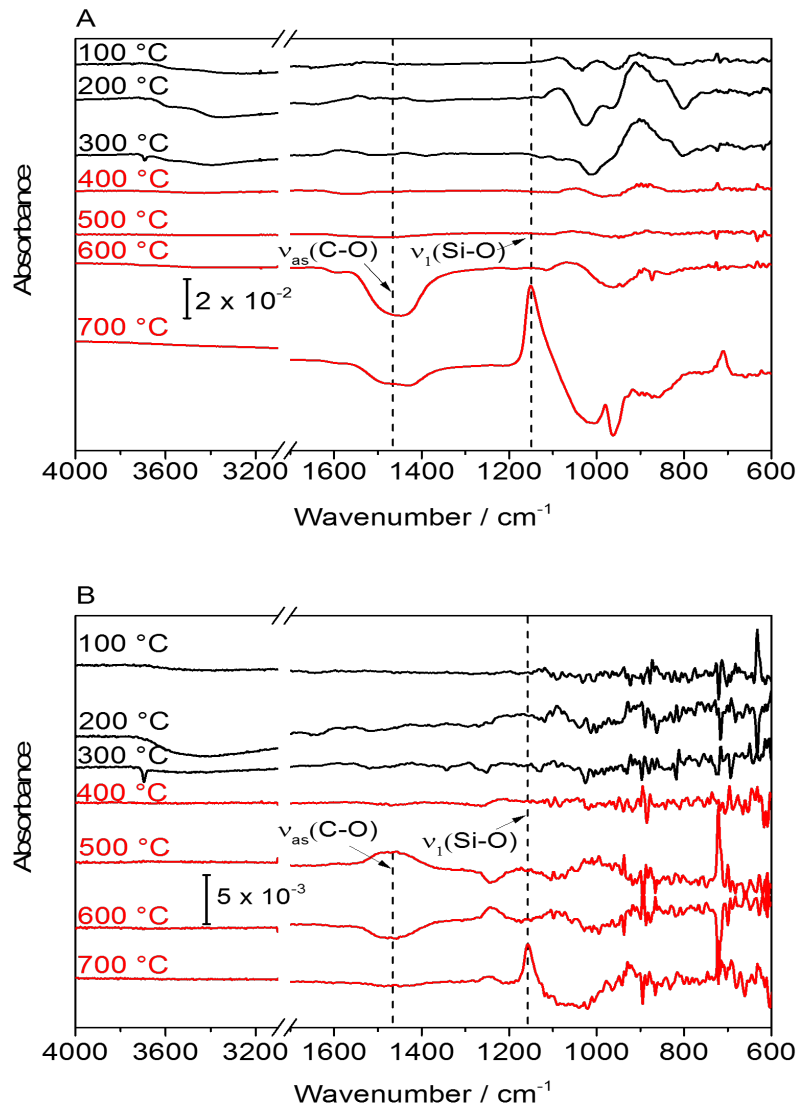


Figure 33: Si-O-stretching area of the difference IR spectra of several heating steps of A. C-S-H phases produced in a 25% methanol in water solution and a B. C-S-H phases produced in a 30% methanol in water solution. All spectra take the previous temperature as background.

In the figure 33 the changes produced in the silicate structure of the samples produced in methanol solutions are shown. In both figures 33.A (25%) and 33.B (30%), the spectra are similar to the ones of figure 27. The principal difference lies on the changes in the Si-O stretching vibration. Since the polymerization was partially produced at RT, the changes in the $\nu(\text{Si-O})$ area are not evident. However, even if it is much less intensive, in both samples the peak associated to the frustrated chains is observed ($\nu_1(\text{Si-O})$), after 700 °C. This confirms that the Ca/Si ratio of the C-S phases is still <1 . However, the increment of the Ca/Si ratio compared to the one of the samples synthesized in water can be also confirmed observing the absolute spectra of both samples as shown in figure 34. After heating prolonged times at 900 °C the C-S phases are transformed into Wollastonite and SiO_2 . In figure 34

the absolute spectrum of the C-S phases synthesized in water after heating several times are shown and compared with the one synthesized in solution of 25% v/v of methanol in water. The changes produced after heating one second the sample synthesized in methanol are more significant than the ones produced on the water sample after 10 seconds of heating at the same temperature. Besides, the amount of SiO₂ produced after heating the 25%-methanol sample is quite less observed by the absence of the corresponding stretching vibration ($\nu_q(\text{Si-O})$ at 1250 cm⁻¹). The implementation of other kind of solvents, for example heavier alcohols remains very promising for the synthesis of C-S-H phases with higher Ca/Si ratios.

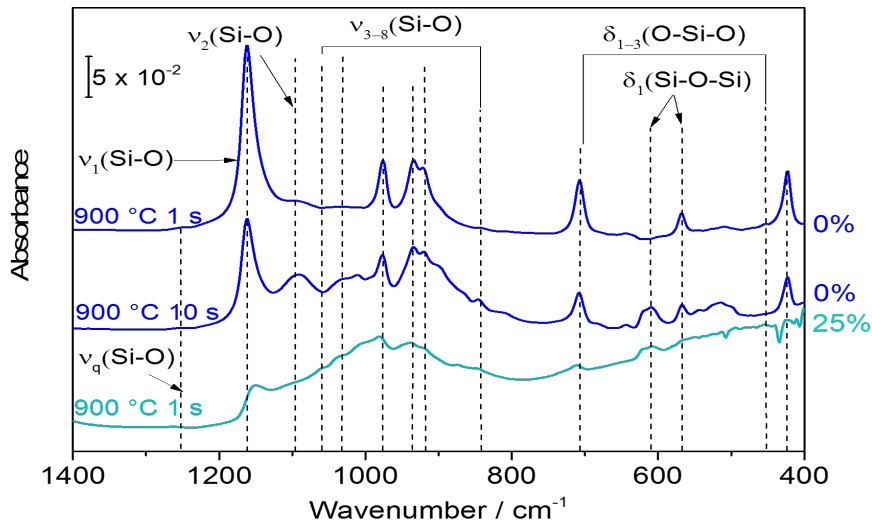


Figure 34: (dark blue lines) Absolute IR spectra of several times of heating of C-S phases synthesized in pure water. (light blue line) Absolute spectrum of C-S phases produced in a 25% methanol in water solution after heating them up.

The synthesis of C-S-H phases and C-S phases on silicon wafers was characterized and the mechanism of their formation was explained. For the first time here, different Ca/Si ratios were assigned to different temperatures of dehydroxylation and their respective vibration modes in infrared spectroscopy. The synthesis has to be further investigated to achieve Ca/Si > 1 as well, and will allow in the future synthesize any specific C-S-H and C-S phase on silicon wafers. This material combination can be studied with many other methods, for example Environmental Scanning Electronic Microscopy (ESEM), Atomic Force Microscopy (AFM), X-ray Photoelectron Spectroscopy (XPS), among others, and by means of first principles calculations.^{36,72}

Apart from their contribution to basic knowledge and understanding, the synthesis of C-S-H and C-S phases on silicon wafers with defined Ca/Si ratios will contribute to the research of several aspects that are of utmost importance nowadays:

- Investigate associated mechanical properties. Since the wafers are able to reflect radiation, mechanical stress applied to them can be analyzed with reflect

tion infrared spectroscopy.³⁷ The stress occasioned to the C-S-H or C-S phases on the wafer can be detected with FTIR and supported with first principles calculations.

- Detect and understand mechanisms of deterioration. The high consumption of concrete is inevitably attached to deterioration costs. One of the most important causes of the corrosion of concrete is due to the weather conditions, where the humidity plays an important role. The mechanism of the effects of water were investigated before, concluding that the chain length is the key for the kinetics of the reactions involved.^{30,72} However, an analysis of the influence of $\text{Ca/Si} < 1$, where chains are already infinite and tridimensional networks are built is missing. Furthermore, the lower coordination of the chains by calcium produced by MPER is observable with FTIR as shown before, which emerges here as a very promising technique to detect deterioration.
- Avoid deterioration. The concrete deterioration can be slowed down in several ways. Since the weather effects on concrete are mostly an interface phenomenon, one popular approach is the reaction of surfaces with different molecules intended to protect them.⁸⁸ It was already shown, that those reaction compete with carbonation of concrete.³⁸ The synthesis of carbonates-free C-S-H phases on silicon wafers and further reaction with specific molecules in protected atmospheres represents an interesting investigation path for this field.

Furthermore, C-S-H and C-S phases on silicon wafers allow the development of several interface applications, based on their unique chemistry.^{2,36,72,89} These substrates might be promising materials as sensors for phosphates in e.g. wastewaters, and for even other compounds that are either needed to be recovered, or has to be urgently removed to avoid serious health problems, like arsenates.^{90–91} The synthesis of important compounds like calcium phosphates can be also achieved, which are significant for the medicine industry due to their bioactivity. The doping of phosphorus in silicon wafers using these substrates seems to be very feasible for the semiconductors manufacture.^{72,89,92–95} The exchange of Calcium with other metals can be also performed (e.g. Nickel), interesting for the catalysis research. Consequently, the successfully development of the applications depends principally on the accuracy and reproducibility of the production of these substrates. The relevant factors to be controlled at the synthesis depend on the final application. For example the wet chemistry, which could make the surface react with specific molecules, is controlled by the MPER.³⁰ The effects produced by this reaction depend strongly on the characteristics of the substrate. These characteristics are: the orientation of the crystal in case of crystalline phases, the layer thickness, and the disposability of calcium at the interface, since the uniformity of the presence of certain metals on the surface plays an important role for several reactions.^{56,96}

4.9 Summary

The core of this chapter lies on the preparation of the model surface, which highlights the importance of C-S and C-S-H surfaces, and makes it possible to model reactiv-

ity, stability and mechanical properties using first principles calculations. Several conclusions could be drawn in this section:

- Having $\text{Ca/Si} < 1$, the heating leads to the formation of $\text{Ca/Si} = 0$ (Quartz) and $\text{Ca/Si} = 1$ (Wollastonite), which are the thermodynamic most stable structures.
- The temperature of dehydroxylation of C-S-H phases decreases with the increment of Ca/Si ratio, and suggests that if $\text{Ca/Si} > 1$, the formation of chains is thermodynamically less probable.
- The unique Ca/Si ratio of the C-S-H phases synthesized in water is kinetically controlled by the Metal-Proton Exchange Reaction, and can be only modified changing the chemistry of the solution, for example with alcohols.
- The observation of the Si-O vibration modes of the frustrated chains in FTIR is directly associated with the lower coordination of calcium and the formation of tridimensional networks.

The controlled synthesis of such crystallized and amorphous compounds is very promising for several applications like sensing, catalysis, semiconductors, medicine between others. In which the interaction of the C-S interfaces with different conditions has to be well understood, principally for wet chemical applications.

5 The Problem of Passivation of C-S-H Phases by Carbonation

The contents of this chapter were adapted from the published article: “Carbonation Competing Functionalization on Calcium-Silicate-Hydrates: Investigation of Four Promising Surface-Activation Techniques” with permission from ACS Sustainable Chemistry & Engineering . Copyright (2016) American Chemical Society.³⁷

5.1 Passivation Approaches to Avoid Corrosion: Concept of Activation

One approach to bridge the problems caused by MPER and carbonation is the passivation of Calcium-Silicate-Hydrate (C-S-H) surfaces. Such passivation can be, for instance, the reaction of C-S-H surfaces with water-repelling films made of specific molecules, like silanes. Molecules like tetraethoxysilane (TEOS) can react with hydrated cement, among others.⁸⁸ However, it is for C-S-H surfaces not clear how they interact with silanes, given that the nature of such bindings is unknown. Besides, C-S-H phases are normally carbonate terminated and they are even more difficult to passivate, since there is already a passivation produced by carbonates that makes the reaction of these surfaces with silanes less probably.⁹⁷ As observed by Okhrimenko et al., on the adsorption of alcohols on the calcium carbonate, the Ca-CO₃ pair tends to delocalize charge by ordering the -OH end of small organic molecules in a way that O associates with Ca and H associates with CO₃, making a covalent bond quite improbable.⁹⁸ In contrast, crystal like silicates are more able to react with several molecules, for example in SiO₄ containing minerals, on which surfaces many molecules could be implemented to react with.⁸⁸ Supplementary calculations were performed in this work, relaxing the concerning molecules on calcite, which are interesting to react with the the C-S-H-phases. The results support the idea that carbonates are not able to react with such passivation molecules, and consequently, should be first removed from the surfaces of C-S-H phases.

Four approaches to activate C-S-H surfaces by removing the carbonates are presented in this chapter: UV-light radiation, direct heating, wet chemical treatment and Ar/O₂ plasma treatment. The evaluation of efficiency of every technique and their effects on the C-S-H phases is mainly done by means of in-situ infrared spectroscopy.

5.2 Methodology

Theoretical Methods

Two calculations were performed to determine the nature of carbonates formed in the system. The aim was reached simulating the carbonation process on Wollastonite surfaces as explained by Longo et al.³² Both calculations carried out in this chapter, were performed within the Generalized Gradient Approximation (GGA), as it is programmed in the Vienna Ab initio Simulation Package (VASP).^{41,61} The electron-ion

interaction was described within the Projector-Augmented Wave (PAW) scheme.⁴² The kinetic energy, up to which the wave functions were expanded, was 360 eV. The Wollastonite slabs were 2×2 supercells with long enough vacuum region to discard interactions within adsorbed molecules and the next structures due to periodicity. In the first calculation clean Wollastonite was relaxed with one molecule of CO_2 . In the second one, a cluster model was performed to model the surface reactant: $\text{Ca}(\text{OH})_2 + 3 \text{H}_2\text{O}$. This assumption is justified because the Ca^{2+} has been removed partially from the surface and is available for the carbonate reaction in the solution, as will be explained in detail later. Atoms were free to relax, until the forces on the atoms were below $10 \text{ meV}/\text{\AA}$. The Brillouin zone integration was done using a $4 \times 4 \times 1$ mesh within the Monkhorst-Pack scheme.⁹⁹ The PBE functional was implemented to describe the electron exchange and correlation energies within the GGA.⁴⁴ The reaction pathway of the carbonation reaction was simulated by means of the Nudged Elastic Band method (NEB).^{100–101}

Complementary calculations were performed to study the reaction of different molecules on a calcite surface. (10.4)-calcite slabs were calculated and water, formic acid, methanol and silicic acid were relaxed on the slabs with the same parameters described above.⁹⁸

Sample Preparation

A $3 \text{ cm} \times 1 \text{ cm}$ silicon(111) crystal was chemically cleaned, exposing it for 30 min at $80 \text{ }^\circ\text{C}$ to a 1:3 solution of aqueous H_2O_2 : 18 M H_2SO_4 (piranha solution), prepared with 97 % p/p sulfuric acid obtained as bought from Merck. Afterwards, the crystal was rinsed thoroughly with deionized (DI) water. The silicon wafers were put into a solution of $\text{Ca}(\text{OH})_2$ with a concentration of 10 mM of a solid with a 96 % obtained from Sigma Aldrich, 100 ml during 6 h at $60 \text{ }^\circ\text{C}$. After that, the samples were left 12 hours in contact with the air to allow the formation of dry carbonates. As shown in the last chapter, this preparation technique yields reproducible ultra-thin C-S-H phases.³⁶

Sample Characterization

Environmental Scanning Electron Microscopy

ESEM micrographs were recorded using a NEON 40 (Carl Zeiss SMT AG, Germany) field emission gun environmental scanning electron microscope (FEG-ESEM), operated using electron energies between 15 kV and 30 kV at a chamber pressure between 0.7 - 1 torr.

Fourier Transform Infrared Spectroscopy (FTIR)

For UV, direct heating and wet chemical treatment, FTIR measurements were performed in a $\text{N}_2^{(g)}$ purged glovebox with a Bruker Vertex 70, and obtained with a nominal 4 cm^{-1} resolution. Spectra were collected from 400 to 4000 cm^{-1} in transmission mode with an angle of incidence of 64° with respect to the silicon surface normal. A room temperature pyroelectric detector (DTGS) was employed for data

collection. In a typical experiment, 1024 scans were taken. The same nomenclature used for the spectra in the last chapter is implemented here as well.

X-ray Diffraction (XRD)

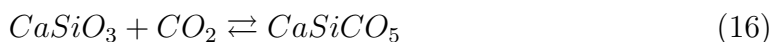
A Bruker D8 Advance in Bragg-Brentano geometry ($\theta - \theta$ setup) for out-of-plane measurements (coplanar geometry) with PSD Lynxeye (192 Si-strip detector), 9-fold sample holder, Cu-radiation was implemented. The scan speed was of 0.2 s/step and the step size of 0.01° . Diffracted intensities were recorded in an interval between 10° and 70° .

Plasma Treatment

The C-S-H surfaces were modified by means of low-reduced plasma pressure. The plasma treatment was performed in a homemade plasma chamber and is combined with in-situ FTIR spectroscopy.¹⁰² Prior to the plasma modification, the chamber was evacuated to a base pressure of about 10^{-4} mbar. A mixture of Ar/O₂ (1/1) was flushed through the chamber. All the plasma treatments were performed at a partial pressure of 0.3 mbar. A commercial high voltage power supply (G2000 Redline) was used for applying an alternating and adjustable voltage with a frequency of 30.7 kHz. The duty cycle was set to 15% and the applied voltage was set to 450 V. The current Intensity measured passing through the electrodes was around 0.2 A. After the plasma modification, the chamber was flushed with N₂ in order to retain the surface changes on the sample. The modified sample was moved to the FTIR position measurement. The FTIR mode used was the discrete polarization modulation Fourier transform infrared reflection-absorption spectroscopy (DPM-FT-IRRAS) with a Bruker Vertex 70 with an MCT-detector (energy range 4000-600 cm^{-1} , aperture 6 mm, energy resolution 4 cm^{-1}).¹⁰² For one single channel spectrum, four cycles (64 scans/spectrum) with p- and s-polarized light were recorded and averaged.

5.3 Nature of Carbonates on C-S Phases: Two Different Species

From the theoretical calculations it can be concluded that two different kinds of carbonates can be formed on the surfaces. In the figure 35, the adsorption of the CO₂ molecule on the (001) Wollastonite surface is observed, forming a calcium-silicate carbonate. Equation 16 shows the first type of carbonation reaction on Wollastonite.



The exposure of CaSiO₃ to CO₂ results in a very fast carbonate production. CO₂ reacts with the oxygen at the surface and forms CO₃²⁻ complexes.¹⁰³ After a carbonate monolayer has been formed, the dry carbonation reaction comes to a standstill. The loss of energy following this barrier-free reaction path is of 0.24 eV, due to the exothermic reaction.³² In the first step of the reaction, the adsorption of

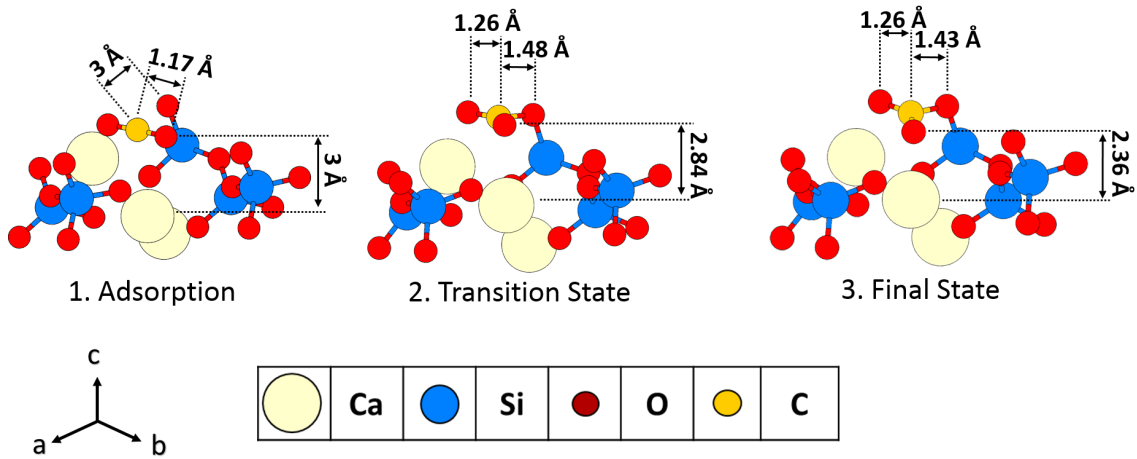
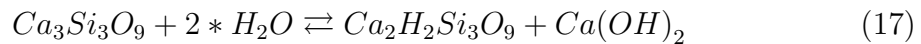


Figure 35: Initial and final configurations of CO₂ reacting with a (001) Wollastonite surface covered by less than a monolayer of water.

the CO₂ molecule, the C-O bond lengths are both of 1.17 Å. The distance between the uppermost Ca of the Wollastonite and the lowermost O of the CO₂ is about 3 Å, and the carbon atom is separated by a distance of 3 Å from the O with which it will react to form the CO₃²⁻ complex. Then, at the transition state, the before-mentioned C-O bonds get longer, to about 1.26 Å, shortening the following two described distances to 2.84 Å and 1.48 Å, respectively. At this point, the third bond is already formed, and the three angles of the four-atom molecule are of 115°. At the final state the lengths of the original C-O-bonds stay constant, meanwhile the third one will be reduced to 1.43 Å, and the Ca-O distance shortens to 2.36 Å.

In the presence of water, MPER leads the surface to a non-stoichiometric thermodynamic ground state in equilibrium with a Ca(OH)₂ solution:



This process is very fast, and the reaction with CO₂ can also take place inside the solution. In that case CaCO₃ sedimentates on the surface.

In the figure 36 a minimum energy path of a cluster model of Ca(OH)₂ in H₂O reacting with CO₂ is represented. CO₂ is dissolved in water to form carbonic acid. Dissociation of carbonic acid leads to the formation of bicarbonate and carbonate ions. Formation of solid calcium carbonates results from the reaction of free Ca²⁺ ions and CO₃⁻² carbonate ions.¹⁰⁴ The reaction is strongly influenced by the chemical potential of water in the environment. The adsorption of CO₂ on CaSiO₃ with a water monolayer completely changes its mechanism. Due to the MPER, the Ca²⁺ has been removed partially from the surface and it is available for the carbonate reaction in the solution. Again, the second type of carbonation is shown in the equation 18.



The thermodynamic ground state of calcium silicate phases in equilibrium with

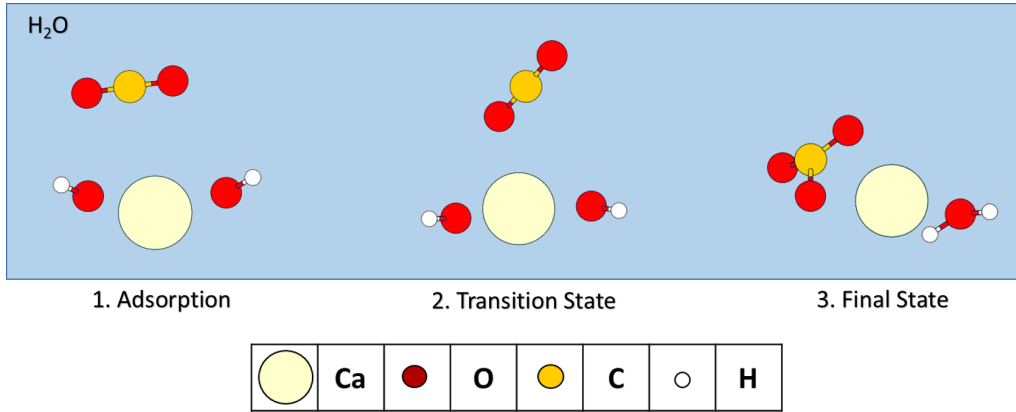


Figure 36: Cluster model of the minimum energy path of CO₂ reacting with Ca(OH)₂.

water is reached fast enough to consider it as a realistic scenario to describe the reaction with CO₂. The energy barrier of that pathway is of 0.32 eV, resulting in a globally considered exothermic reaction with a liberation of 0.96 eV.³²

Many authors have investigated bonds formed between different molecules and silicate or SiO₂ terminated surfaces.^{4,88,105} The aim of these investigations was mainly to produce the passivation of C-S-H phases to avoid their corrosion. In contrast to that, carbonate terminated surfaces are much less investigated.

Earlier investigations about the reaction of carbonates surfaces with different molecules did not include the main groups used for the passivation of C-S-H phases. Therefore, four different molecules were relaxed on a slab of calcite (calcium carbonate, CaCO₃, (10.4)). These calculations simulate the interface between this substrate, which is covering the C-S-H surfaces, and the reacting molecules. The representing schema of the calculations is shown in the figure 37, where the molecules that are relaxed on the calcite slab are: water (H₂O) in 37.A, formic acid (HCOOH) in 37.B, methanol (CH₃OH) in 37.C and silicic acid (Si(OH)₄) in 37.D. Important factors resulting of these calculations are depicted in the figure, where the distance Ca-O is referred to the uppermost Ca of the surface to the O of the functionalizing molecule, and the O-H bridge distance is the one between the H of the functionalizing molecule and the uppermost O of the calcite surface; and Θ is the adsorption energy calculated as done by Sanna et al.¹⁰ No dissociation is observed, and consequently, no molecule reacts forming covalent bonds with the carbonate surface. All energy values are in concordance with the literature.⁹⁸ The conclusion is drawn, that carbonates are not able to react with those molecules aiming passivation, and consequently should be first removed.

5.4 Synthesis of C-S-H Phases on Silicon Wafers

The mechanism of the reactions taking place at the synthesis of C-S-H phases on silicon wafers was explained by Ebbert et al. (see Eq (1) to (5) of that work) and in the last chapter.³⁶ In the figure 38.A, the spectrum of a synthesized C-S-H phase on a silicon wafer is shown. During the synthesis, the CO₂ presence was not avoided, and it can be noticed in the spectrum by the formation of calcium carbonates (ν_{as} (C-O)

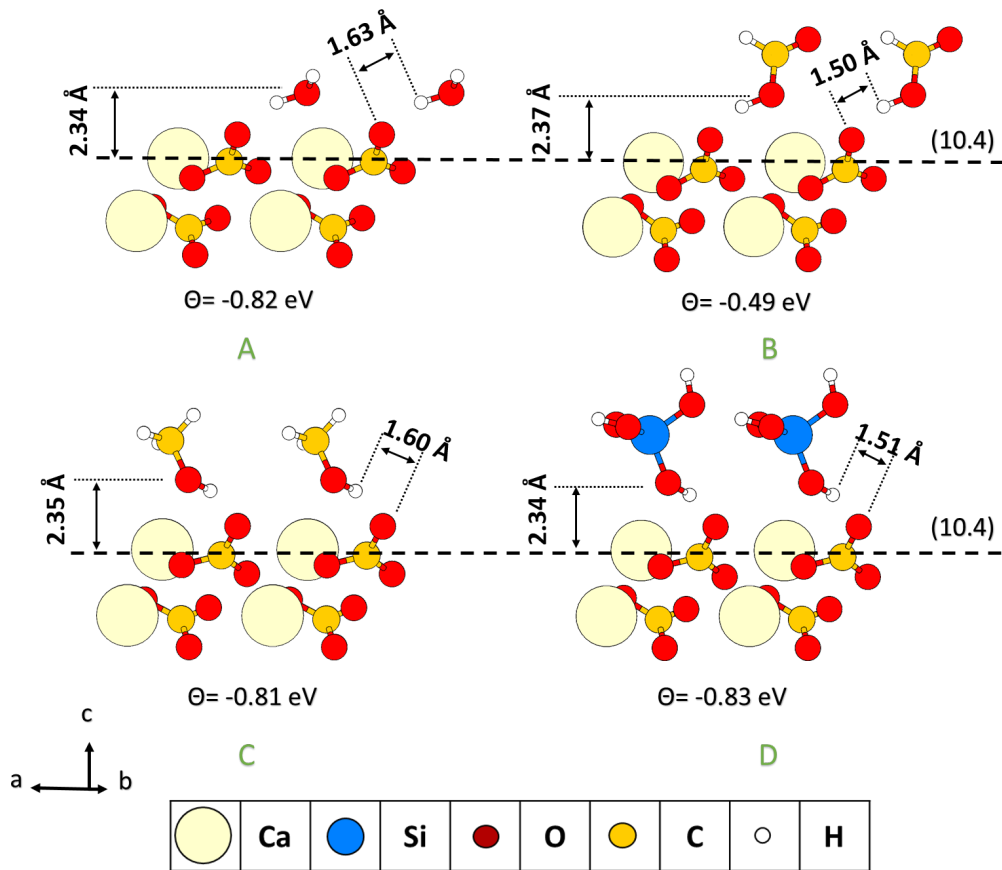


Figure 37: Relaxation of A. Water; B. Formic Acid; C. Methanol and D. Silicic Acid on a (10.4)-calcite slab.

centered at 1460 cm^{-1} and $\delta(\text{O-C-O})$ at 875 cm^{-1}). C-S-H phases on the wafer can be confirmed by the Si-O vibration modes ($\nu(\text{Si-O})$ centered at 1010 cm^{-1} and $\delta(\text{O-Si-O})$ at 475 cm^{-1}), and the vibration modes of OH corresponding to dissociated water ($\nu(\text{O-H})$ at 3749 cm^{-1}). The presence of water can be depicted in the stretching-vibration area as well as in the bending-vibration area (broad peak $\nu(\text{O-H})$ between 3600 cm^{-1} and 3200 cm^{-1} and $\delta(\text{H-O-H})$ at 1640 cm^{-1}). The differences caused by the exposure to the air are hard to recognize in an absolute spectrum. Therefore, in the figure 38.B, the differential spectrum between these two states (before and after exposure to air) is shown. The changes are not drastic, taking into account the intensity, but several interesting peaks appear. Together with the adsorption of water (broad peak $\nu(\text{O-H})$ between 3600 cm^{-1} and 3200 cm^{-1} and $\delta(\text{H-O-H})$ at 1640 cm^{-1}), more carbonates are formed on the surface. As was explained above, CaCO_3 is formed because of the MPER observed by the broad peak centered at 1460 cm^{-1} . A third peak is observed in the spectrum centered at 1593 cm^{-1} , which is attributed here to the asymmetric stretching vibration of calcium-silicate carbonates. This statement will be confirmed by the activation techniques, i.e. gradual removal of carbonates. The adsorption of water and the formation of carbonates produce changes in the silicates, which are observed by the vibration modes in the Si-O region. ($\nu(\text{Si-O})$ at 1124 cm^{-1} ; 1029 cm^{-1} ; 971 cm^{-1} and 945

cm⁻¹).

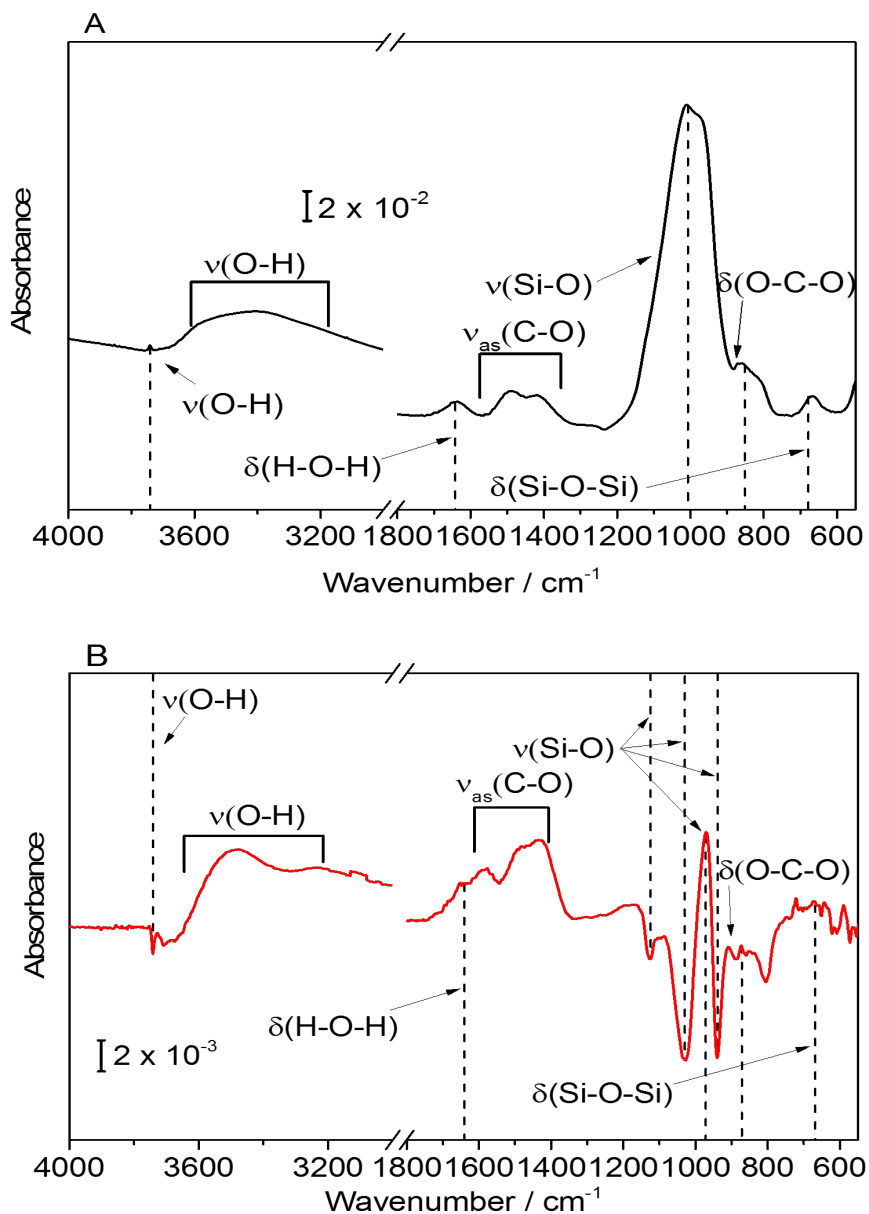


Figure 38: A. Absolute IR spectrum of C-S-H phases synthesized on a silicon wafer. B. Difference spectrum of C-S-H after 12 h exposure to the air, with the sample before the exposure as background.

Figures 39.A and 39.B show ESEM captures from C-S-H phases synthesized on silicon wafers and terminated with carbonates, top and side view, respectively. In the figure 39.A, the layer thickness of the C-S-H phases on the wafer is <200 nm, besides the typical form of carbonates crystals can be detected on the surface.¹⁰⁶ These crystals were not distributed overall the sample, as can be depicted in the figure 39.B and therefore are not detectable using XRD. These captions are useful

to have a good impression of the start point of the substrates before their activation by the four techniques analyzed here.

Next, four different technologies to remove the carbonates from the C-S-H surface are applied. The changes in the IR spectra are considered for the quantification of carbonates removal. Therefore, the region between 1700 and 1300 cm^{-1} is focused in this chapter. In this range carbonates are not the only type of compound that vibrates. Water and organic bending vibrations could influence the integration values. This is later additionally discussed. The correlation between the integration of the absolute spectra before and after every treatment is a valid reference of the effectiveness of the activation, and is taken to compare the efficiency of carbonates removal techniques.

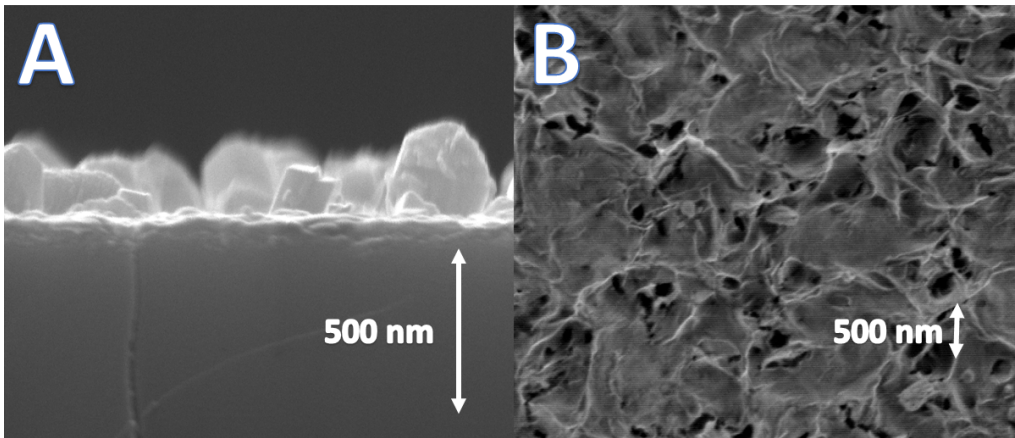


Figure 39: ESEM captures of C-S-H phases synthesized on a silicon wafer, covered with carbonates and before any treatment. A. top view and B. side view.

5.5 Activation Techniques

UV-light Radiation (365 nm)

The samples, already characterized by figures 38 and 39 were radiated with UV-light (365 nm); with a Prizmatix, produced by Mountain Photonics. The power of the LED emitting the beam was of 112 mW. During the radiation, FTIR was measured in situ for 10 hours and figure 40 shows the obtained spectra. All spectra take the initial state of the sample as background. In the range from 1700 cm^{-1} to 1300 cm^{-1} a negative peak appears with a maximum developed at 1593 cm^{-1} . It can be correlated to the asymmetric stretching vibration ($\nu_{as}(\text{C-O})$ at 1593 cm^{-1}) of the CO_3^{2-} group as a part of the calcium-silicate carbonates as described in figure 35.^{33,107–108}. As can be supposed from this figure, calcium-silicate carbonates should present two stretching-vibration modes observable in transmission FTIR, in contrast to the carbonates which just present one. Nevertheless, this vibration mode ($\nu(\text{C-OSi})$) is weak compared to the asymmetric one and hard to distinguish, and therefore are not further considered. From the calculations it is known that after desorption of CO_2 the remaining Si-O has shortened by 0.2 \AA . This shortening is

observed in the experiments as a shift of the Si-O stretching vibration ($\nu(\text{Si-O})$ at 1119 cm^{-1} to 1089 cm^{-1}). Finally, a relaxation of the Si-O-Si ($\delta(\text{Si-O-Si})$ at 600 cm^{-1}) takes place. The disposal of carbonates does not produce an only sharp peak, but broad peaks. Therefore, instead of considering just intensity, the integration of the area of those peaks is taken as proportional to the quantity of carbonates removed. Taking the integral values of the total removal and comparing it to the integration of the carbonates of the original sample a removal-efficiency value can be obtained. For this technique the obtained value is 1.76 %, which depicts the efficiency of the technique.

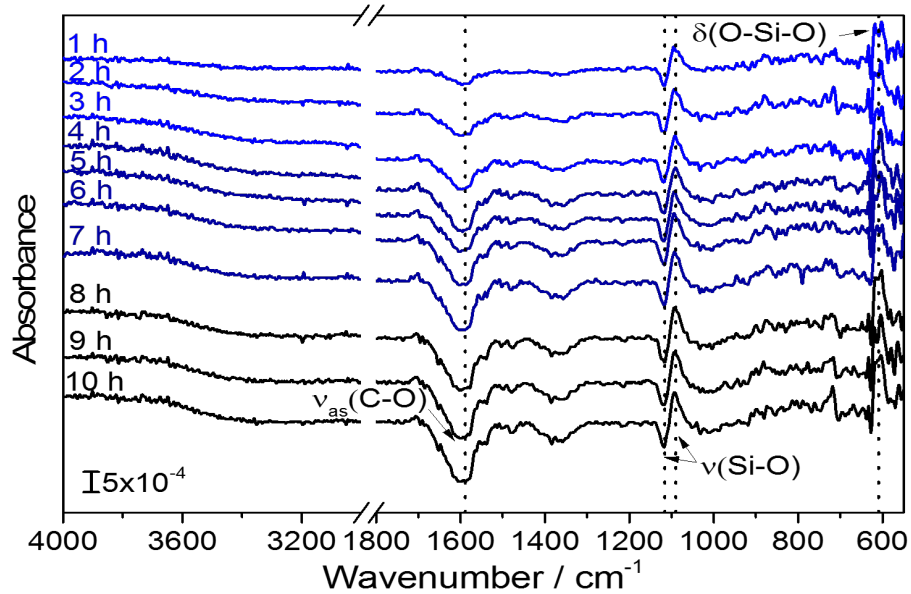


Figure 40: Difference IR spectra of C-S-H phases radiated with UV-light (365 nm). Every spectrum is produced by taking the $t=0 \text{ h}$ as background.

Direct Heating (Room Temperature-840 °C)

C-S-H phases synthesized on a silicon wafer were mounted on the FTIR holder and heated stepwise from $60 \text{ }^\circ\text{C}$ to $840 \text{ }^\circ\text{C}$. FTIR measurements are taken after every heating step at constant $60 \text{ }^\circ\text{C}$. The first measurement is taken as a background for the $100 \text{ }^\circ\text{C}$ measurement. After that, each spectrum is referenced to the previous one to have difference spectra of all temperatures. Figure 41 shows the infrared spectra of each temperature step, from low to high. As can be observed, both kinds of carbonates are removed. The calcium-silicate carbonates were eliminated at lower temperatures, detected by the vibrations mentioned before at UV-light radiation ($\nu_{as}(\text{C-O})$ at 1593 cm^{-1}). A shift is observed to lower wavenumbers with every temperature. This can be explained as was explained before for the CO_3^{2-} -complexes vibrations. During the UV-light radiation, the same intensity (energy) was applied during the whole process, which means that the removed compounds are always of the same kind, releasing CO_2 . In case of direct heating, with every increment of

temperature a different X-CO₃ configuration is removed due to the increment of energy. X is the amount of Ca and Si, and the changes of this configuration shifts the wavenumbers to lower values.¹⁰⁷ The shift to higher frequencies is related to the increment of energy needed to decompose that carbonates. Once a temperature of 400 °C is reached, all the weakest compounds, here called calcium-silicate carbonates are already removed.

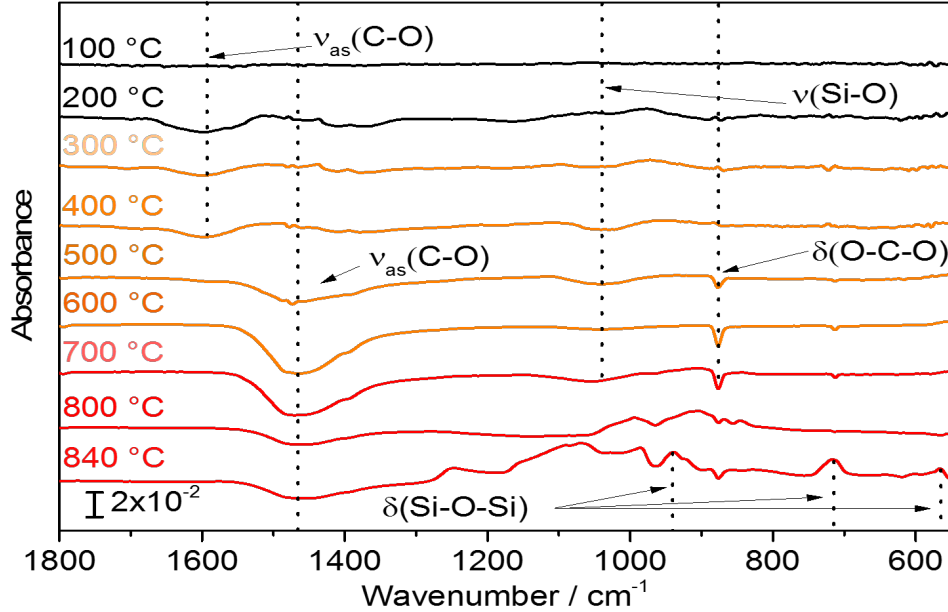


Figure 41: Difference IR spectra of several heating steps of C-S-H phases synthesized on a silicon wafer. IR single channels are taken after every heating step at constant 60 °C and every spectrum takes the previous temperature as background.

Starting from 500 °C the calcium carbonates are removed, observed by the negative peaks corresponding to the asymmetric stretching and to the in-plane bending vibration of CO₃²⁻ ($\nu_{as}(\text{C-O})$ at 1460 cm⁻¹ and $\delta(\text{O-C-O})$ at 875 cm⁻¹).¹⁰⁹ At temperatures higher than 800 °C, the CaO released by elimination of carbonates starts to incorporate to the structure, giving vibration modes that are characteristic of the C-S phases. Two new peaks are observed at 840 °C, which are associated with Si-O-Si bending vibration and reconfiguration of SiO₄ tetrahedra ($\delta(\text{Si-O-Si})$ at 714 cm⁻¹ and 564 cm⁻¹), due to the better definition of the crystal. The same attribution is given to the peak observed at 473 cm⁻¹.¹¹⁰

Performing the integration of carbonates named above, before and after the treatment it could be confirmed that the carbonates were totally (100 %) removed.

Wet Chemical Treatment

The chemical effect of the MPER on C-S-H phases was explained above. If the carbonates of the system are treated chemically, solutions of low pH values must be employed. pH values under 4 are fast enough for the process. Nevertheless this treatment affects the structure of the C-S-H phases too, etching them as described in several publications.^{7,30,32,111} The procedure was carried out to interpret the results. Therefore, an ultra-thin layer of C-S-H phases was exposed to a solution of HCl. The pH of the solution was 3.6. In figure 42 the infrared spectra are represented as a function of time of immersion in the solution, where every spectrum takes the initial state as background, before any treatment. As can be observed, not only the vibration modes corresponding to the removal of carbonates are observed, SiO₂ vibration modes corresponding to a modification in the C-S-H structure ($\nu(\text{Si-O})$ at 1205 cm⁻¹) and Si-O stretching and bending vibration of silicates appear too ($\nu(\text{Si-O})$ at 1030 cm⁻¹ and $\delta(\text{Si-O-Si})$ at 610 cm⁻¹). Asymmetrical stretching vibration of calcium-silicate carbonates ($\nu_{as}(\text{C-O})$ at 1593 cm⁻¹) and calcium carbonates stretching and in-plane bending vibration are detected ($\nu_{as}(\text{C-O})$ at 1460 cm⁻¹ and $\delta(\text{O-C-O})$ at 875 cm⁻¹), confirming the efficiency of their elimination. The integration to determine the efficiency of the removal results to be equivalent to 97 % of the total carbonates. However, with many effects in the silicate structure.

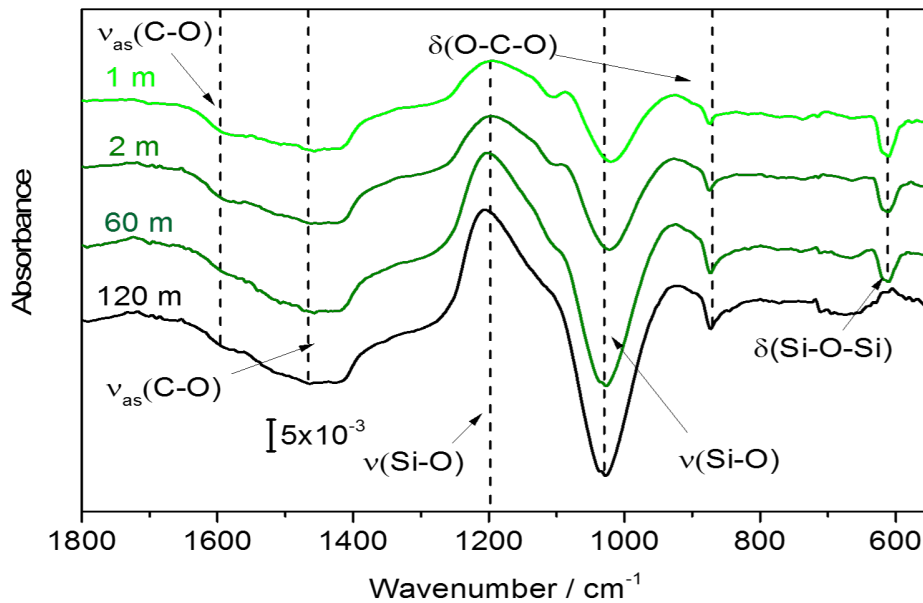


Figure 42: Difference IR spectra of C-S-H phases synthesized on a silicon wafer in contact with a solution of pH 3.6 of HCl in a protected atmosphere to avoid re-carbonation. The background for all spectra is the single channel of the sample before the wet chemical treatment.

Ar/O₂-Plasma Treatment

Figure 43 depicts the difference IR spectra measured of the C-S-H phases after four steps of 1-minute exposure to Ar/O₂ plasma treatment; each spectrum with the previous step as background. In the figure 43.A the p-polarized IR spectra are shown. The signal/noise ratio is relatively low in this case. A better ratio can be obtained if the s-polarized spectra were subtracted from the p-polarized ones to remove the contribution of the atmosphere. But such subtraction cannot be done here, since the substrate vibrates differently at both polarizations, as shown in the figure 43.B. Nevertheless, the changes are strong enough to interpret the results and draw the corresponding conclusions.

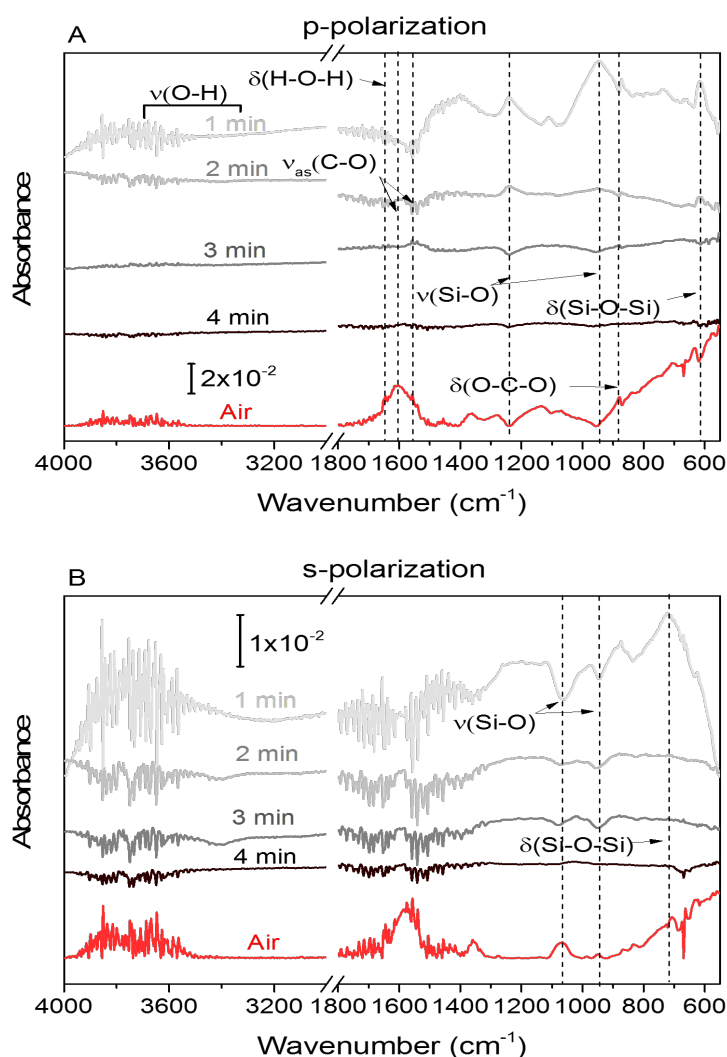


Figure 43: A. p-polarized and B. s-polarized difference IR spectra measured of the C-S-H phases. (gray lines) Four steps of 1-minute exposure to Ar/O₂ plasma treatment; every spectrum takes the previous step as background. (red line) Difference IR spectrum after overnight contact with the atmosphere to produce re-carbonation, with the last step of plasma treatment as background.

The p-polarized IR spectra obtained from the measurements are representative of the removal of carbonates by plasma treatment (see figure 43.A). These measurements serve as milestone for a process of activation that has to be developed. By applying this technique, both kind of carbonates named above were removed. Negative peaks corresponding to Calcium-silicate-carbonates vibrations are observed as well as by direct heating ($\nu_{as}(\text{C-O})$ at 1612 cm^{-1}). Furthermore, the vibration modes corresponding to the asymmetric stretching vibration of CO_3^{2-} and the corresponding to the in-plane-bending vibration appear ($\nu_{as}(\text{C-O})$ at 1562 cm^{-1} and $\delta(\text{O-C-O})$ at 878 cm^{-1}). These peaks mean that the removal of the stronger bonded carbonates was also achieved.¹¹²

The removal success with further formation of SiO_2 , as can be detected by the longitudinal optical phonons of Si-O in the p-polarized IR spectra ($\nu(\text{Si-O})$ at 1241 cm^{-1} and $\delta(\text{Si-O-Si})$ at 617 cm^{-1} in the figure 43.A) and the transversal optical phonons at the s-polarized IR spectra ($\nu(\text{Si-O})$ at 1065 cm^{-1} and $\delta(\text{Si-O-Si})$ at 715 cm^{-1} in the figure 35.B).^{36, 113} In addition to that, a relaxation of the Si-O compounds is observed at both polarizations ($\nu(\text{Si-O})$ at 946 cm^{-1} in the figures 35.A and 35.B). After three cycles, no further modifications were observed. Frequency shifts are expected as a consequence of optical effects arising in the IRRAS spectra, compared to transmission FTIR. These shifts are a result of a significant change in the refractive index occurring when scanning over an absorption band. A shift to higher wavenumbers is detected in the plasma-treatment spectra of carbonates and water bands compared to the corresponding transmission spectrum. The shifts are more pronounced for strong and broad bands than for narrow and sharp peaks.¹⁰² After the confirmation that a further cycle does not modify the sample, the chamber was opened and let overnight in contact with the atmosphere to produce the re-carbonation. In the figures 43.A and 43.B, the red line depicts the spectrum of the sample after this exposure with the last step of plasma treatment as background. As a result, formation of carbonates on the surface together with the adsorption of water is observed, thus with the corresponding effects in the Si-O vibration modes. The removal success of the plasma treatment can be evaluated by the integration of the carbonates vibration modes as done for the previous presented techniques, obtaining a value of 11.57 % of removal.

5.6 Efficiency of the Activation

Carbonates are formed within minutes on C-S and C-S-H surfaces. The formation of carbonates after MPER on C-S-H phases is well known, but the question stays if they could work as passivators for the surfaces. In an earlier study, the D_2O adsorption from humid atmosphere on oxide-covered aluminum films and on self-assembled monolayers (SAMs) of octadecylphosphonic acid (ODPA) was analyzed by means of in-situ photoelastic modulated infrared reflection absorption spectroscopy (PM-IRRAS) to study the barrier properties of SAMs of ODPA and the interface chemistry of the phosphonic acid groups in the presence of high water activities.¹¹⁴ It could be shown that a proton exchange (similar to the MPER) occurs within the AlOOH layer at the interface between the ODPA SAM and the Al metal substrate. The kinetics of this process are similar to those for the uncovered passive-film-coated

Al substrate. These results are a hint, that carbonates do not influence the kinetics of the MPER; yet they influence the maximum of the detectable Ca concentration in the liquid phase.²

For the passivation of the here-analyzed system, the reaction of the surfaces with adequate molecules is the most promising alternative, e.g. with silanes.^{4,105} The barrier to these alternatives is the carbonates termination.⁹⁷ DFT calculations have shown that this kind of molecules do not react covalently with carbonates. The chemical explanation for this behaviour is the constant of dissociation of carboxylic acid, being much bigger than the one of silicic acid.^{115–116} As a result, silicic acid can neither etch carbonates nor bind covalently to the carbonate surface. An alternative for successful chemical passivation is the implementation of stronger acids to react with the surface, for example phosphonic acid.^{117–118}

Independently of the molecule destined to react with the C-S-H phases surfaces, carbonates-free surfaces are desirable for the success of the passivation. Four different techniques were presented here to perform the removal of the carbonates that are acting as a barrier at the surface. UV-light radiation was able to remove 1.76 % of the total carbonates. This result confirms the weakness of the technique, even when the desired superficial effect was achieved. It was already demonstrated by Longo et al., that the formation of calcium-silicate carbonates successes barrier-free releasing 0.24 eV product of the exothermic reaction, meanwhile the calcium carbonates need to overcome a 0.32 eV barrier to be built on the surface, releasing afterwards 0.96 eV.³³ If the endothermic process is considered now, i.e. the decomposition energy of the compounds that are already formed is completely different. In the case of calcium carbonate, the reaction of decomposition is well known, with an activation energy of around 1.86 eV, determined by isoconversional methods.^{119–120} UV-light radiation as implemented in this manuscript delivers an energy of 0.022 mW cm⁻², calculated in base of the distance of 15 cm from the supply to the sample.¹²¹ If this value is used to calculate the energy irradiated from the supply to the sample the total energy value can be estimated. The result is compared to the energy necessary to remove carbonates from the surface. From this comparison it is concluded that the energy necessary to remove all the carbonates of the surface is much bigger than the one provided from the UV-lamp, and therefore most of the carbonates removed are the weakly bonded calcium-silicate carbonates of the uppermost layers. However, with the appropriated lamp, an activation of the surface could be precisely achieved, depending on the kind and amount of carbonates formed on the surface.

The direct-heating technique was the most efficient of all methods, removing the totality of carbonates. The big amount of carbonates removed by this technique is a result of the non-superficial manner of activation. Since the sample is completely heated up, all kind of carbonates are removed, whether they were on the surface or not. The biggest disadvantage of this technique is that the removal of carbonates performs with strong and probably irreversible changes in the silicate structure. However, the removal of the strongest carbonates starts between 400 °C and 500 °C, and the changes in the silicate structure are not drastic at these temperatures. Consequently a longer treatment at low temperatures seems to be promising.

Wet chemical treatment removes virtually the same amount of carbonates as the heating process, but causes strong and undesirable damages in the silicate struc-

ture. Implementing weaker solutions, i. e. higher pH values, and longer times of treatment, the carbonates can be removed more selectively.

At last, plasma treatment resulted to be the most promising of the four applied techniques. The equivalent to 11.57 % of the total of the carbonates could be removed in 3 minutes of contact with the plasma. Even though it was not the strongest technique, the effects in the silicate structure were not dramatic, and further investigations appear necessary to its optimization.

5.7 Summary

Two completely different types of carbonates have been investigated in this study: calcium-silicate carbonates (dry carbonates) and calcium carbonates. Both kind of carbonates are formed within minutes on ultrathin C-S-H phases if the presence of CO₂ is not avoided at the synthesis. Even though some molecules are easily adsorbed on the carbonates surface, there is no evidence for covalent bonds. Carbonates are not able to react with molecules aiming passivation, and consequently should be first removed.

Interestingly, only the calcium-silicate carbonates were sensitive to UV-light radiation as investigated by means of in-situ FTIR spectroscopy. The 1.76 % of the total amount of carbonates was removed.

The direct heating (Room Temperature (RT)- 840 °C) was releasing CO₂ from the calcium-silicate carbonates in the temperature range from RT – 300 °C. At higher temperatures (400 °C – 800 °C) this approach was releasing CO₂ from the calcium carbonates. The total amount (100 %) of carbonates was removed.

On the wet chemical treatment, low pH values are necessary to remove the carbonates. This process was able to remove the 97 % of the total carbonates. However, these solutions affect strongly the C-S-H phases too, given that etching reactions and principally the Metal-Proton Exchange Reaction take place.

The Ar/O₂ plasma treatment of 3 minutes was considerably effective removing the calcium-silicate carbonates as well as part of the carbonates from the C-S-H surface. 11.57 % of total amount of the carbonates was removed with this technique. In addition to the characterization of the efficiency of every technique, it can be concluded that the removal of carbonates could be performed by any of the four techniques implemented here, with the respective adjustments. With an according lamp, UV-light radiation performs a superficial activation. Wet chemical treatment remains applicable, implementing less acidic solutions (pH>4) and prolonged times. By direct heating, low temperatures (<500 °C) remove the superficial carbonates and allow the further passivation. Finally, an adjusted plasma configuration seems to be the most promising technique at RT and complementary investigations appear essential.

6 Implementation of High Temperature Resistant Phosphate-Probe Molecules: Phosphates

The contents of this chapter were adapted from the published article: “Calcium-Silicate Phases Explained by High-Temperature-Resistant Phosphate Probe Molecules” with permission from Langmuir. Copyright (2016) American Chemical Society.⁷²

6.1 Interface Characterization by Probe Molecules

The application of probe molecules to analyze the interface phenomena of C-S-H and C-S phases synthesized on silicon wafers is developed in this chapter. This procedure allows obtaining relevant information about their chemical structure.^{37,122} There are two interesting interfaces to be considered, the first between C-S/C-S-H phases and the atmosphere (gas/C-S) and the second between the C-S/C-S-H phases and the bulk silicon (C-S/Si bulk). The development of probe molecules became very popular in the last decade, principally to be used on fluorescence measurements.^{123–124} Furthermore the implementation of probe molecules on the study of surfaces by means of Fourier transform infrared (FTIR) spectroscopy has been applied in catalysis.¹²⁵

6.2 Selection of Phosphates as Probe Molecules

Several molecules are useful to analyze the interface of the C-S/C-S-H phases, among them many organic compounds. However, the main problem of the application of these compounds as probe molecules is their limited thermal stability. Since most of the organic molecules cannot resist high temperatures, they fall apart before significant changes in the C-S/C-S-H phases can be detected.

Phosphorus compounds forming phosphates were found to be suitable for these studies, since they do not evaporate nor fall apart during the heating steps, but they penetrate the ultrathin C-S phases to reach the silicon wafer.^{45,126} All steps of this migration are analyzed implementing transmission FTIR, and the accumulation of phosphorus in the silicon structure of the wafer is confirmed by Time-of-Flight Secondary Ion Mass Spectrometry (ToF-SIMS).

In this chapter the reaction of the C-S phases with phosphate probe molecules is presented. The aim of this procedure is to further strengthen the interpretation of the FTIR data and to shed some light on the understanding of interfaces between phosphate/silicate systems. It was therefore necessary to design a C-S system of highest reproducibility and applicability, which is the synthesis of C-S phase on the silicon wafer, also described in the last two chapters. A representation of the complete sensing process is shown in the figure 44. The initial substrate consists of ultrathin C-S phases on a silicon wafer (gray, figure 44.A). Figure 44.B represents the step after depositing the probe molecules, phosphates (green) on the C-S phases, where the phosphates of the solution form calcium phosphate at the surface.³⁰ Figure 44.C shows the transport mechanism of the phosphates at 1000 °C which are diffusing deeper inside the C-S phase (yellow), from the gas phase/C-S interface to the

C-S/Si-bulk interface. If the sample is heated continuously, phosphates penetrate into the silicon wafer and the C-S phases are regenerated (figure 44.D).

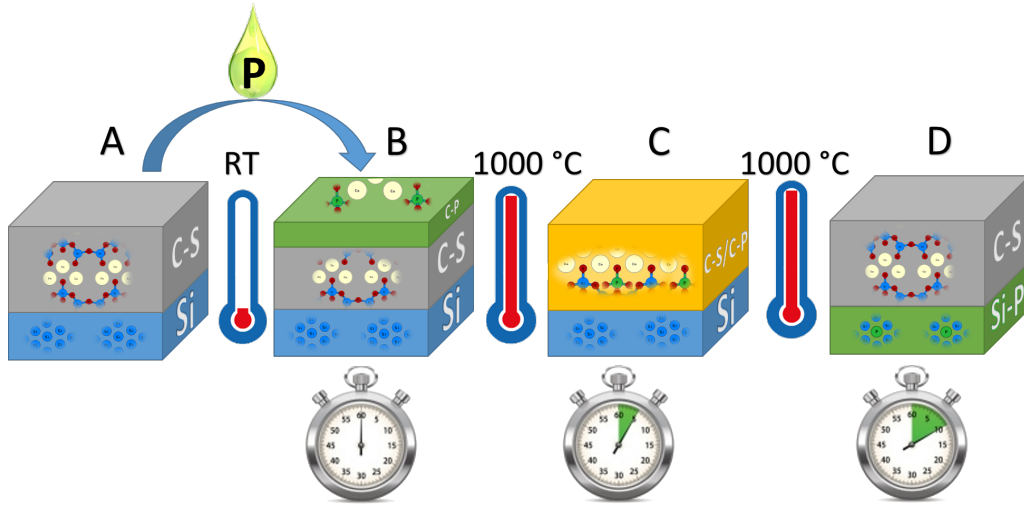


Figure 44: Sketch of the phosphorus diffusion. (A) The initial Calcium-Silicate (C-S) phases (gray) on a silicon wafer (blue). (B) Layer of phosphates (green) deposited on the C-S phases (gray) at room temperature. (C) Phosphates diffuse into the C-S phases (yellow) at 1000 °C. (D) Phosphorus doped into the silicon (green) after several steps of heating at 1000 °C, regenerating the C-S phases (gray).

6.3 Methodology

Computational Methodology

All ab-initio calculations reported here were carried out using Density Functional Theory (DFT) as implemented in the Vienna Ab initio Simulation Package (VASP).⁶¹ The electron-ion interaction is treated within the Projector-Augmented Wave (PAW) method.⁴¹ The plane waves into which the valence electron wave functions are expanded to a kinetic energy cutoff of 360 eV. This energy limit yielded converged structures for all calculations. The Brillouin zone sampling was completed with $1 \times 1 \times 1$ meshes of Monkhorst-Pack k-points.⁴³ The electron-electron exchange and correlation energy was approached making use of the PW91 functional contained in the Generalized Gradient Approximation (GGA).⁴⁴ C-S minerals and phosphates were relaxed and their vibration modes were calculated. The aim of these calculations was to help at the interpretation of the vibration modes of such complex system. In the case of silicates, three different substrates were calculated: C_2S (Ca_2SiO_4) for mono-tetrahedra, Jaffeite ($Ca_6Si_2O_7(OH)_6$) for bi-tetrahedral configuration and Wollastonite ($CaSiO_3$) for an infinite long chain.^{127–129} In the case of phosphates, Hydroxyapatite was used as a model. Since this compound is mono-tetrahedral, the changes on the vibration modes caused by the formation of multi-tetrahedra were supposed to be similar to the ones on the silicate compounds.^{129–130} Each calculation corresponding to a particular mineral was performed from its unit cell. Once the relaxation had converged the vibration modes were calculated.

Synthesis of Calcium-Silicate-Hydrate (C-S-H) Phases

C-S-H phases were synthesized on silicon wafers are described in the last chapter.

Fourier Transform Infrared Spectroscopy (FTIR)

FTIR measurements were done in a $N_2^{(g)}$ purged glovebox with a Bruker Vertex 70, and recorded with a nominal 4 cm^{-1} resolution. Spectra were collected from 400 to 4000 cm^{-1} in transmission mode with an angle of incidence of 64° with respect to the silicon surface normal. A room temperature pyroelectric detector (DTGS) was employed for data collection. In all experiments 1024 scans were measured. To perform the deposition of the desired probe molecule on the gas/C-S-H and gas/C-S interface, an aliquot of $4\ \mu\text{L}$ 1 mM KH_2PO_4 aqueous solution was implemented. During the heating process, all measurements, before and after heating, were performed at $60\text{ }^\circ\text{C}$. After a successful implementation of the phosphates as a layer on the surface, heating is applied, thereby driving the probe molecules inside the structure. The silicon wafer is mounted on an FTIR holder designed to measure and heat up to $1000\text{ }^\circ\text{C}$ (heating rate $\simeq 50\text{ }^\circ\text{C/s}$) in-situ. The same nomenclature as described in the chapter 4 is implemented for all the spectra presented in this chapter.

Time-of-Flight Secondary Ion Mass Spectrometry (ToF-SIMS)

The ToF-SIMS analysis was carried out on a gridless reflectron-based ToF-SIMS V (ION-TOF GmbH, Muenster, Germany), equipped with a bismuth-cluster ion source. All spectra and images were obtained using Bi^+ primary ions at 25 keV energy in the high current bunched mode, with a mass resolution of $m/\Delta m = 6000$. Depth profiling was performed by eroding the samples with a 1 keV Cs ion beam.

6.4 C-S-H Phases Characterization and Transformation into C-S Phases

A detailed description of the ultrathin C-S-H phases on silicon and their transformation to C-S phases as a function of temperature is given in the figures 45 and 46. As can be observed, there is a huge similarity with the figures 21 and 27 of the chapter 4, but the difference lies on the presence of carbonates, which in this chapter was not avoided. In figure 45 an IR spectrum of the synthesized C-S-H phases on a silicon wafer referenced to the piranha-cleaned wafer is depicted. As it can be seen the synthesis not only drives Ca to the surface, but also carbonates that are identified by their vibration modes (in $\nu_{as}(\text{C-O})$ with a maximum at 1491 cm^{-1} and $\delta(\text{O-C-O})$ at 878 cm^{-1}).^{37,131–133} The spectrum shows two features related to the presence of OH: a broad band between 3100 and 3500 cm^{-1} corresponding to molecular water adsorbed and a sharp peak at 3690 cm^{-1} that confirms the presence of dissociated water as Ca-OH.¹³⁴ Other vibration modes are observed after the synthesis, corresponding to the Si-O ($\nu_{mono}(\text{Si-O})$ with a maximum at 970 cm^{-1} and $\delta_{mono}(\text{O-Si-O})$ with a maximum at 460 cm^{-1} , which evidences the formation of the C-S-H phases.

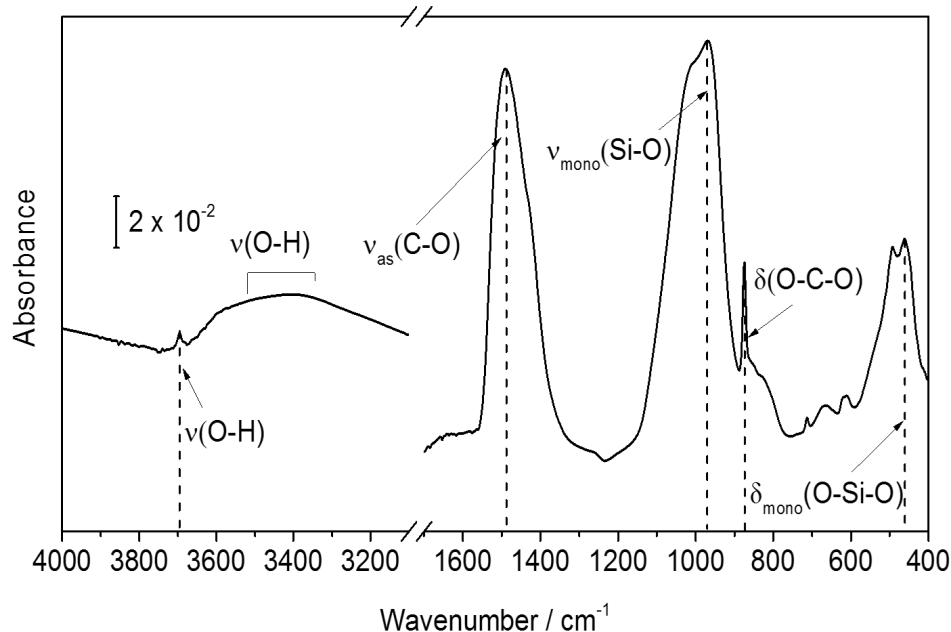


Figure 45: Absolute IR spectrum of C-S-H phases synthesized on a silicon wafer.

An important observation of figure 45 is that no Si-O stretching nor Si-O-Si bending vibrations corresponding to multi-tetrahedral compounds are observed. This is attributed here to the absence of chains, i.e. all the Si-O bonds of the tetrahedra present similar vibration modes, and the explanation for that is that no long chains are formed.

In the first heating step up to 900 °C several changes are observed (see figure 46.A). The removal of carbonates is underlined by the negative band corresponding to the stretching modes at 1491 cm⁻¹ and the peak corresponding to the bending modes at 878 cm⁻¹. Together with the elimination of carbonates the OH species are being removed as well, denoted by the negative vibration modes cited for such compound before (broad band between 3100 and 3500 cm⁻¹ corresponding to $\nu(\text{O-H})$ of free water and a sharp peak at 3690 cm⁻¹ corresponding to dissociated water). The temperature produces changes in the structure of the silicates. Vibration modes evidence these changes on silicates ($\nu_{1;3-5;7-8}(\text{Si-O})$ at 1160 cm⁻¹, 1056 cm⁻¹, 1043 cm⁻¹, 1009 cm⁻¹, 940 cm⁻¹ and 840 cm⁻¹). These vibrations modes remain active in the cycles of heating, as observed in the figure 46.B. Every vibration mode is correlated to a calculated vibration mode, which are shown in Table 1, in the chapter 4. The vibration modes of specific compounds are correlated to the ones observed in the spectra of the present system, which accelerates the interpretation of the changes occasioned in the structure. Even if the total wavenumbers do not exactly agree with the experimental ones, the order does.

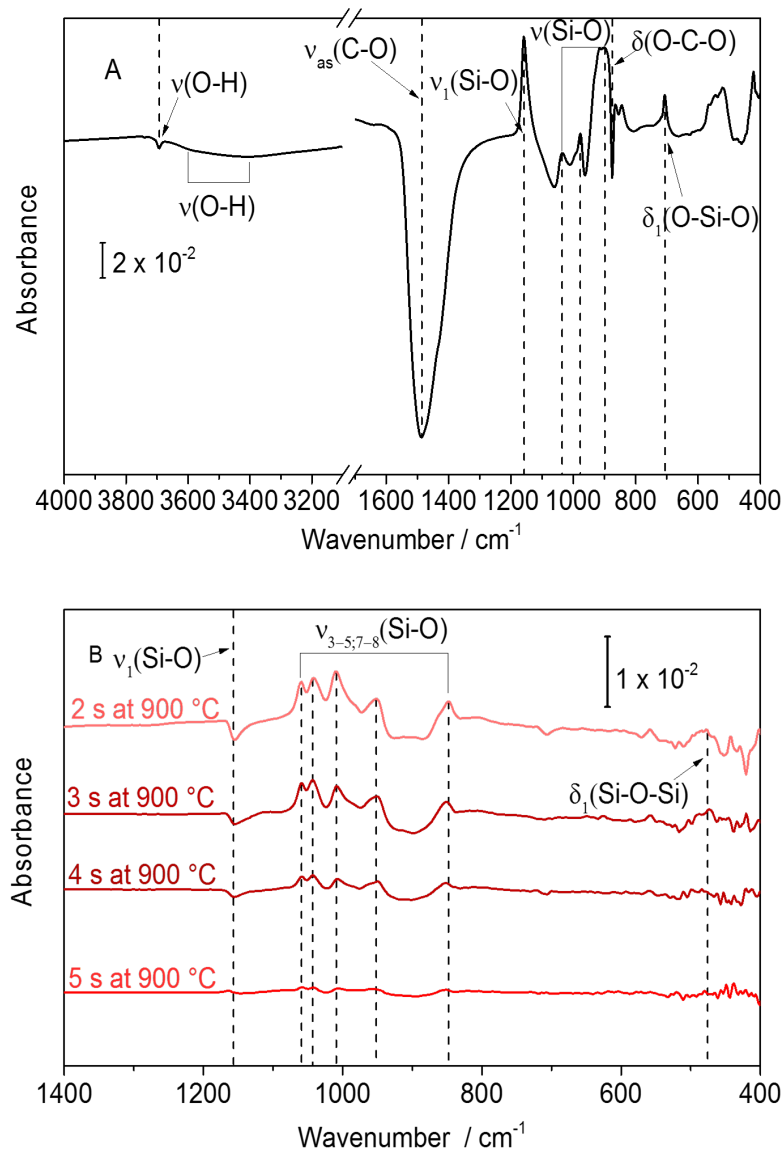


Figure 46: Difference IR spectra of the transformation of C-S-H phases into C-S phases as a function of temperature. A. Difference IR spectrum of the first heating step of the C-S-H phases up to 900 °C during 1 s with the C-S-H phases on a silicon wafer as background. B. Difference IR spectra of further heating steps of C-S phases, each spectrum takes the last step of heating as background.

The most important fact of the transformation is that several new vibrations appear, associated with the formation of chains. Besides, the loss of OH groups is associated with the formation of CaO and the decomposition of Si-OH, named dehydroxylation.^{135–136} The remaining compounds react to build Ca_xSi_yO_z-chained structures. The sample was stepwise heated until a constant line was found in the difference spectra as a function of temperature, which means that further heating up to the same temperature does not change the surface chemistry, which is an

adequate starting point for the probe molecules (figure 44.A).

6.5 Application of Probe Molecules on C-S-H Phases

First, probe molecules were deposited on C-S-H phases before any heating treatment, and the corresponding spectrum is shown in the figure 47. The OH stretching vibration of the dissociated water ($\nu(\text{O-H})$ at 3740 cm^{-1}), is associated with the presence of molecular water. These water molecules are observable by the corresponding stretching and bending vibration ($\nu(\text{O-H})$ between 3600 cm^{-1} and 3400 cm^{-1} and $\delta(\text{H-O-H})$ at 1620 cm^{-1}). The interaction of the phosphates on the sample affects not only the silicates but also the carbonates. This is confirmed by the negative stretching and bending vibrations of the carbonates ($\nu_{as}(\text{C-O})$ centered at 1420 cm^{-1} and $\delta(\text{O-C-O})$ at 870 cm^{-1}) and Si-O vibration modes ($\nu_{mono}(\text{Si-O})$ at 933 cm^{-1} and $\delta_{mono}(\text{O-Si-O})$ at 570 cm^{-1} and 475 cm^{-1}) and the positive stretching vibrations of phosphates ($\nu(\text{P-OH})$ at 1118 cm^{-1} and $\nu(\text{P-O})$ at 1005 cm^{-1}).¹³⁷

As it was observed before in the figure 45, at the synthesis of the C-S-H phases on a silicon wafer, the Si-O stretching vibration is represented by a broad peak with a maximum at 970 cm^{-1} . This wavenumber is influenced by the presence of water and carbonates on the sample, but remains as a single vibration mode. After the application of the probe molecules, only one vibration mode is being affected by the formation of phosphates ($\nu(\text{Si-O})$ at 930 cm^{-1}). This confirms the first conclusion, that no long chains are formed before the heating of the C-S-H phases. The presence of chains is associated to the interconnection of Si-O tetrahedral, as observed in several vibration modes in figure 46.

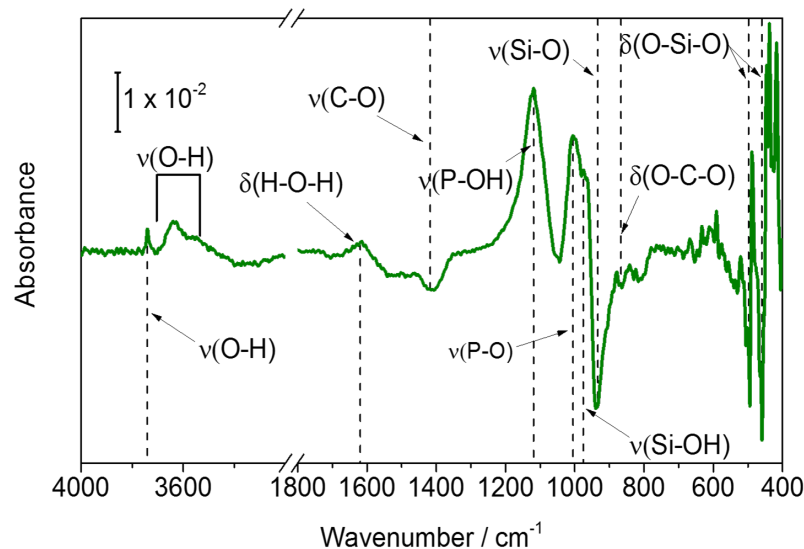


Figure 47: Difference IR spectrum of the phosphates molecules deposited on C-S-H phases, with the C-S-H phases synthesized on a silicon wafer as background.

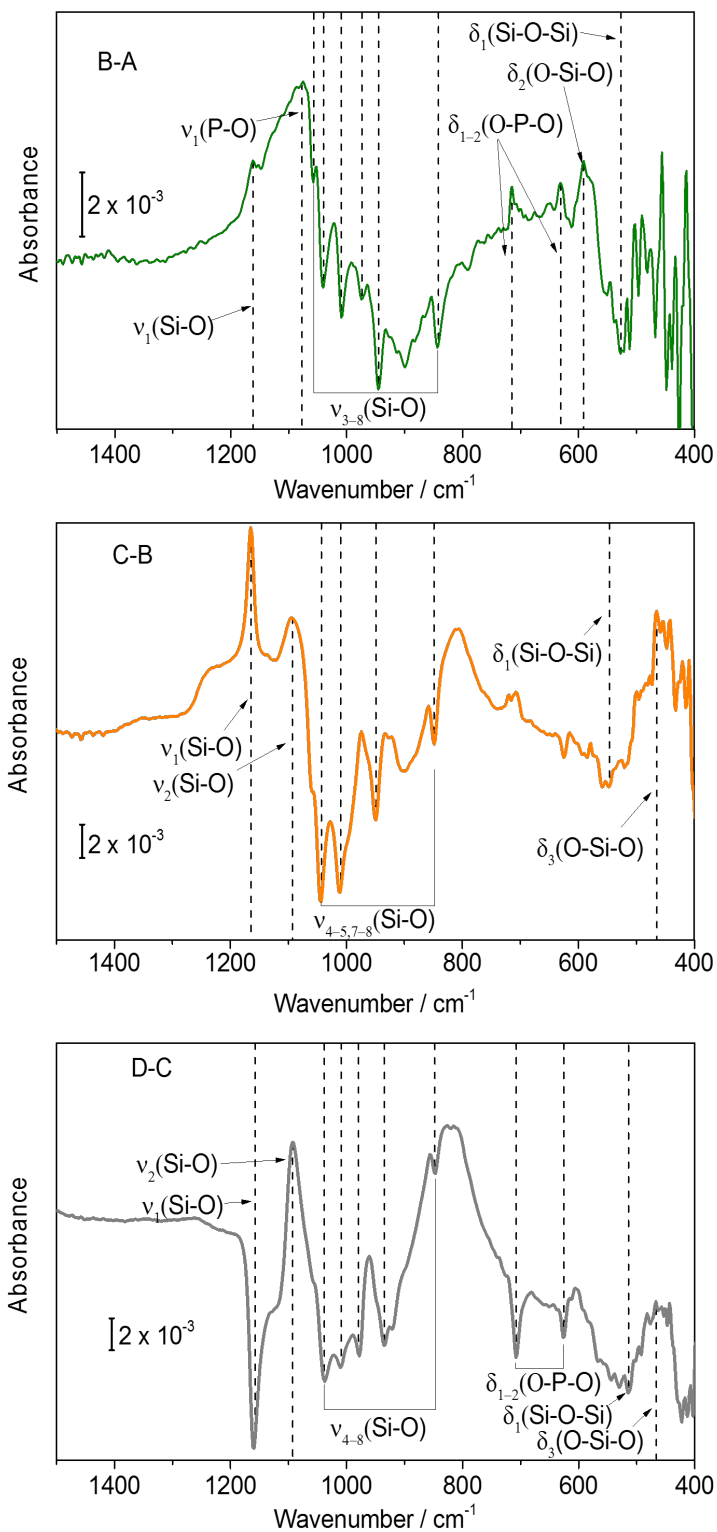


Figure 48: Difference IR spectra of every step represented in the figure 44, with the previous step as background. (B-A) Phosphates on C-S phases. (C-B) After heating, probe molecules inside the C-S structure. (D-C) After longer heating, producing the diffusion of phosphorus into the silicon wafer.

6.6 Application of Probe Molecules on C-S Phases

Next, probe molecules are applied on C-S phases (as described in figure 44). The difference IR spectra corresponding to the whole sensing process are shown in the figure 48. The first spectrum corresponds to the detection of the phosphates on the C-S phases (figure 48 B-A). The positive P-O stretching vibration is present, and the bending vibrations of the phosphate appear too (broad $\nu_1(\text{P-O})$ peak with a maximum at 1074 cm^{-1} and $\delta_{1-2}(\text{O-P-O})$ at 714 cm^{-1} and 625 cm^{-1}).¹³⁸ The negative peaks observed in the same figure, depicted as $\nu_{3-8}(\text{Si-O})$ correspond to the silicates that are modified by the formation of phosphates, (see Table 1, $\nu_{3-8}(\text{Si-O})$ at 1056 cm^{-1} , 1043 cm^{-1} , 1009 cm^{-1} , 979 cm^{-1} , 940 cm^{-1} and 840 cm^{-1}). There is only one positive peak of the Si-O vibration modes in the spectrum ($\nu_1(\text{Si-O})$ at 1160 cm^{-1}), the meaning of this peak is explained by a new concept called frustrated chains. The concept of frustrated chains is reflected in a shift of the Si-O-Si vibration mode to higher wavenumbers. This shift is related to the formation of calcium phosphates and causes a lower coordination of the silicate chains (lower coordinated = frustrated). A calculated model of this concept is shown in the figure 49. This model is representative to confirm that vibration modes of longer (higher coordinated) silicate chains shift to lower wavenumbers. In contrast, the vibration modes of the frustrated (lower coordinated) chains shift to higher wavenumbers.

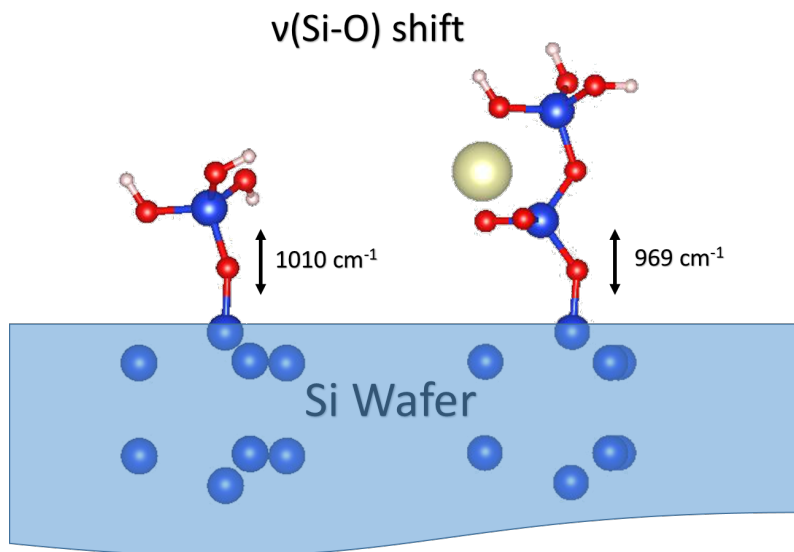


Figure 49: Calculated model for the shift of wavenumbers of $\nu(\text{Si-O})$ in silicate tetrahedral chains grafted to a silicon wafer respect to the length of the chain.

Figure 49 shows that the Si-O-Si vibration mode of a silicate chain shifts from 1010 cm^{-1} to 969 cm^{-1} when a two-tetrahedra chain is formed. This consideration is confirming the hypothesis mentioned before, that the 1160 cm^{-1} peak corresponds to a lower coordination of calcium in the tetrahedral chain.

In the figure 46 it was observed that the peak at 1160 cm^{-1} appears because of the formation of silicate tetrahedral chain, i.e. the dehydroxylation of C-S-H

phases. The principal responsible for the formation of such chains is the release of CaO. The coordination of the calcium, product of the reaction of CaO with the dehydroxylated Si-O tetrahedral compounds, results in an increment of the chains length. The further heating produces the incorporation of more Ca into the structure of the C-S phase increasing the Ca/Si ratio, which is evidenced by the formation of longer chains and lower wavenumbers. The vibration modes attributed to the frustrated chains, $\nu_1(\text{Si-O})$ at 1160 cm^{-1} appear once the sample is heated, and the ones of SiO_4 of the C-S phase partially disappear. However, the vibration modes of the phosphate remain unchanged. In the figure 48 C-B it can be seen how with the further heating, the peak corresponding to the frustrated chains keeps growing ($\nu_1(\text{Si-O})$ at 1160 cm^{-1}). This phenomenon is explained by the diffusion of the phosphates in the calcium silicates.

Once the phosphate has reached the interface of the wafer in the figure 48 D-C, the bending vibrations of phosphate begin to disappear, and surprisingly the Si-O vibrations do the same, showing at the same time new vibration modes, that are attributed to the reconstruction of C-S phases, which after 8 seconds of heating at $1000\text{ }^\circ\text{C}$ cease ($\nu_2(\text{Si-O})$ at 1095 cm^{-1} and $\delta_3(\text{O-Si-O})$ at 464 cm^{-1}).

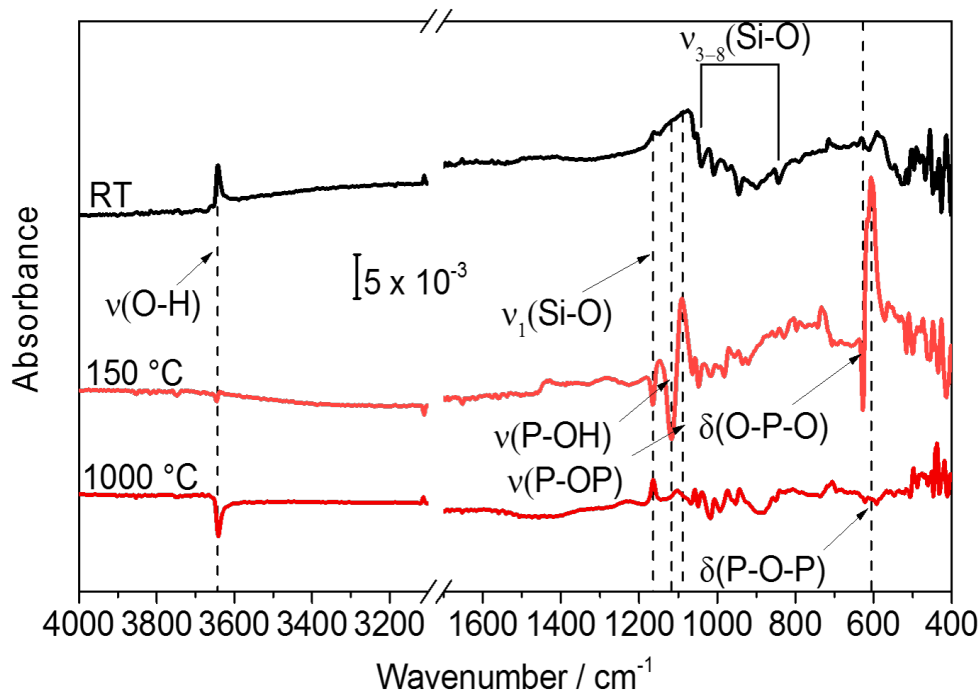
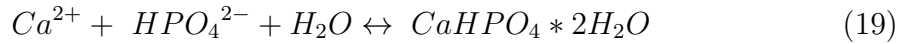


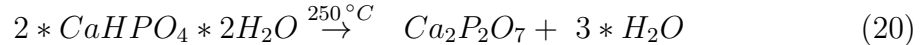
Figure 50: Difference IR spectra of C-S phases with a phosphate molecule. (top) After phosphate molecule deposition at RT with the C-S phases as background, (middle) after heating up to $150\text{ }^\circ\text{C}$ with the same sample at RT as background and (bottom) after heating up to $1000\text{ }^\circ\text{C}$, with the previous state as background.

6.7 Driving Force of the Diffusion of Phosphates and Phosphorus

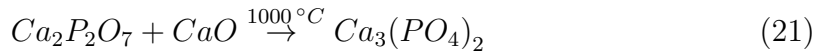
One possible approach to the supposed chemical driving force of the diffusion of phosphates through the C-S phases is presented. The black line in the figure 50 shows the spectrum of the first state of the phosphate molecule deposited on the C-S phases referenced to the heated and stable C-S phases on a wafer. As can be noticed, the phosphate on the surface is still hydroxylated ($\nu(\text{O-H})$ at 3640 cm^{-1}), which is here suggested to be CaHPO_4 . The mechanism of formation of this phosphate was already understood and explained in earlier publications.^{139–140} The release of a proton by the dissociation of the KH_2PO_4 induces the already known Metal-Proton Exchange Reaction (MPER), and forms the first calcium hydrogen phosphate on the surface, as depicted in the equation (19).^{30,10}



This compound is stable at room temperature, but after heating up to around $250 \text{ }^\circ\text{C}$, its transformation performs completely as described by the equation 20. The formation of new phosphate compounds is driven by the higher concentration of calcium on the way down to the silicon wafer, and the activation energy is provided by the high temperature.



In the figure 50, the spectrum of the system after heating up to $150 \text{ }^\circ\text{C}$ shows that the reaction described in the equation (20) has already started. The negative band of $\nu(\text{O-H})$ is the most remarkable change ($\nu(\text{O-H})$ at 3640 cm^{-1}). The shift observed in the stretching vibrations of P-OH ($\nu(\text{P-OH})$ at 1118 cm^{-1} to 1085 cm^{-1}) corresponds to the change of free tetrahedra of the CaHPO_4 to P-O stretching mode of P-O-P in $\text{Ca}_2\text{P}_2\text{O}_7$. Frustrated chains vibration mode disappears (Si-O systems react with the CaO to form the C-S phase). After $1000 \text{ }^\circ\text{C}$ the PO_4 has again advanced into the structure due to the calcium gradient as proposed by the equation (21).



The heat of formation of every compound was calculated, validating the series of reactions proposed for the product depicted in the equation (21).^{141–142}

The driving force of the diffusion of phosphates towards the silicon wafer was explained as a gradient of calcium concentration, increasing towards the silicon and a gradient of phosphorus, decreasing in the same direction. Calcium phosphates are formed in its way down, these compounds take the calcium of the silicates, producing a stronger vibration of the Si-O-Si bonds bridging the chains, which was observed by means of FTIR. Several authors have observed this vibration in similar systems, attributing this vibration mode to a more linear and less cross-linked structures than the one presented on SiO_2 networks.^{143–144} Others were even conscious of the influence of calcium in such vibration mode, relating it to a $\text{Ca/Si} < 1$.¹⁴⁵ But it was not evident until the probe molecules were applied as will be explained, also confirming all the statements made in the chapter 4.

At the silicon interface, the overall driving force was found to be the thermodynamic instability of P^{5+} in contact with silicon at high temperature, initiating a self-decomposition at 500 °C, as described by Longo et al.⁸⁹ After P diffusing into the silicon wafer, CaO as an end product is obtained on the surface, which reacts again with the Si-O system to produce C-S phases (see figure 48 D-C).

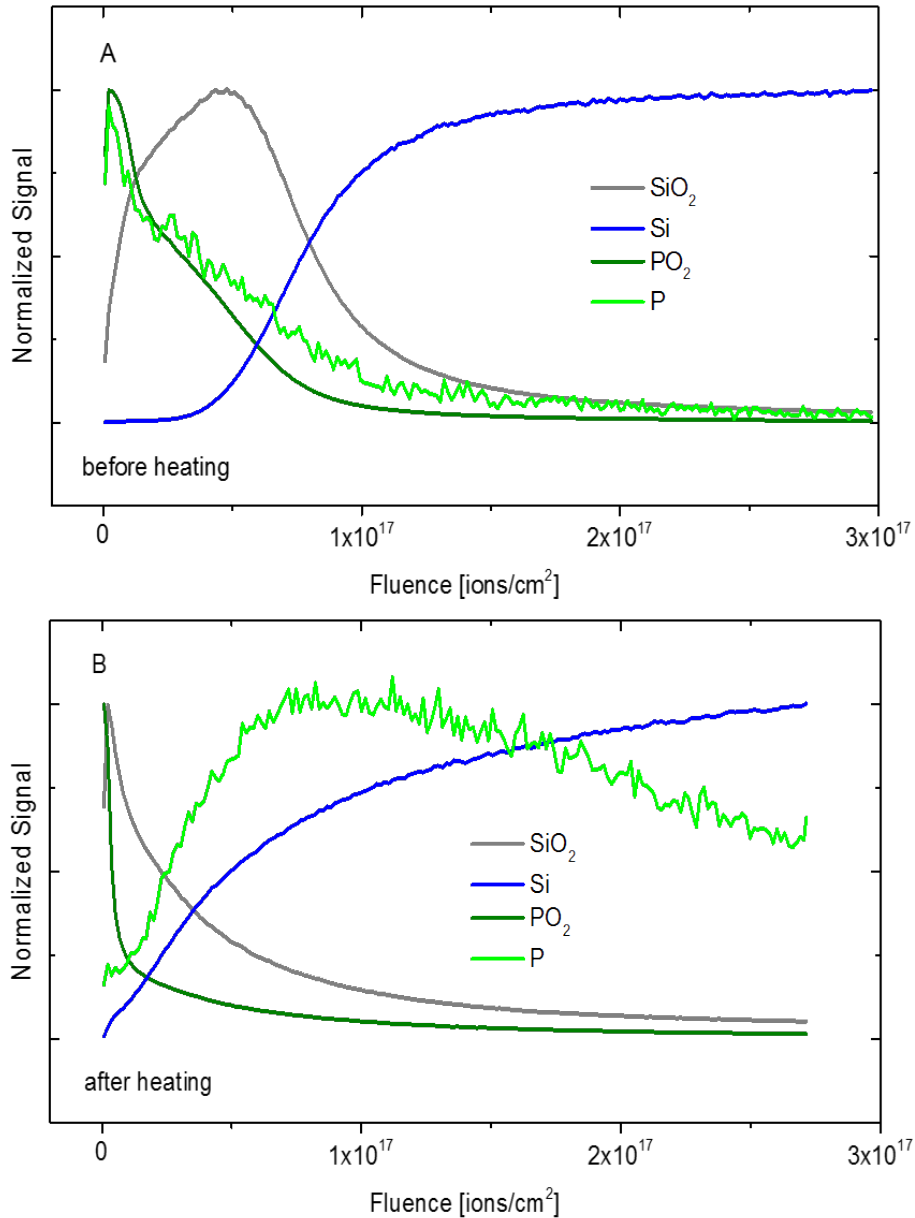


Figure 51: ToF-SIMS measurements of (gray line) silicon oxide, (blue line) silicon, (light green line) phosphorus and (dark green line) oxidized phosphorus on: (A) after the application of phosphates and (B) after heating up to 1000 °C.

6.8 ToF-SIMS Confirmation of the Diffusion

While the IR absorption spectrum provides evidence for the adsorption of phosphates, it is difficult to know if the silicon surface remains unoxidized because the SiO₂ vibration modes occur in the 1000-1250 cm⁻¹ region, overlapping the Si-O and associated oxygen vibrations.¹⁰⁵ Therefore, complementary ToF-SIMS measurements were applied to investigate the mass transport of phosphorus towards the C-S/Si-bulk interface, and to estimate the layer thickness of the C-S-H phases, which was approximately of 100 nm. In the figures 51.A and 51.B, the sputter profiles of negative fragments most representative for oxidized silicon (gray line), elementary silicon (blue line), oxidized phosphorus (dark green line) and reduced phosphorus (light green line) are shown. Figure 51.A depicts the situation after the deposition of phosphates on C-S phases. The mass transport of phosphates from the C-S-H/liquid interface is represented by the dark green line, a PO₂ fragment. Further fragments like PO₃ have been detected and follow the same line shape. The C-S/Si-bulk interface is found where the line of oxidized silicon (gray line) intersects the one of elementary silicon (blue line). Note that before heating the phosphates reach the C-S/Si-bulk interface, but they do not penetrate into the silicon (dark green line never goes behind gray line).

The situation completely changes after heating, as depicted in the figure 51.B. Again, the C-S/Si-bulk interface is found where the line of oxidized silicon (gray line) intersects the one of elementary silicon (blue line). Interestingly, the phosphates have been completely removed from the system. Instead, fragments of reduced phosphorus have been found to penetrate deeply into the silicon bulk. The maximum of the light green line is found behind the C-S/Si-bulk interface. Overall, the ToF-SIMS measurement has complementary confirmed the results of FTIR and given deeper insights into the mass transport from the C-S-H/liquid to the C-S/Si-bulk interface.

6.9 Summary

The use of phosphates as probe molecules to analyze the chemical structure of C-S phases was applied here, evidenced by FTIR. At room temperature the interaction is dominated by the formation of calcium phosphates, but in case of an increment of the temperature up to 1000 °C, the calcium-silicates phases are regenerated. The phosphate molecules, instead of falling apart, penetrate the structure driven by the concentration gradients, and dope the silicon wafer. The FTIR results were analyzed on the basis of first principles calculations and further supported by complementary Time-of-Flight Secondary Ion Mass Spectrometry (ToF-SIMS) experiments.

Exclusive information of the presented system was obtained from the in-situ deposition of probe molecules and heating:

- There are no long chains in the synthesized C-S-H phases on the silicon wafer, until the dehydroxylation takes place.
- The formation of such chains can be understood based on the interpretation of Si-O-Si vibration modes.

- Si-O-Si vibration modes shift to lower wavenumbers when more calcium is incorporated to the structure, thereby, increasing the Ca/Si ratio.

The length of the chains plays a very important role in the structure of calcium silicates, not only because of the mechanical properties associated with it, but also in the chemical corrosion produced by the Metal-Proton Exchange Reaction.^{30–31,56}

7 Conclusions and Perspectives

7.1 Conclusions

In this work several approaches were implemented to study the complex structure of Calcium-Silicates (C-S) and Calcium-Silicate-Hydrate (C-S-H) phases, which are the most important components of hydrated cement, the most used construction material by mankind. At the application of every approach, several interesting aspects of these compounds were analyzed.

In the first part of this dissertation, a well-known mineral, Wollastonite, was taken as a model for the reaction involved at the hydration, corrosion and protection of cementitious materials. The implementation of this mineral allowed to draw the conclusions that in presence of water, the Metal-Proton Exchange Reaction (MPER) leads surfaces to a non-stoichiometric thermodynamic ground state in equilibrium with a $\text{Ca}(\text{OH})_2$ solution, by the exchange of one Ca from the Wollastonite surface with two protons of the water. This exchange was observed to be dependent of the concentration of protons in the solution. On the Wollastonite (010) surfaces, the reaction occurs with a smaller kinetic barrier than on (001) surfaces, explaining the effect of anisotropy.

The application of Wollastonite as a model system for the study of chemical corrosion of concrete, allowed to study crystallographic effects. Using XRD, substantial changes in the shape of Wollastonite particles upon immersion into water were detected. A thorough theoretical analysis revealed that these shape changes, caused by a corrosion process referred to as MPER, cannot be explained by thermodynamic arguments alone, instead kinetic considerations have to be taken into account. The observed phenomena can be rationalized kinetically, where the MPER was found to be substantially accelerated on surfaces oriented perpendicular to the b-axis of Wollastonite ([010]-orientation), whereas for orientations parallel to the silicate tetrahedral chains the reaction is delayed.³⁰ These kinetic differences are responsible for the characteristic changes on the shape of the mineral particles when exposed to water. The length of the silicate tetrahedral chain plays a very important role in the mechanical properties such as stiffness and hardness, and also determines how the MPER will affect their structure.

The Wollastonite as a model presents also some limitations, such as its limited availability and relative impurity. To overcome these challenges, a new model was developed: the synthesis of C-S-H and C-S phases on silicon wafers. The uniqueness of this kind of substrate lies on the preparation of the model surface, which perfection highlights the importance of C-S and C-S-H surfaces, and makes it possible to model reactivity, stability and mechanical properties using first principles calculations. Several conclusions could be drawn as a consequence of the controlled synthesis of such compounds, which is very promising for several applications like sensing, catalysis, semiconductors, medicine between others.

Among the interesting aspects that can be studied by implementing the synthesized C-S-H and C-S phases on silicon wafers, the carbonation stands out. Two completely different types of carbonates have been analyzed: calcium-silicate carbonates (dry carbonates) and calcium carbonates. Both kind of carbonates are formed on ultrathin C-S-H phases if the presence of CO_2 is not avoided at the syn-

thesis. Even though some molecules can be adsorbed on the carbonates surface, there is no evidence for covalent bonds to the carbonate surface yet. Carbonates are not able to react with the molecules intended to passivate the surfaces of C-S-H phases and consequently should be first removed. After the characterization of the efficiency of every technique, it can be concluded that the removal of carbonates could be performed by any the implemented techniques with the respective adjustments.

The synthesis of C-S-H and C-S phases on silicon wafers is suitable to the application of several analytical methods. The application of phosphates as probe molecules to analyze their chemical structure, evidenced by FTIR, was presented. At room temperature the interaction is dominated by the formation of calcium phosphates, but in case of an increment of the temperature up to 1000 °C, the calcium-silicates phases are regenerated. The phosphate molecules, instead of falling apart, penetrate the structure driven by the concentration gradients, and dope the silicon wafer. The FTIR results were analyzed on the basis of first principles calculations and further supported by complementary Time-of-Flight Secondary Ion Mass Spectrometry (ToF-SIMS) experiments. Exclusive information of the presented system was obtained from the in-situ deposition of probe molecules and heating.

Overall in this work model systems were applied to improve the understanding of C-S-H and C-S phases and their respective reactions with some other compounds. The models proposed in this dissertation, namely Wollastonite and C-S-H phases synthesized on silicon wafers, were very helpful to draw important conclusions. However, these models present some limitations, which have to be overcome to improve the reach of their application. Among those limitations the most important are the difficulty to analyze hydration, since the C-S-H phases are synthesized on the silicon wafers and not from a powder. The analysis presented here does not include the influence of other compounds present on cement like aggregates, sulfates and different metals, which are very important for mechanical analysis, etc. However, the further research on these models will surely allow to overcome these obstacles.

Apart from the plenty conclusions that could be drawn in this work, many of them mentioned above, the development of the proposed models is relevant for the upcoming research. The successful synthesis of C-S-H and C-S phases on silicon wafers is very promising for many other applications that are not related with the cement and concrete research, some of them will be presented in the following.

7.2 Perspectives

From the conclusions drawn in this work, several applications in different research fields can be developed. In this section the possible directions of these fields are mentioned. All the perspectives described in this section can be developed in an ultra-high-vacuum chamber, which is shown in the figure 52 which is able to heat up the wafers, and to be filled with any necessary gas.

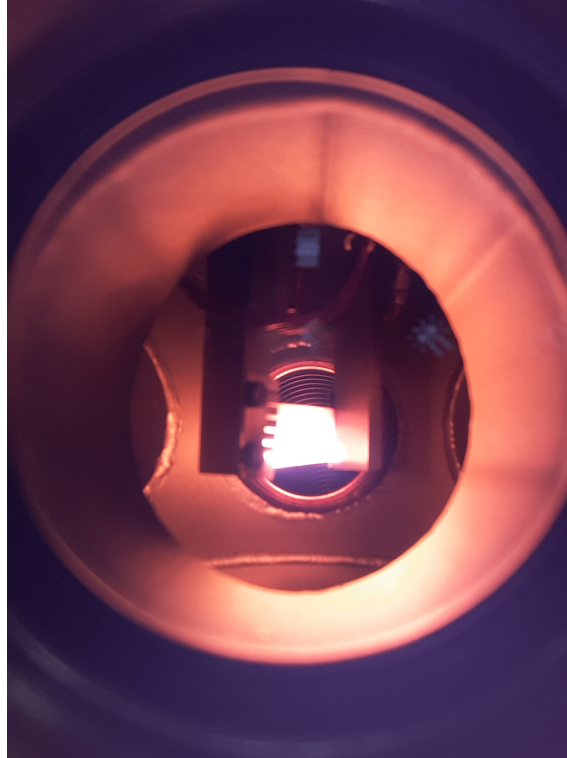


Figure 52: Inside of the ultra-high-vacuum chamber, while heating up a silicon wafer.

Corrosion vs Ca/Si ratio

The chemical corrosion of concrete was characterized by the MPER. The analysis was performed in Wollastonite, which well-known structure contains infinite silicate tetrahedral chains running along the b-axis. However, there are many open questions about how this reaction affects structures, where the $\text{Ca/Si} \neq 1$, for both C-S and C-S-H phases. The description of this dependence remains necessary, since it was shown that the MPER on Wollastonite leads to a new thermodynamic ground state, but no fundamental prediction can be found about the behavior of other structures, such as Tobermorite ($\text{Ca/Si} < 1$) or Jaffeite ($\text{Ca/Si} > 1$). Even when the experimental evidence shows that the MPER affects stronger phases with $\text{Ca/Si} > 1$. The approach developed in this work of the synthesis of C-S-H phases on silicon wafers was able to achieve different Ca/Si ratios. Thence, the further investigation on the synthesis with alcohol mixtures and different thermodynamic conditions are the experimental support for the necessary calculations to determine the effects of MPER in different phases.

Passivation of Carbonates-free C-S-H Phases

Having analyzed the effect of water induced corrosion in the C-S-H and C-S phases, the following step is to try to avoid it. As it was mentioned in the chapter 5, the passivation of surfaces by specific molecules was one of the most popular action against that problem. However, as discussed before, the activation of the surfaces is

necessary before any reaction of passivation, due to the carbonates present on the surface. The principal issue of the activation is that the structure of the material is changed during the process and further investigation of not-invasive methods remains necessary. Nevertheless, the synthesis of C-S-H and C-S phases on silicon wafers can be performed under protected atmospheres, whereat the formation of carbonates is avoided. These phases are then appropriated to the investigation of the functionalization to protect materials against corrosion.

Mechanical Properties Supported by Means of Ab Initio Calculations

Since the C-S-H and C-S phases on silicon wafers are also able to reflect IR light, the bending of these samples can be also investigated by means of FTIR. Furthermore, the C-S phases that are recognized and identified in XRD can be calculated by means of first principles calculations and the strains of several phases can be investigated. The mechanical properties of construction materials are well known, but the singular effects of every change in the structure by external compounds, like during corrosion, or processes to improve the properties with aggregates, are not completely understood. This lack can be filled with this proposed investigation path.

Metal-Metal Exchange Reaction (MMER): Catalysts Made of Concrete

The corrosion of Wollastonite or other C-S phases is not the only effect that is controlled by the MPER. The exchange of Calcium with protons from the water is the key in that mechanism, but another metal can be also exchanged. The different energetic barrier that will be necessary to overcome to produce the exchange of other metals is very interesting, since in this way metals against metals can be exchanged. In the chapter 5, it was mentioned that the production of CO₂ needs to be controlled, because of the earth warming. 5% of the world's production of CO₂ is released during the manufacturing of cement. Reactions like Methanation, responsible for the transformation of carbon dioxide into methane, are very popular nowadays. The principal inconvenient for this reactions to be implemented in every industry is the development of catalysts. Consequently, the exchange of Calcium against metals that can be used as catalysts remains very promising, e.g. Nickel for methanation reactions. Such exchange produces Nickel-containing concrete, which due to its porosity and stability appears suitable for catalysis research.

Ca/Si ratio Effects at Synthesis of Compounds for the Medicine

In the chapter 4, it was mentioned that the synthesis of several phosphorus compounds like hydroxyapatite are very important for the medicine research. These compounds can be synthesized by exchange of silicates in the C-S-H or C-S phases by phosphates, due to their stronger dissociation. The Ca/Si ratio is controlled at the synthesis of C-S-H phases on silicon wafers by the MPER. Modifying the equilibrium, different Ca/Si ratios can be obtained. This modification will also affect the synthesis of bio-compounds and is also very interesting for this field.

8 Acknowledgements

This thesis was made by myself, but I would not have been able to achieve it without thinking about my family every day. The love, support and understanding of my mother Edith, brother Marcos and sister Micaela are the force that drives me to get up every day and smile. Maia and her family were also my company the whole time, she always found the way to make me smile and I am very thankful for that, it brought me to this point.

I want to thank to the Deutsche Forschungsgemeinschaft (DFG) for financial support through the project TH 1566/3-1 and 2 - Modell-Entwicklung Mineralischer Grenzflächen.

Thanks to Prof. Dr. Wöll, who accepted me as his PhD student and helped me every time I asked it.

Very special thanks to Dr. Peter Thissen. He picked me up as his collaborator in this project, and I learned very much from him. He was responsible for the advances that I made and advised me wisely every day.

Thanks to Priv. Doz. Dr. Artur Böttcher for accepting being the second examiner of my thesis and for inserting me to the world of teaching. Also I want to acknowledge Priv. Doz. Dr. Andreas-Neil Unterreiner for accepting and helping me at the coordination of practices in physical chemistry.

Many thanks to my colleagues:

Samuel Bergdolt was my companion along this long way and was there every time that I needed him.

Fabrice Laye had always the patience to help me with my crazy experiments and my horrific english. He became a really good friend.

Franz Königer was my guide and instructor in the electrical experiments. He was always prepared and available.

Dr. Peter G. Weidler helped me a lot. His knowledge accelerated my work very much.

Peter Krolla-Siedenstein transferred me a part of his great knowledge in experimental research, he was also very patient and, most notably very kind.

Florian Schnetzer and Priv. Doz. Dr. Katja Emmerich introduced me to a new research field, the clay minerals. This work was not included in this thesis, but it helped me to open my mind to different structures and phenomena.

Roberto C. Longo Pazos helped me with my calculations several times. He was also very patient and helpful.

I also want to thank to the Texas Advanced Computing Center (TACC) for providing me with computing capacity.

All my department colleagues were helpful for me, either supporting me with experimental research or discussing my results, among them: Prof. Andreas Gerdes, Dr. Matthias Schwotzer, Beatriz Arevalo Galvan, Jonas Kaltenbach, Thomas Sollich, Mohammed Monjur ul Islam, Baburam Bhat, Olivia Wenzel, Jens Heinrichs, Dr. Carsten Natzeck.

9 Publications

Giraud, N.; Krolla-Sidenstein, P.; Bergdolt, S.; Heinle, M.; Gliemann, H.; Messerschmidt, F.; Brüner, P.; Thissen, P., Early Stage Hydration of Wollastonite: Kinetic Aspects of the Metal-Proton Exchange Reaction.

The Journal of Physical Chemistry C **2015**, *119*, 10493-10499.

Giraud, N.; Thissen, P., Carbonation Competing Functionalization on Calcium-Silicate-Hydrates: Investigation of Four Promising Surface-Activation Techniques.

ACS Sustainability Chemistry & Engineering **2016**, *4*, 3985-3994.

Giraud, N.; Weidler, P. G.; Laye, F.; Schwotzer, M.; Lahann, J.; Wöll, C.; Thissen, P., Corrosion of Concrete by Water-Induced Metal-Proton Exchange.

The Journal of Physical Chemistry C **2016**, *120*, 22455-22459.

Giraud, N.; Bergdolt, S.; Wohlgemuth, J.; Welle, A.; Schuhmann, A.; Königer, F.; Thissen, P., Calcium-Silicate Phases Explained by High Temperature Resistant Phosphate-Probe Molecules.

Langmuir **2016**, *32*, 13577-13584.

Schnetzer, F.; Thissen, P.; **Giraud**, N.; Emmerich, K., Unraveling the Coupled Processes of (De)Hydration and Structural Changes in Na⁺-Saturated Montmorillonite.

The Journal of Physical Chemistry C **2016**, *120*, 15282-15287.

10 References

- (1) Thomas, J. J.; Jennings, H. M.; Chen, J. J., Influence of Nucleation Seeding on the Hydration Mechanisms of Tricalcium Silicate and Cement. *The Journal of Physical Chemistry C* **2009**, *113*, 4327-4334.
- (2) Garrault, S.; Behr, T.; Nonat, A., Formation of the C-S-H Layer During Early Hydration of Tricalcium Silicate Grains with Different Sizes. *The Journal of Physical Chemistry B* **2006**, *110*, 270-275.
- (3) Allen, A. J.; Thomas, J. J.; Jennings, H. M., Composition and Density of Nanoscale Calcium-Silicate-Hydrate in Cement. *Nature Materials* **2007**, *6*, 311-316.
- (4) Pujari, S. P.; Scheres, L.; Marcelis, A. T. M.; Zuilhof, H., Covalent Surface Modification of Oxide Surfaces. *Angewandte Chemie International Edition* **2014**, *53*, 6322-6356.
- (5) Survey, U. S. G., Mineral Commodity Summaries. Survey, U. S. G., Ed. **2015**; Vol. January 2015.
- (6) Nonat, A., The Structure and Stoichiometry of C-S-H. *Cement and Concrete Research* **2004**, *34*, 1521-1528.
- (7) Schott, J.; Pokrovsky, O. S.; Spalla, O.; Devreux, F.; Gloter, A.; Mielczarski, J. A., Formation, Growth and Transformation of Leached Layers During Silicate Minerals Dissolution: The Example of Wollastonite. *Geochimica Cosmochimica Acta* **2012**, *98*, 259-281.
- (8) Rawal, A.; Smith, B. J.; Athens, G. L.; Edwards, C. L.; Roberts, L.; Gupta, V.; Chmelka, B. F., Molecular Silicate and Aluminate Species in Anhydrous and Hydrated Cements. *Journal of the American Chemical Society* **2010**, *132*, 7321-7337.
- (9) Richardson, I. G., The Calcium Silicate Hydrates. *Cement and Concrete Research* **2008**, *38*, 137-158.
- (10) Sanna, S.; Schmidt, W. G.; Thissen, P., Formation of Hydroxyl Groups at Calcium-Silicate-Hydrate (C-S-H): Coexistence of Ca-OH and Si-OH on Wollastonite(001). *The Journal of Physical Chemistry C* **2014**, *118*, 8007-8013.
- (11) Richardson, I. G., The Nature of C-S-H in Hardened Cements. *Cement and Concrete Research* **1999**, *29*, 1131-1147.
- (12) Buerger, M. J., The Arrangement of Atoms in Crystals of the Wollastonite Group of Metasilicates. *Proceedings of the National Academy of Sciences USA* **1956**, *42*, 113-116.
- (13) Dalas, E.; Klepetsanis, P.; Koutsoukos, P. G., The Overgrowth of Calcium Carbonate on Poly(Vinyl Chloride-Co-Vinyl Acetate-Co-Maleic Acid). *Langmuir* **1999**, *15*, 8322-8327.
- (14) Cong, H.-P.; Yu, S.-H., Shape Control of Cobalt Carbonate Particles by a Hydrothermal Process in a Mixed Solvent: An Efficient Precursor to Nanoporous Cobalt Oxide Architectures and Their Sensing Property. *Crystal Growth and Design* **2009**, *9*, 210-217.
- (15) Huijgen, W. J. J.; Comans, R. N. J., Mineral CO₂ Sequestration by Steel Slag Carbonation. *Environmental Science and Technology* **2005**, *39*, 9676-9682.
- (16) Lammers, K.; Murphy, R.; Riendeau, A.; Smirnov, A.; Schoonen, M. A. A.; Strongin, D. R., CO₂ Sequestration through Mineral Carbonation of Iron Oxyhy-

- droxides. *Environmental Science and Technology* **2011**, *45*, 10422-10428.
- (17) Schneider, S. H., The Greenhouse Effect: Science and Policy. *Science* **1989**, *243*, 771-781.
- (18) Kelemen, P. B.; Matter, J., In Situ Carbonation of Peridotite for CO₂ Storage. *Proceedings of the National Academy of Sciences USA* **2008**, *105*, 17295-17300.
- (19) Rochelle, C. A.; Czernichowski-Lauriol, I.; Milodowski, A. E., The Impact of Chemical Reactions on CO₂ Storage in Geological Formations: A Brief Review. *Geological Society* **2004**, *233*, 87-106.
- (20) Harrison, A. L.; Power, I. M.; Dipple, G. M., Accelerated Carbonation of Brucite in Mine Tailings for Carbon Sequestration. *Environmental Science and Technology* **2013**, *47*, 126-134.
- (21) Huntzinger, D. N.; Gierke, J. S.; Kawatra, S. K.; Eisele, T. C.; Sitter, L. L., Carbon Dioxide Sequestration in Cement Kiln Dust through Mineral Carbonation. *Environmental Science and Technology* **2009**, *43*, 1986-1992.
- (22) Morandea, A. E.; White, C. E., Role of Magnesium-Stabilized Amorphous Calcium Carbonate in Mitigating the Extent of Carbonation in Alkali-Activated Slag. *Chemistry of Materials* **2015**, *27*, 6625-6634.
- (23) Wang, C.; Li, W.; Yang, Z.; Chen, Y.; Shao, W.; Ji, J., An Invisible Soil Acidification: Critical Role of Soil Carbonate and Its Impact on Heavy Metal Bioavailability. *Science Reports* **2015**, *5*, 12735.
- (24) Haselbach, L. M.; Ma, S., Potential for Carbon Adsorption on Concrete: Surface Xps Analyses. *Environmental Science and Technology* **2008**, *42*, 5329-5334.
- (25) Pade, C.; Guimaraes, M., The CO₂ Uptake of Concrete in a 100 year Perspective. *Cement and Concrete Research* **2007**, *37*, 1348-1356.
- (26) Galan, I.; Andrade, C.; Mora, P.; Sanjuan, M. A., Sequestration of Co₂ by Concrete Carbonation. *Environmental Science and Technology* **2010**, *44*, 3181-3186.
- (27) Eikeland, E.; Blichfeld, A. B.; Tyrsted, C.; Jensen, A.; Iversen, B. B., Optimized Carbonation of Magnesium Silicate Mineral for CO₂ Storage. *ACS Applied Materials & Interfaces* **2015**, *7*, 5258-5264.
- (28) Vance, K.; Falzone, G.; Pignatelli, I.; Bauchy, M.; Balonis, M.; Sant, G., Direct Carbonation of Ca(OH)₂ Using Liquid and Supercritical CO₂: Implications for Carbon-Neutral Cementation. *Industrial and Engineering Chemical Research* **2015**, *54*, 8908-8918.
- (29) Koch, G. H.; Turner-Fairbank Highway Research, C.; International, N.; Laboratories, C. C. T.; United, S., *Corrosion Cost and Preventive Strategies in the United States*; Turner-Fairbank Highway Research Center ; Available through the National Technical Information Service: McLean, Va.: Springfield, Va., **2002**.
- (30) Giraud, N.; Krolla-Sidenstein, P.; Bergdolt, S.; Heinle, M.; Gliemann, H.; Messerschmidt, F.; Brüner, P.; Thissen, P., Early Stage Hydration of Wollastonite: Kinetic Aspects of the Metal-Proton Exchange Reaction. *The Journal of Physical Chemistry C* **2015**, *119*, 10493-10499.
- (31) Hou, D.; Zhang, J.; Li, Z.; Zhu, Y., Uniaxial Tension Study of Calcium Silicate Hydrate (C-S-H): Structure, Dynamics and Mechanical Properties. *Materials and Structures* **2014**, 1-14.

- (32) Longo, R. C.; Cho, K.; Br uner, P.; Welle, A.; Gerdes, A.; Thissen, P., Carbonation of Wollastonite(001) Competing Hydration: Microscopic Insights from Ion Spectroscopy and Density Functional Theory. *ACS Applied Materials & Interfaces* **2015**, *7*, 4706-4712.
- (33) Black, L.; Breen, C.; Yarwood, J.; Garbev, K.; Stemmermann, P.; Gasharova, B., Structural Features of C-S-H(I) and Its Carbonation in Air—a Raman Spectroscopic Study. Part II: Carbonated Phases. *Journal of the American Ceramic Society* **2007**, *90*, 908-917.
- (34) Montes-Hernandez, G.; Pommerol, A.; Renard, F.; Beck, P.; Quirico, E.; Brissaud, O., In Situ Kinetic Measurements of Gas-Solid Carbonation of Ca(OH)₂ by Using an Infrared Microscope Coupled to a Reaction Cell. *Chemical Engineering Journal* **2010**, *161*, 250-256.
- (35) Pelisser, F.; Gleize, P. J. P.; Mikowski, A., Effect of the Ca/Si Molar Ratio on the Micro/Nanomechanical Properties of Synthetic C-S-H Measured by Nanoindentation. *The Journal of Physical Chemistry C* **2012**, *116*, 17219-17227.
- (36) Ebbert, C.; Grundmeier, G.; Buitkamp, N.; Kr oger, A.; Messerschmidt, F.; Thissen, P., Toward a Microscopic Understanding of the Calcium-Silicate-Hydrates/Water Interface. *Applied Surface Science* **2014**, *290*, 207-214.
- (37) Giraud, N.; Thissen, P., Carbonation Competing Functionalization on Calcium-Silicate-Hydrates: Investigation of Four Promising Surface-Activation Techniques. *ACS Sustainable Chemistry and Engineering* **2016**, *4*, 3985-3994.
- (38) Schiewer, S.; Volesky, B., Modeling of the Proton-Metal Ion Exchange in Biosorption. *Environmental Science & Technology* **1995**, *29*, 3049-3058.
- (39) Oelkers, E. H.; Golubev, S. V.; Chairat, C.; Pokrovsky, O. S.; Schott, J., The Surface Chemistry of Multi-Oxide Silicates. *Geochimica Cosmochimica Acta* **2009**, *73*, 4617-4634.
- (40) Casey, W. H.; Westrich, H. R.; Banfield, J. F.; Ferruzzi, G.; Arnold, G. W., Leaching and Reconstruction at the Surfaces of Dissolving Chain-Silicate Minerals. *Nature* **1993**, *366*, 253-256.
- (41) Kresse, G.; Furthm ller, J., Efficient Iterative Schemes for Ab Initio Total-Energy Calculations Using a Plane-Wave Basis Set. *Physical Reviews B: Condensed Matter* **1996**, *54*, 11169-11186.
- (42) Kresse, G.; Joubert, D., From Ultrasoft Pseudopotentials to the Projector Augmented-Wave Method. *Physical Reviews B: Condensed Matter* **1999**, *59*, 1758-1775.
- (43) Monkhorst, H. J.; Pack, J. D., Special Points for Brillouin-Zone Integrations. *Physical Reviews B: Condensed Matter* **1976**, *13*, 5188-5192.
- (44) Perdew, J. P.; Burke, K.; Ernzerhof, M., Generalized Gradient Approximation Made Simple (Vol 77, Pg 3865, 1996). *Physical Reviews Letters* **1997**, *78*, 1396-1396.
- (45) Thissen, P.; Peixoto, T.; Longo, R. C.; Peng, W.; Schmidt, W. G.; Cho, K.; Chabal, Y. J., Activation of Surface Hydroxyl Groups by Modification of H-Terminated Si(111) Surfaces. *Journal of the American Chemical Society* **2012**, *134*, 8869-8874.
- (46) Thissen, P.; Grundmeier, G.; Wippermann, S.; Schmidt, W. G., Water Adsorption on the Alpha-Al₂O₃(0001) Surface. *Physical Reviews B: Condensed Matter*

2009, *80*, 245403.

(47) Thierfelder, C.; Hermann, A.; Schwerdtfeger, P.; Schmidt, W. G., Strongly Bonded Water Monomers on the Ice Ih Basal Plane: Density-Functional Calculations. *Physical Reviews B: Condensed Matter* **2006**, *74*, 045422.

(48) Thissen, P.; Seitz, O.; Chabal, Y. J., Wet Chemical Surface Functionalization of Oxide-Free Silicon. *Progress in Surface Science* **2012**, *87*, 272-290.

(49) Štich, I.; Car, R.; Parrinello, M.; Baroni, S., Conjugate Gradient Minimization of the Energy Functional: A New Method for Electronic Structure Calculation. *Physical Review B* **1989**, *39*, 4997-5004.

(50) Jonsson, H. M., G.; Jacobsen, K. W. , Nudged Elastic Band Method for Finding Minimum Energy Paths of Transitions. In *Classical and Quantum Dynamics in Condensed Phase Simulations*, Berne, B. J. C., G.; Coker, D. F. , Ed. World Scientific. Singapore, **1998**.

(51) Payne, M. C.; Teter, M. P.; Allan, D. C.; Arias, T. A.; Joannopoulos, J. D., Iterative Minimization Techniques for Ab Initio Total-Energy Calculations: Molecular Dynamics and Conjugate Gradients. *Reviews of Modern Physics* **1992**, *64*, 1045-1097.

(52) Brown, G.; Gu, B., The Chemistry of Perchlorate in the Environment. In *Perchlorate*, Gu, B.; Coates, J., Eds. Springer US: **2006**; 17-47.

(53) Kundu, T. K.; Hanumtntha Rao, S.; Parker, S. C., Atomistic Simulation of the Surface Structure of Wollastonite. *Chemical Physics Letters* **2003**, *377*, 81-92.

(54) Brinker, C. J., Hydrolysis and Condensation of Silicates: Effects on Structure. *Journal of Non-Crystalline Solids* **1988**, *100*, 31-50.

(55) Sharpe, P. J. H.; DeMichele, D. W., Reaction Kinetics of Poikilotherm Development. *Journal of Theoretical Bioogy* **1977**, *64*, 649-670.

(56) Giraud, N.; Weidler, P. G.; Laye, F.; Schwotzer, M.; Lahann, J.; Wöll, C.; Thissen, P., Corrosion of Concrete by Water-Induced Metal-Proton Exchange. *The Journal of Physical Chemistry C* **2016**, *120*, 22455-22459.

(57) Ringe, E.; Van Duyne, R. P.; Marks, L. D., Wulff Construction for Alloy Nanoparticles. *Nano Letters* **2011**, *11*, 3399-3403.

(58) Dobrushin, R. L.; Kotecký, R.; Shlosman, S., *Wulff Construction: A Global Shape from Local Interaction*; American mathematical society Providence, Rhode Island, **1992**.

(59) Roosen, A. R.; McCormack, R. P.; Carter, W. C., Wulffman: A Tool for the Calculation and Display of Crystal Shapes. *Computational Materials Science* **1998**, *11*, 16-26.

(60) Geysersmans, P.; Finocchi, F.; Goniakowski, J.; Hacquart, R.; Jupille, J., Combination of (100), (110) and (111) Facets in MgO Crystals Shapes from Dry to Wet Environment. *Physical Chemistry Chemical Physics* **2009**, *11*, 2228-2233.

(61) Kresse, G.; Hafner, J., Ab Initio Molecular Dynamics for Liquid Metals. *Physical Reviews B: Condensed Matter* **1993**, *47*, 558-561.

(62) Himmel, D.; Goll, S. K.; Leito, I.; Krossing, I., A Unified pH Scale for All Phases. *Angewandte Chemie International Edition* **2010**, *49*, 6885-6888.

(63) Weidenthaler, C., Pitfalls in the Characterization of Nanoporous and Nano-sized Materials. *Nanoscale* **2011**, *3*, 792-810.

(64) Langford, J. I.; Wilson, A. J. C., Scherrer after Sixty Years: A Survey

and Some New Results in the Determination of Crystallite Size. *Journal of Applied Crystallography* **1978**, *11*, 102-113.

(65) Survey, U. S. G. *Wollastonite : A Versatile Industrial Mineral*; U.S. Geological Survey: **2001**.

(66) Malyi, O. I.; Kulish, V. V.; Persson, C., In Search of New Reconstructions of (001) α -Quartz Surface: A First Principles Study. *RSC Advances* **2014**, *4*, 55599-55603.

(67) Goumans, T. P. M.; Wander, A.; Brown, W. A.; Catlow, C. R. A., Structure and Stability of the (001) α -Quartz Surface. *Physical Chemistry Chemical Physics* **2007**, *9*, 2146-2152.

(68) de Leeuw, N. H.; Higgins, F. M.; Parker, S. C., Modeling the Surface Structure and Stability of Alpha-Quartz. *The Journal of Physical Chemistry B* **1999**, *103*, 1270-1277.

(69) Bauchy, M.; Abdolhosseini Qomi, M. J.; Bichara, C.; Ulm, F.-J.; Pellenq, R. J. M., Nanoscale Structure of Cement: Viewpoint of Rigidity Theory. *The Journal of Physical Chemistry C* **2014**, *118*, 12485-12493.

(70) Pellenq, R. J.-M.; Kushima, A.; Shahsavari, R.; Van Vliet, K. J.; Buehler, M. J.; Yip, S.; Ulm, F.-J., A Realistic Molecular Model of Cement Hydrates. *Proceedings of the National Academy of Science* **2009**, *106*, 16102-16107.

(71) Durgun, E.; Manzano, H.; Kumar, P. V.; Grossman, J. C., The Characterization, Stability, and Reactivity of Synthetic Calcium Silicate Surfaces from First Principles. *The Journal of Physical Chemistry C* **2014**, *118*, 15214-15219.

(72) Giraud, N. B., S.; Wohlgemuth, J.; Welle, A.; Schuhmann, A.; Königer, F.; Thissen, P., Calcium-Silicate Phases Explained by High Temperature Resistant Phosphate-Probe Molecules. *Langmuir* **2016**, *32*, 13577-13584.

(73) Schoenitz, M.; Navrotsky, A.; Ross, N., Enthalpy of Formation of $\text{Ca Si}_2\text{O}_5$, a Quenched High-Pressure Phase with Pentacoordinate Silicon. *Physics and Chemistry of Minerals* **2001**, *28*, 57-60.

(74) Higashi, G. S.; Chabal, Y. J.; Trucks, G. W.; Raghavachari, K., Ideal Hydrogen Termination of the Si(111) Surface. *Applied Physics Letters* **1990**, *56*, 656-658.

(75) Venkatesh, R. P.; Prasad, Y. N.; Tae-Young, K.; ooung-Jae, K.; pin-GoY, r., Effect of Alkaline Ph on Polishing and Etching of Single and Polycrystalline Silicon. *Japanese Journal of Applied Physics* **2012**, *51*, 071301.

(76) Levenspiel, O., Chemical Reaction Engineering. *Industrial & engineering chemistry research* **1999**, *38*, 4140-4143.

(77) Morrow, B. A.; McFarlan, A. J., Surface Vibrational Modes of Silanol Groups on Silica. *The Journal of Physical Chemistry* **1992**, *96*, 1395-1400.

(78) Vega, A.; Thissen, P.; Chabal, Y. J., Environment-Controlled Tethering by Aggregation and Growth of Phosphonic Acid Monolayers on Silicon Oxide. *Langmuir* **2012**, *28*, 8046-8051.

(79) Paluszkiwicz, C.; Błażewicz, M.; Podporska, J.; Gumuła, T., Nucleation of Hydroxyapatite Layer on Wollastonite Material Surface: FTIR Studies. *Vibrational Spectroscopy* **2008**, *48*, 263-268.

(80) Lin, K.; Lin, C.; Zeng, Y., High Mechanical Strength Bioactive Wollastonite Bioceramics Sintered from Nanofibers. *RSC Advances* **2016**, *6*, 13867-13872.

- (81) Kudoh, Y.; Kanzaki, M., Crystal Chemical Characteristics of Alpha-CaSi₂O₅, a New High Pressure Calcium Silicate with Five-Coordinated Silicon Synthesized at 1500°C and 10 GPa. *Physics and Chemistry of Minerals* **1998**, *25*, 429-433.
- (82) Akaogi, M.; Yano, M.; Tejima, Y.; Iijima, M.; Kojitani, H., High-Pressure Transitions of Diopside and Wollastonite: Phase Equilibria and Thermochemistry of CaMgSiO₆, CaSiO₃ and CaSi₂O₅ - CaSiTiO₅ System. *Physics of the Earth and Planetary Interiors* **2004**, *143-144*, 145-156.
- (83) Lin, K.; Chang, J.; Chen, G.; Ruan, M.; Ning, C., A Simple Method to Synthesize Single-Crystalline Beta-Wollastonite Nanowires. *Journal of Crystal Growth* **2007**, *300*, 267-271.
- (84) Emmerich, K.; Koeniger, F.; Kaden, H.; Thissen, P., Microscopic Structure and Properties of Discrete Water Layer in Na-Exchanged Montmorillonite. *Journal of Colloid and Interface Science* **2015**, *448*, 24-31.
- (85) Merlino, S.; Bonaccorsi, I.; Armbruster, T., Tobermorites: Their real Structure and Order-Disorder (Od) Character. *American Mineralogist* **1999**, *84*, 1613-1621.
- (86) Manzano, H.; Dolado, J.; Guerrero, A.; Ayuela, A., Mechanical Properties of Crystalline Calcium-Silicate-Hydrates: Comparison with Cementitious C-S-H Gels. *physica status solidi (a)* **2007**, *204*, 1775-1780.
- (87) Ponrouch, A.; Frontera, C.; Barde, F.; Palacin, M. R., Towards a Calcium-Based Rechargeable Battery. *Nature Materials* **2016**, *15*, 169-172.
- (88) Stewart, A.; Schlosser, B.; Douglas, E. P., Surface Modification of Cured Cement Pastes by Silane Coupling Agents. *ACS Applied Materials & Interfaces* **2013**, *5*, 1218-1225.
- (89) Longo, R. C.; Cho, K.; Schmidt, W. G.; Chabal, Y. J.; Thissen, P., Monolayer Doping Via Phosphonic Acid Grafting on Silicon: Microscopic Insight from Infrared Spectroscopy and Density Functional Theory Calculations. *Advanced Functional Materials* **2013**, *23*, 3471-3477.
- (90) Lim, S.-F.; Zheng, Y.-M.; Chen, J. P., Organic Arsenic Adsorption onto a Magnetic Sorbent. *Langmuir* **2009**, *25*, 4973-4978.
- (91) Zhang, J.; Stanforth, R., Slow Adsorption Reaction between Arsenic Species and Goethite Alpha-FeOOH: Diffusion or Heterogeneous Surface Reaction Control. *Langmuir* **2005**, *21*, 2895-2901.
- (92) Mori, K.; Yamaguchi, K.; Hara, T.; Mizugaki, T.; Ebitani, K.; Kaneda, K., Controlled Synthesis of Hydroxyapatite-Supported Palladium Complexes as Highly Efficient Heterogeneous Catalysts. *Journal of the American Chemical Society* **2002**, *124*, 11572-11573.
- (93) McKelvie, I. D.; Peat, D. M.; Worsfold, P. J. In *Analytical Perspective. Techniques for the Quantification and Speciation of Phosphorus in Natural Waters*, Anal. Proc. Incl. Anal. Comm., Royal Society of Chemistry: **1995**; pp 437-445.
- (94) Prati, C.; Gandolfi, M. G., Calcium Silicate Bioactive Cements: Biological Perspectives and Clinical Applications. *Dental Materials* **2015**, *31*, 351-370.
- (95) Vonlanthen, P.; Bittner, D.; Hudson, A. G.; Young, K. A.; Muller, R.; Lundsgaard-Hansen, B.; Roy, D.; Di Piazza, S.; Largiadere, C. R.; Seehausen, O., Eutrophication Causes Speciation Reversal in Whitefish Adaptive Radiations. *Nature* **2012**, *482*, 357-362.

- (96) Sips, R., On the Structure of a Catalyst Surface. *The Journal of Chemical Physics* **1948**, *16*, 490-495.
- (97) Lakshitanov, L. Z.; Stipp, S. L. S., Interaction between Dissolved Silica and Calcium Carbonate: 1. Spontaneous Precipitation of Calcium Carbonate in the Presence of Dissolved Silica. *Geochimica Cosmochimica Acta* **2010**, *74*, 2655-2664.
- (98) Okhrimenko, D. V.; Nissenbaum, J.; Andersson, M. P.; Olsson, M. H. M.; Stipp, S. L. S., Energies of the Adsorption of Functional Groups to Calcium Carbonate Polymorphs: The Importance of -OH and -COOH Groups. *Langmuir* **2013**, *29*, 11062-11073.
- (99) Blochl, P. E.; Jepsen, O.; Andersen, O. K., Improved Tetrahedron Method for Brillouin-Zone Integrations. *Physical Reviews B: Condensed Matter* **1994**, *49*, 16223-16233.
- (100) Henkelman, G.; Jonsson, H., Improved Tangent Estimate in the Nudged Elastic Band Method for Finding Minimum Energy Paths and Saddle Points. *Journal of Chemical Physics* **2000**, *113*, 9978-9985.
- (101) Henkelman, G.; Uberuaga, B. P.; Jonsson, H., A Climbing Image Nudged Elastic Band Method for Finding Saddle Points and Minimum Energy Paths. *Journal of Chemical Physics* **2000**, *113*, 9901-9904.
- (102) Marcus, P.; Mansfeld, F. B., *Analytical Methods in Corrosion Science and Engineering*; CRC press. USA, **2005**.
- (103) Voigts, F.; Bebensee, F.; Dahle, S.; Volgmann, K.; Maus-Friedrichs, W., The Adsorption of CO₂ and Co on Ca and CaO Films Studied with MIES, UPS and XPS. *Surface Science* **2009**, *603*, 40-49.
- (104) Funk, A.; Trettin, H. F. R., Dft Study on the Effect of Water on the Carbonation of Portlandite. *Industry and Engineering Chemical Research* **2013**, *52*, 2168-2173.
- (105) Tian, R.; Seitz, O.; Li, M.; Hu, W.; Chabal, Y. J.; Gao, J., Infrared Characterization of Interfacial Si-O Bond Formation on Silanized Flat SiO₂/Si Surfaces. *Langmuir* **2010**, *26*, 4563-4566.
- (106) Kim, Y.-Y.; Schenk, A. S.; Ihli, J.; Kulak, A. N.; Hetherington, N. B. J.; Tang, C. C.; Schmahl, W. W.; Griesshaber, E.; Hyett, G.; Meldrum, F. C., A Critical Analysis of Calcium Carbonate Mesocrystals. *Nature Communications* **2014**, *5*.
- (107) Lin-Vien, D.; Colthup, N. B.; Fatelny, W. G.; Grasselli, J. G., Chapter 9 - Compounds Containing the Carbonyl Group. In *the Handbook of Infrared and Raman Characteristic Frequencies of Organic Molecules*, Grasselli, D. L.-V. B. C. G. F. G., Ed. Academic Press: San Diego, **1991**, 117-154.
- (108) Chollet, M.; Horgnies, M., Analyses of the Surfaces of Concrete by Raman and FTIR Spectroscopies: Comparative Study of Hardened Samples after Demoulding and after Organic Post-Treatment. *Surface and Interface Analysis* **2011**, *43*, 714-725.
- (109) Genge, M. J.; Jones, A. P.; Price, G. D., An Infrared and Raman Study of Carbonate Glasses: Implications for the Structure of Carbonatite Magmas. *Geochimica Cosmochimica Acta* **1995**, *59*, 927-937.
- (110) Yu, P.; Kirkpatrick, R. J.; Poe, B.; McMillan, P. F.; Cong, X., Structure of Calcium Silicate Hydrate (C-S-H): Near-, Mid-, and Far-Infrared Spectroscopy.

Journal of the American Ceramic Society **1999**, *82*, 742-748.

(111) Oelkers, E. H.; Golubev, S. V.; Chairat, C.; Pokrovsky, O. S.; Schott, J., The Surface Chemistry of Multi-Oxide Silicates. *Geochimica et Cosmochimica Acta* **2009**, *73*, 4617-4634.

(112) Garbev, K.; Stemmermann, P.; Black, L.; Breen, C.; Yarwood, J.; Gasharova, B., Structural Features of C-S-H(I) and Its Carbonation in Air - a Raman Spectroscopic Study. Part I: Fresh Phases. *Journal of the American Ceramic Society* **2007**, *90*, 900-907.

(113) Queeney, K. T.; Weldon, M. K.; Chang, J. P.; Chabal, Y. J.; Gurevich, A. B.; Sapjeta, J.; Opila, R. L., Infrared Spectroscopic Analysis of the Si/SiO₂ Interface Structure of Thermally Oxidized Silicon. *Journal of Applied Physics* **2000**, *87*, 1322-1330.

(114) Maxisch, M.; Thissen, P.; Giza, M.; Grundmeier, G., Interface Chemistry and Molecular Interactions of Phosphonic Acid Self-Assembled Monolayers on Oxyhydroxide-Covered Aluminum in Humid Environments. *Langmuir* **2011**, *27*, 6042-6048.

(115) Liptak, M. D.; Shields, G. C., Accurate pKa Calculations for Carboxylic Acids Using Complete Basis Set and Gaussian-N Models Combined with Cpcm Continuum Solvation Methods. *Journal of the American Chemical Society* **2001**, *123*, 7314-7319.

(116) Annenkov, V. V.; Danilovtseva, E. N.; Likhoshway, Y. V.; Patwardhan, S. V.; Perry, C. C., Controlled Stabilisation of Silicic Acid Below pH 9 Using Poly(1-Vinylimidazole). *Journal of Materials Chemistry* **2008**, *18*, 553-559.

(117) Bhartia, B.; Bacher, N.; Jayaraman, S.; Khatib, S.; Song, J.; Guo, S.; Troadec, C.; Puniredd, S. R.; Srinivasan, M. P.; Haick, H., Application of Organophosphonic Acids by One-Step Supercritical CO₂ on 1d and 2d Semiconductors: Toward Enhanced Electrical and Sensing Performances. *ACS Applied Materials & Interfaces* **2015**, *7*, 14885-14895.

(118) Szillies, S.; Thissen, P.; Tabatabai, D.; Feil, F.; Fürbeth, W.; Fink, N.; Grundmeier, G., Formation and Stability of Organic Acid Monolayers on Magnesium Alloy AZ31: The Role of Alkyl Chain Length and Head Group Chemistry. *Applied Surface Science* **2013**, *283*, 339-347.

(119) Vyazovkin, S., Chemical Processes. In *Isoconversional Kinetics of Thermally Stimulated Processes*, Springer International Publishing: **2015**; 163-231.

(120) Tan, G.; Tang, D.; Mu, T.; Xu, C.; Wang, D.; Wang, Q., The Validity of Nonlinear Isoconversional Method in the Kinetic Analysis of Calcium Carbonate Decomposition under Isothermal and Non-Isothermal Conditions. *Thermochimica Acta* **2014**, *585*, 21-24.

(121) Bolton, J. R., Calculation of Ultraviolet Fluence Rate Distributions in an Annular Reactor: Significance of Refraction and Reflection. *Water Research* **2000**, *34*, 3315-3324.

(122) Ebbert, C.; Grundmeier, G.; Buitkamp, N.; Kroeger, A.; Messerschmidt, F.; Thissen, P., Toward a Microscopic Understanding of the C-S-H/Water Interface. *Applied Surface Science* **2014**, *290*, 207-214.

(123) Briñas, R. P.; Troxler, T.; Hochstrasser, R. M.; Vinogradov, S. A., Phosphorescent Oxygen Sensor with Dendritic Protection and Two-Photon Absorbing

Antenna. *Journal of the American Chemical Society* **2005**, *127*, 11851-11862.

(124) Bricks, J. L.; Kovalchuk, A.; Trieffinger, C.; Nofz, M.; Büschel, M.; Tolmachev, A. I.; Daub, J.; Rurack, K., On the Development of Sensor Molecules That Display Fe(III)-Amplified Fluorescence. *Journal of the American Chemical Society* **2005**, *127*, 13522-13529.

(125) Knözinger, H., Infrared Spectroscopy for the Characterization of Surface Acidity and Basicity. In *Handbook of Heterogeneous Catalysis*, Wiley-VCH Verlag GmbH & Co. KGaA. Germany, **2008**.

(126) Raynaud, S.; Champion, E.; Bernache-Assollant, D.; Thomas, P., Calcium Phosphate Apatites with Variable Ca/P Atomic Ratio I. Synthesis, Characterisation and Thermal Stability of Powders. *Biomaterials* **2002**, *23*, 1065-1072.

(127) Ohashi, Y.; Finger, L. W., The Role of Octahedral Cations in Pyroxenoid Crystal Chemistry; I, Bustamite, Wollastonite, and the Pectolite-Schizolite-Serandite Series. *American Mineralogist* **1978**, *63*, 274-288.

(128) Yamnova, N.; Sarp, K.; Egorov-Tismenko, Y. K.; Pushcharovski, D.; Dasgupta, G., Crystal Structure of Jaffeite. *Crystal Reports* **1993**, *38*, 464-467.

(129) Yamnova, N. A.; Zubkova, N. V.; Eremin, N. N.; Zadov, A. E.; Gazeev, V. M., Crystal Structure of Larnite Beta-Ca₂SiO₄ and Specific Features of Polymorphic Transitions in Dicalcium Orthosilicate. *Crystal Reports* **2011**, *56*, 210-220.

(130) Downs, R. T.; Hall-Wallace, M., The American Mineralogist Crystal Structure Database. *American Mineralogist* **2003**, *88*, 247-250.

(131) Hirai, T.; Hodono, M.; Komasa, I., The Preparation of Spherical Calcium Phosphate Fine Particles Using an Emulsion Liquid Membrane System. *Langmuir* **2000**, *16*, 955-960.

(132) Andrews, L. D.; Deng, H.; Herschlag, D., Isotope-Edited FTIR of Alkaline Phosphatase Resolves Paradoxical Ligand Binding Properties and Suggests a Role for Ground-State Destabilization. *Journal of the American Chemical Society* **2011**, *133*, 11621-11631.

(133) Reyes-Gasga, J.; Martínez-Piñeiro, E. L.; Rodríguez-Álvarez, G.; Tiznado-Orozco, G. E.; García-García, R.; Brès, E. F., XRD and FTIR Crystallinity Indices in Sound Human Tooth Enamel and Synthetic Hydroxyapatite. *Materials Science and Engineering C* **2013**, *33*, 4568-4574.

(134) Du, Q.; Superfine, R.; Freysz, E.; Shen, Y. R., Vibrational Spectroscopy of Water at the Vapor/Water Interface. *Physical Reviews Letters* **1993**, *70*, 2313-2316.

(135) Alarcon-Ruiz, L.; Platret, G.; Massieu, E.; Ehrlacher, A., The Use of Thermal Analysis in Assessing the Effect of Temperature on a Cement Paste. *Cement and Concrete Research* **2005**, *35*, 609-613.

(136) Gasparini, E.; Tarantino, S. C.; Ghigna, P.; Riccardi, M. P.; Cedillo-González, E. I.; Siligardi, C.; Zema, M., Thermal Dehydroxylation of Kaolinite under Isothermal Conditions. *Applied Clays Science* **2013**, *80-81*, 417-425.

(137) Elzinga, E. J.; Sparks, D. L., Phosphate Adsorption onto Hematite: An in Situ ATR-FTIR Investigation of the Effects of pH and Loading Level on the Mode of Phosphate Surface Complexation. *Journal of Colloid and Interface Science* **2007**, *308*, 53-70.

(138) Klähn, M.; Mathias, G.; Kötting, C.; Nonella, M.; Schlitter, J.; Gerwert, K.; Tavan, P., Ir Spectra of Phosphate Ions in Aqueous Solution: Predictions

of a DFT/MM Approach Compared with Observations. *The Journal of Physical Chemistry A* **2004**, *108*, 6186-6194.

(139) Okano, K.; Miyamaru, S.; Kitao, A.; Takano, H.; Aketo, T.; Toda, M.; Honda, K.; Ohtake, H., Amorphous Calcium Silicate Hydrates and Their Possible Mechanism for Recovering Phosphate from Wastewater. *Separation and Purification Technology* **2015**, *144*, 63-69.

(140) Kim, D. W.; Cho, I.-S.; Kim, J. Y.; Jang, H. L.; Han, G. S.; Ryu, H.-S.; Shin, H.; Jung, H. S.; Kim, H.; Hong, K. S., Simple Large-Scale Synthesis of Hydroxyapatite Nanoparticles: In Situ Observation of Crystallization Process. *Langmuir* **2010**, *26*, 384-388.

(141) Martin, R. I.; TenHuisen, K. S.; Leamy, P.; Brown, P. W., Enthalpies of Formation of Compounds in the P_2O_5 -CaO- H_2O System. *The Journal of Physical Chemistry B* **1997**, *101*, 9375-9379.

(142) Hurle, K.; Neubauer, J.; Bohner, M.; Doebelin, N.; Goetz-Neunhoeffler, F., Calorimetry Investigations of Milled Alpha-Tricalcium Phosphate (Alpha-TCP) Powders to Determine the Formation Enthalpies of Alpha-TCP and X-Ray Amorphous Tricalcium Phosphate. *Active Biomaterials* **2015**, *23*, 338-346.

(143) Lenza, R. F. S.; Vasconcelos, W. L., Structural Evolution of Silica Sols Modified with Formamide. *Materials Research* **2001**, *4*, 175-179.

(144) Innocenzi, P.; Brusatin, G.; Guglielmi, M.; Bertani, R., New Synthetic Route to (3-Glycidoxypropyl)Trimethoxysilane-Based Hybrid Organic-Inorganic Materials. *Chemistry of Materials* **1999**, *11*, 1672-1679.

(145) Hidalgo, A.; Petit, S.; Domingo, C.; Alonso, C.; Andrade, C., Microstructural Characterization of Leaching Effects in Cement Pastes Due to Neutralisation of Their Alkaline Nature: Part I: Portland Cement Pastes. *Cement and Concrete Research* **2007**, *37*, 63-70.